Bathymetry induced turbulence modelling the Alderney Race site : regional approach with TELEMAC-LES

Adrien Bourgoin

Normandie Université

THÈSE

Pour obtenir le diplôme de doctorat

Spécialité MECANIQUE DES FLUIDES, ENERGETIQUE, THERMIQUE, COMBUSTION, ACOUSTIQUE

Préparée au sein de l'Université de Caen Normandie

Modélisation de la turbulence engendrée par la morphologie dans le Raz Blanchard : Approche régionale avec TELEMAC-LES

Présentée et soutenue par
Adrien BOURGOIN

Thèse soutenue publiquement le 26/03/2019 devant le jury composé de		
M. PIERRE LUBIN	Professeur des universités, Institut national polytechnique Bordeaux	Rapporteur du jury
Mme CHANTAL STAQUET	Professeur des universités, Université Grenoble Alpes	Rapporteur du jury
M. RIADH ATA	Ingénieur, EDF	Membre du jury
M. JEROME THIEBOT	Maître de conférences HDR, Université Caen Normandie	Membre du jury
M. OLIVIER THUAL	Professeur des universités, INP Toulouse	Président du jury
M. SYLVAIN GUILLOU	Professeur des universités, Université Caen Normandie	Directeur de thèse

Thèse dirigée par SYLVAIN GUILLOU, Laboratoire universitaire des sciences appliquées de cherbourg (Caen)

UNIVERSITÉ CAEN NORMANDIE

591 ED PSIME

LUSAC

Morphology induced turbulence modelling in the Alderney Race site: Regional approach with TELEMAC-LES

Acknowledgments

Ce travail s'inscrit dans le cadre du projet ANR/ITE FEM THYMOTE et a été financé par une aide de l'Etat gérée par l'Agence Nationale de la Recherche au titre du programme Investissements d'avenir et par France Energies Marines portant la référence ANR-10-IEED-0006-11.

Ce travail est le fruit d'une collaboration entre le Laboratoire Universitaire des Sciences Appliquées de Cherbourg (LUSAC) et le Laboratoire d'Hydraulique Saint-Venant (LHSV) dont je remercie sa directrice Nicole Goutal pour son accueil. Il s'inscrit dans le cadre du projet ANR/ITE FEM THYMOTE et a été financé par une aide de l'Etat gérée par l'Agence Nationale de la Recherche au titre du programme Investissements d'avenir et par France Energies Marines portant la référence ANR-10-IEED-0006-11. La thèse a bénéficier des moyens de calcul de EDF R&D.

Je remercie très sincèrement M. Pierre LUBIN, Professeur à Bordeaux INP, et Mme. Chantal STAQUET, Professeur à Université Grenoble-Alpes, pour avoir accepté d'être rapporteur de ma thèse. Je remercie par ailleurs M. Olivier THUAL, Professeur à Toulouse INP pour avoir accepté de faire partie du jury.

Je tiens à remercier mon directeur de thèse, Sylvain GUILLOU et mon encadrant Riadh ATA, pour la qualité de leur encadrement. La réussite de cette thèse leur est en grande partie due. Ils ont tout les deux su m'aiguiller de la bonne façon, avec confiance et bienveillance. Un grand merci à Jérôme THIEBOT et Sofiane BEN-HAMADOUCHE pour l'intérêt qu'ils ont porté à mon travail, en acceptant d'intégrer le jury de thèse mais aussi pour leurs critiques, remarques et suggestions pertinentes souvent très enrichissantes durant ces trois années.

Merci à Steve d'avoir pris le temps de relire mon manuscrit. Je remercie aussi Kamal pour son amitié, ses conseils bienveillants tout au long de la thèse. Je remercie enfin Yoann et Laurent pour leur appui informatique.

Mes remerciements vont également aux autres membres du laboratoire. Je pense particulièrement à ceux qui ont partagé mon bureau : Jérémie (je regrette de n'avoir pas plus passé de temps avec toi), Alex (un plaisir d'enseigner la science à un sédimentologue) et Sofiane (il faudrait toujours avoir un ami matheux). Une pensée

aussi aux compagnons de galère qui ont traversé l'épreuve de la thèse à mes côtés (Florent, Florian, Roberto, Thomas, Pierrick et Marina). Merci aussi à mes collègues thésard THYMOTE Philippe et Maria, pour nos moments très agréables passés en réunion et colloque!

Pour finir, j'aimerais remercier ma famille. Merci pour votre soutien indéfectible. Merci à ma merveilleuse Pauline, de m'avoir su me soutenir et m'apaiser au quotidien, tout en restant patiente et tolérante dans les moments difficiles. J'embrasse enfin mes deux grand-mères, qui ont été de vrais modèles en termes de dévouement et de valeurs environnementales.

Contents

List of Figures

List of Tables

Nomenclature

Acronyms

ADCP Acoustic Doppler Current Profiler

ADV Acoustic Doppler Velocimeter

DES Detached Eddy Simulation

DFSEM Divergence Free Synthetic Eddy Method

DNS Direct Numerical Simulation

LES Large-Eddy-Simulation

RANS Reynolds Averaged Navier Stokes

SEM Synthetic Eddy Method

SUPG Streamwise Upwind Petrov Galerkin

TEC Tidal Energy Converter

TSR Tip Speed Ratio

URANS Unsteady Reynolds Averaged Navier Stokes

Greek Symbols

δ_{ij}	Kronecker symbol	-
η	Free surface elevation	m
κ	Von Karman constant	-
λ	Eddy length scale	m
λ_2	Lambda 2 criterion	s^{-2}
μ	Dynamic viscosity	$Pa.s^{-1}$

ν	Kinematic viscosity	$m^2.s^{-1}$
ν_T	Turbulent viscosity	
ν_t	Subgrid viscosity	
Ω_{ij}	Vorticity tensor	s^{-1}
ψ_i	Finite element basis functions	-
ρ	Density	$kg.m^{-3}$
σ_{ij}	Cauchy stress tensor	Pa
τ_p	Bottom friction stress	Pa
τ_{ij}	Subgrid tensor	$m^2.s^{-1}$
ε	Turbulent dissipation rate	$m^2.s^{-3}$
φ_i	Reference element basis functions	-

Mathematical signs

Δ	Laplace differential operator	
∇	Nabla differential operator	
∇_H	2D nabla differential operator	

Romans Symbols

$\boldsymbol{n}$	Normal vector	m
$\boldsymbol{u_c}$	Advection velocity	$m.s^{-1}$
$\boldsymbol{u_H}$	Horizontal velocity	ms^{-1}
$\boldsymbol{u} = (u, v, w)$	Velocity	$m.s^{-1}$
Com	Comatrice symbol	-
b	Bottom elevation	m

C	Chezy coefficient	$m^{1/2}s^{-1}$
C_f	Friction coefficient	-
C_P	Turbine power coefficient	-
C_T	Turbine thrust coefficient	-
Fr	Froude number	-
g	Acceleration of gravity	$m.s^{-2}$
I_∞	Turbulent intensity	-
K	Strickler coefficient	$m^{1/3}s^{-1}$
k	Turbulent kinetic energy	$m^2.s^{-2}$
k_s	Nikuradse coefficient	m
M	Manning coefficient	$m^{-1/3}s$
p	Pressure	Pa
p_d	Dynamic pressure	Pa
p_h	Hydrostatic pressure	Pa
Q	Q criterion	s^{-2}
R_{ij}	Reynolds tensor	$m^2.s^{-2}$
Re	Reynolds number	-
t	Time	s
t_a	Averaging duration	s

Chapter 1

Introduction of turbulence in a tidal environment

Water is the softest of all things, yet it is the most powerful.

W. Dyer

Dans le cadre de la recherche d'énergies renouvelables, les énergies marines sont considérées avec grand interêt. Pas encore mature, le secteur hydrolien représente un grand potentiel, via l'installation de fermes de turbines immergées. L'installation de machines nécessite la connaissance fine des courants marins, pour pouvoir anticiper à la fois leur performance, mais aussi leur fatigue. A première vue, la rugosité des fonds marins semble générer une turbulence importante, qui pourrait influencer grandement les turbines. La caractérisation de tels écoulements s'effectue principalement avec la simulation numériques, permettant d'établir des modèles régionaux. Cependant, la modélisation de la turbulence inhérente aux code environmentaux existants est bien souvent insuffisante.

In the framework of the renewable energy assessment, marine energies are viewed with great interest. Not yet mature, the tidal energy extraction sector has great potential, through the deployment of submerged turbine farms. The installation of machines requires a detailed knowledge of tidal currents, in order to be able to anticipate both their performance and their fatigue. Preliminary investigations suggest that the roughness of the seabed generates a significant turbulence, which could greatly influence the turbines. The characterisation of such flows is mainly carried out with numerical simulation, allowing regional models to be established. However, the modelling of the turbulence inherent in existing environmental softwares is often insufficient.

1.1 A promising renewable energy: the tidal current energy

1.1.1 The marine renewable energies

In the context of sustainable development and particularly in the search for new energy sources, marine energy represents a very strong potential. It includes all the technologies that produce electricity from different forces or resources in the marine environment: waves, currents, tides or temperature gradient between warm surface waters and deep cold waters.

Offshore wind turbine technology is the first mature technology in this domain. Mostly developed in Europe, there are two main types of offshore wind turbines: fixed turbines that are located on shallow waters and floating turbines that offer the advantage of being built on land and deployed in areas where the construction of foundations is not possible. These concepts are experiencing significant growth in Europe (with 15GW already installed), and have begun to develop in Asia and America in recent years.
Tidal energy is presently one of the most advanced technologies in the marine energy sector. The tidal barrage 'La Rance' (region Brittany, France) supplies energy in very large quantities (240MW installed) to the electricity grid. Other facilities exist in the world but such projects are nevertheless quite rare given the low number of sites able to host economically viable tidal power plants.

In the early 2000s, the need to develop renewable energies put a spotlight on wave energy and tidal current energy extraction. The maturity of these sectors enabled the simultaneous launch of technical and environmental studies throughout the world. Each of these sectors has different degrees of maturity and specific development prospects in the more or less long term. Most offshore renewable technologies are at the research and experimental stage. The hydroturbine then benefited from considerable technical and financial efforts, as did the development of wind power a few years earlier.

1.1.2 The tidal current energy

The tide is the periodic variation in sea or ocean level mainly due to the gravitational action of the Moon and the Sun, modulated by centrifugal force produced by the rotation of the Earth and the Moon relative to each other. The Moon, close to the

Earth, exerts on water bodies an attractive force strong enough to displace it. When the Moon is located vertically in relation to a point on the ocean surface, the water masses swell, causing a high tide. Conversely, it is the low tide for all places where the Moon can be observed on the horizon. The Sun being further from the Earth, its action is limited to strengthen or to oppose the Moon effects. When the two bodies are perpendicular to each other in relation to the Earth, their influences are thwarted, causing low tide coefficients. On the contrary, when the three celestial bodies are aligned, the Sun accentuates the effect of the Moon, causing high tidal ranges. These water masses displacements induce cyclical tidal currents, propagating periodically at several scales. Offshore, they rotate under the influence of the Coriolis force, clockwise in the Northern Hemisphere and in a trigonometric direction to the left in the Southern Hemisphere. Near the coasts, these rotating currents become alternating, i.e. they propagate in one direction during the first half of the tide and in the opposite direction during the second half.

Like all waves, tidal cycles can be decomposed into harmonic components, each of them depending on a particular physical phenomenon. These harmonics do not have the same period so their addition leads to a non-periodic signal. In terms of notation, each component's name relies on its influence body as well as its period. For example, the main constituent of tidal waves, induced by the gravitational force exercised by the Moon, is semi-diurnal so it is called M2, whereas the main wave induced by the Sun is S2.
However, a few components can be involved in flows (particularly near coasts) without being caused by astrophysical processes. Non-linear interactions of other waves can indeed induce new harmonics generation. For instance, the interaction of the M2 constituent with itself creates the M4 constituent. Moreover some refraction events can appear, for instance near the Mont Saint-Michel, where the tidal range can reach 15m.

When tidal currents flow through narrow and shallow water channels, they are constrained and become very intense. In a few small places in the world (in the order of a few square kilometers), they can reach a velocity magnitude of more than 2ms^{-1}, and can then be very promising in terms of energy extraction. Although not yet widely used, tidal energy also has a considerable potential for electricity genera-

tion. In France alone, it is estimated between 2.5 and 16.6GW, considering only the areas near the coasts, where currents are fast enough for acceptable technical and economic sizing of the machines [26].

The most interesting French tidal sites are shown in Figure 1.1, which presents both the velocity magnitude and the corresponding energy extraction potential computed in [26] using the MARS2D solver, highlighting the Alderney Race area as the highest potential site [23], capitalizing about 70% of these resources [11].

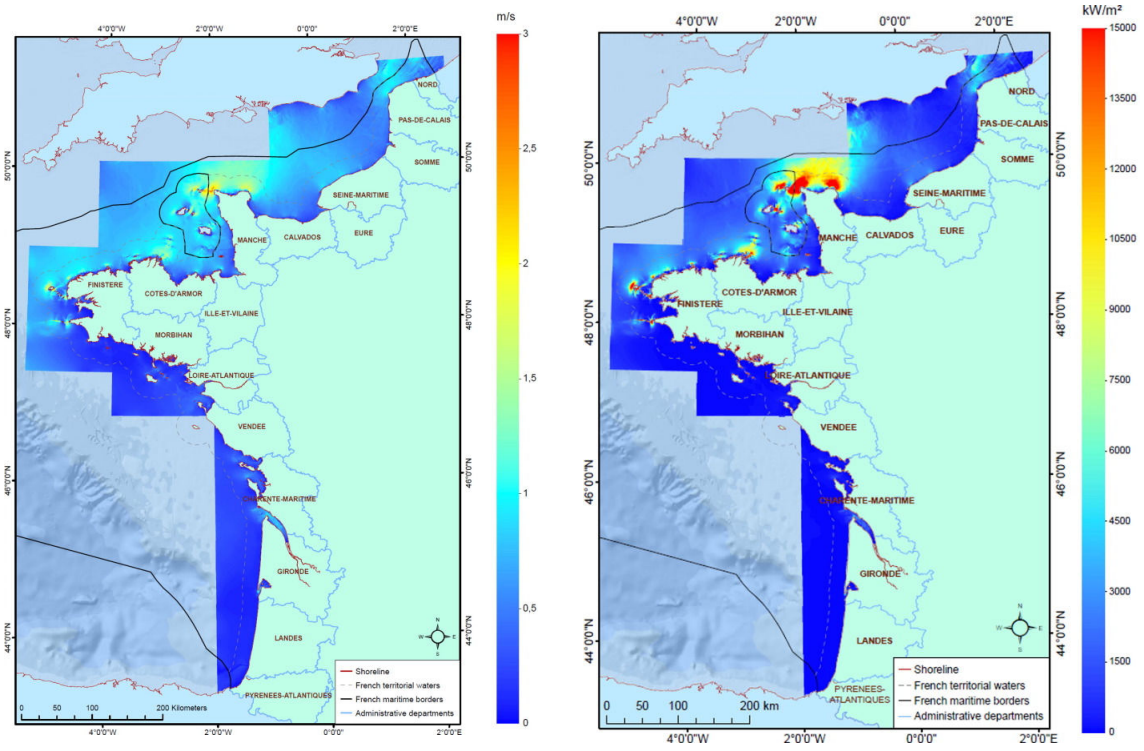

Figure 1.1: Velocity magnitude and energy potential extraction in French waters, after [26].

1.1.3 Tidal turbines: main concept and technologies

As with wind turbines, tidal energy converters have been designed as rotative machines, using lift or drag forces to set in motion a rotor that, produces electricity when connected to a generator. Despite the fact that tidal currents are generally much slower than wind, the higher density of water also enables smaller diameter rotors to extract greater levels of energy [120].

There are two main types of machines: axial flow turbines and transverse flow turbines, illustrated in Figure 1.2. There are also some more original concepts such as oscillating hydrofoils [50]. However, most of commercial devices belong to axial

Figure 1.2: From left to right, example of axial flow turbine (Atlantis AR1500) and transverse flow turbine (TidGen)

flux turbines (see the European Marine Energy Center report 2014). Despite the fact that transverse turbines have a slightly higher power density than axial turbines [120], most of industrial devices rely on the axial turbine technology, considering other practical factors such as rotor solidity.
Table 1.1 gives a few examples of the most powerful axial turbines designed for the moment.

Characteristics	Devices		
	Atlantis AR1000	MCT SeaGen S	Voith 1 MW test
Rated power (W)	1×10^6	2×10^6	1×10^6
Rated flow velocity (ms^{-1})	2.65	2.4	2.9
No. of (rotors (-))	1	2	1
Rotor diameter (m)	18	20	16
Rotor swept area (m^2)	254	314	201
Rated C_P	0.41	0.45	0.40

Table 1.1: Characteristics of a few industrial axial turbines.

1.2 Turbulence in area with strong current

1.2.1 Definition of the turbulence

In the environment, turbulence is observable in everyday life. Through natural phenomena such as a breaking wave, a cigarette smoke, a blood flow or the atmosphere on planet Jupiter, turbulent flows have a complex, disordered and largely unpredictable behaviour. This is illustrated in Figure 1.3. It includes abrupt variations of velocity and pressure as well as instabilities amplifications in a three-dimensional motion. Then, as fluid particles get a more random path, the rate of energy transferred between them is much more important than if only molecular diffusion was involved.

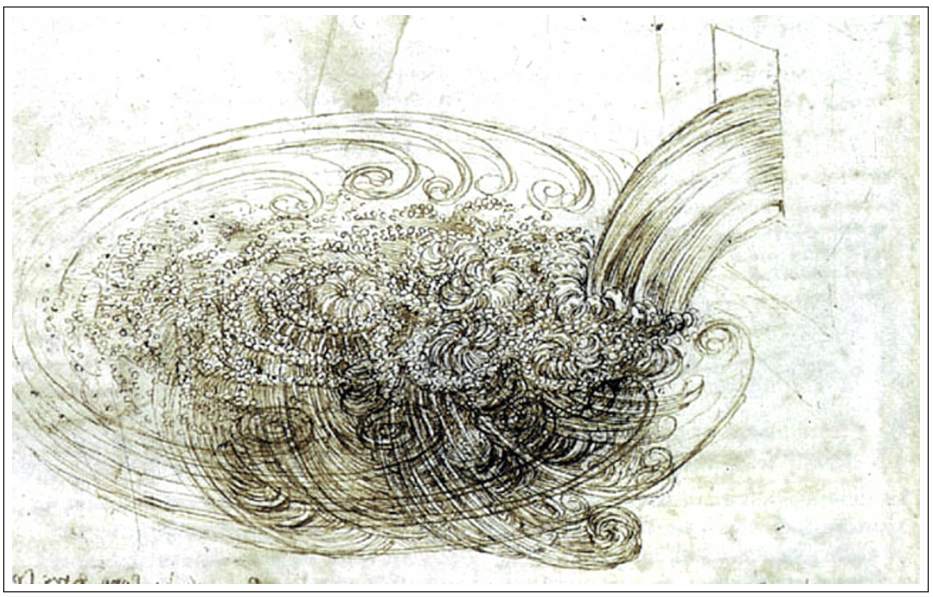

Figure 1.3: Sketch representing turbulence drawn by Leonard de Vinci.

Turbulence points out a fluid state where the momentum diffusion is small in front of the advection. This last notion becomes a source of instabilities, explaining the chaotic side of turbulent flows.

The Reynolds number is given by $Re = \frac{UD}{\nu}$ where U and D are respectively the characteristic velocity and length scales. A Reynolds number describes a laminar flow when low, and turbulent flow when high. The turbulence rate of a fluid can indeed be characterized by this dimensionless number, designating the importance of advective phenomena in the flow. The more the latter prevails in the flow, the

greater are the energy transfers, especially from the large turbulent structures to the smaller ones. The advection aspect of motion is, as such, responsible for the breakdown of rotational structures into smaller ones, where mother-eddies give a part of their energy to the daughter ones. Kolmogorov's theory [79] was born from the analysis of the interaction between a wide spectrum of turbulent structures. F. Richardson called this transfer 'energy cascade' [119]. In this concept, the vortices are differentiated according to their dimensions. We can distinguish:

- The productive scales: they represent the biggest structures, which contain most of the turbulent kinetic energy, generated by the mean flow.
- The inertial scales: they are the intermediate eddies. The energy is transfered between their different scales, regardless of the molecular viscosity and of the production mechanisms.
- The dissipating scales: theses structures do not have the sufficient energy for neglecting the molecular viscosity. Their energy is then dissipated by heat.

In Kolmogorov's study [79], each of these λ vortices' size scales is associated with a velocity noted u_λ . The largest scales are indexed here with $()_0$, and are defined by the mean flow properties. The largest dissipative scales, called Kolmogorov scales, are expressed with $()_\eta$. Then, the characteristic length and the characteristic velocity are respectively denoted with D and U, and the energy transfer rate ε_0 is assumed to be constant between the different scales. The Batchelor relation [13] is defined thanks to a dimensional analysis. It reads:

$$\varepsilon_0 = \frac{u_0^3}{\lambda_0} \approx \varepsilon_\lambda = \frac{u_\lambda^3}{\lambda} \approx \varepsilon_\eta = \frac{u_\eta^3}{\lambda_\eta} \tag{1.1}$$

Among these turbulent scales, the Kolmogorov scales (noted with $()_\eta$) are characterized by a unit Reynolds number, and so read:

$$Re_\eta = \frac{u_\eta \lambda_\eta}{\nu} = 1. \tag{1.2}$$

Their characteristic quantities can thus read:

$$\begin{cases} \lambda_\eta = \left(\frac{\nu^3}{\varepsilon_0}\right) 1/4 \\ u_\eta = (\nu\varepsilon_0)^{1/4} \end{cases} \tag{1.3}$$

The ratio between the lengths associated with the productive scales and dissipative scales can finally be expressed with:

$$\frac{\lambda_0}{\lambda_\eta} = Re_0^{3/4} \tag{1.4}$$

The energy cascade process can easily be illustrated using a spectrum of energy, indicating the turbulent kinetic energy $E(k)$ as a function of the different turbulent structures with wavelengths k, shown in the Figure 1.4.

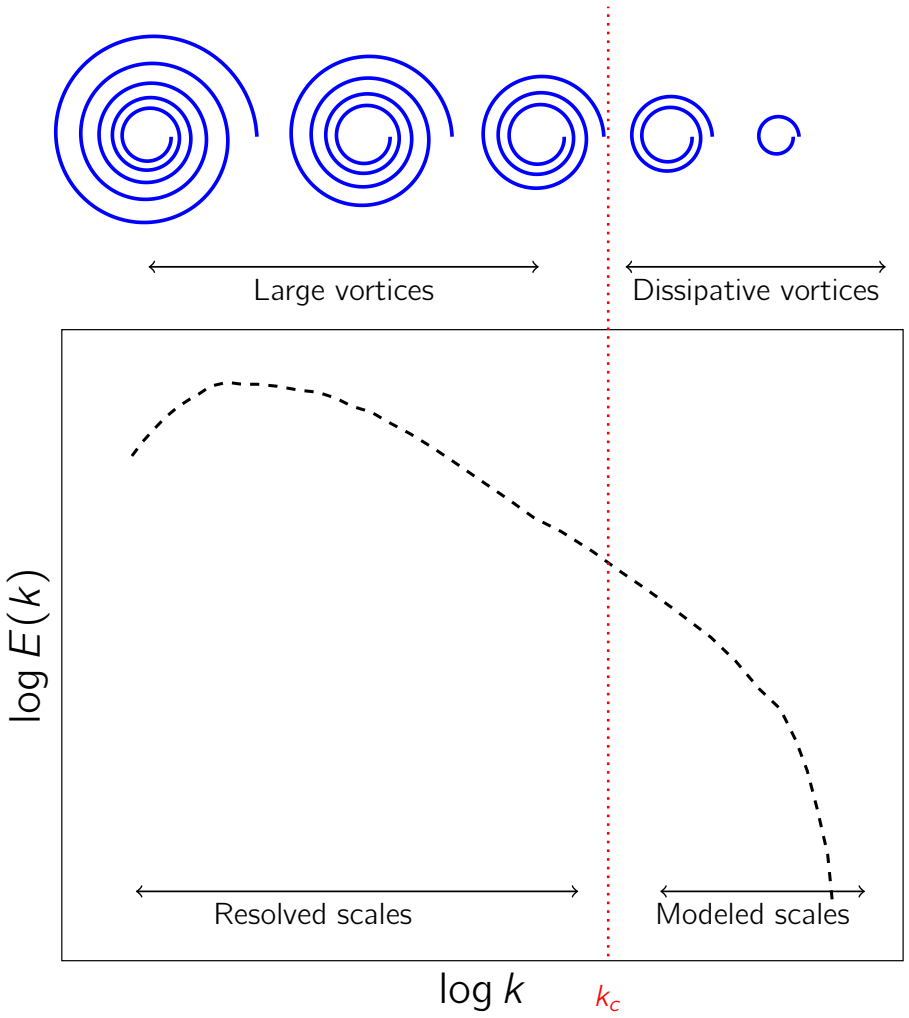

Figure 1.4: Turbulence energy spectrum.

Turbulence appears as a phenomenon mixing a broad spectrum of space-time scales, each acting differently in the flow. Since the theory of turbulence considers

Kolmogorov's work as a reference, it is important to carefully consider the assumptions made. Indeed, this dimensional analysis is based on the assumption of a local isotropic turbulence, which assumes that small scales are statistically independent of larger scales. In the case of shear flows for example, large scales can nevertheless be strongly anisotropic, making the hypothesis no longer valid.

1.2.2 The parameters of turbulence

Due to the chaotic behaviour of turbulent flows, their characterisation is based on the calculation of flow statistics, resulting from an averaging over a sufficiently long time. These statistics are mainly first and second order, which for a quantity f are respectively the averaged velocity $< f >$ and the root mean square $< f'f' >$.
By considering the velocity $\boldsymbol{u}$, these two statistic computations enable the definition of turbulence intensity I_∞ with

$$I_\infty = 100\frac{\sqrt{\frac{2}{3}k}}{<|\boldsymbol{u}|>} \tag{1.5}$$

where $<|\boldsymbol{u}|>$ is the averaged velocity magnitude and k is the turbulent kinetic energy (which corresponds actually to the half trace of Reynolds stress tensor), which read:

$$\begin{aligned} <|\boldsymbol{u}|> &= \sqrt{<u>^2 + <v>^2 + <w>^2} \\ k &= \frac{1}{2}(<u'^2> + <v'^2> + <w'^2>) \end{aligned} \tag{1.6}$$

1.2.3 The knowledge of turbulence in tidal sites

Many projects aimed at characterizing site flows that are favorable to the installation of tidal turbines have been carried out in the last few years. In addition to the characterisation of the resource that can be exploited by the different marine technologies (current intensity, wave height), these campaigns of measurement have shown that flows in the sites are highly turbulent, but also site-specific [142, 95], as summarized in Table 1.2. Ambient turbulence measurements were performed at several sites planned for the deployment of tidal turbines: Fall of Warness, UK [104], Sound of Islay, UK [95], Puget Sound, USA [141]; Strangford Narrows, UK [89], East River, USA [84], Ramsey Sound, UK [142]. Measurements made either by using ADV (Acoustic Doppler Velocimetry) or ADCP (Acoustic Doppler Current

Location	I_∞ (%)	$<\|\boldsymbol{u}\|>$ (ms^{-1})	z (m)	Device	Ref
Sound of Islay (Scotland)	$9.5-10.3$	2.0	5.0	ADV	[95]
Fall of Warness (Scotland)	$9.5-10.3$	1.5	5.0	ADCP	[104]
Puget Sound (USA)	$6.6-9.0$	1.3	4.7	ADV/ADCP	[141]
Strangford narrows (UK)	$3.2-7.1$	$1.5-3.5$	14.0	-	[89]
Grand Passage (Canada)	$10-20$	1.5	$2.1-10.1$	ADCP	[62]

Table 1.2: Flow measurements in several tidal sites.

Profiler) have shown that turbulence intensities can reach 24% and that the size of vortex structures can reach a several dozen meters width. Togneri's work [142] also indicates that the characteristics of turbulence are highly variable spatially and that they depend on the morphology of the bottom and therefore on the study site. According to Clark in [34], turbulence in these areas is influenced by several factors: ambient turbulence (which is due to upstream flow), bottom roughness (due to local bathymetry and which can lead to the formation of coherent turbulent structures), channel or coastal shape (creek, bay, cape,...) or stratification and shear due to wind and wave effects.

Depth one-day results from [104] obtained in the Fall of Warness site are illustrated in Figure 1.5, showing the current velocity $\boldsymbol{u}$, turbulent kinetic energy (TKE) intensity, Reynolds stress, τ_k, TKE production, P, and acoustic backscatter, ABS. Reproducing such flow statistics in flumes is practically impossible. However, numerical modelling can be used to simulate tidal flows and enables their easy characterisation at each point of space and at the wanted time [139, 100], but cannot yet be used to recreate a full description of the turbulence.

1.2.4 Turbulence interactions with turbines

The most promising sites for deploying turbines are high current environments located in shallow, and generally rocky areas. The current is forced and turbulent. Naturally,

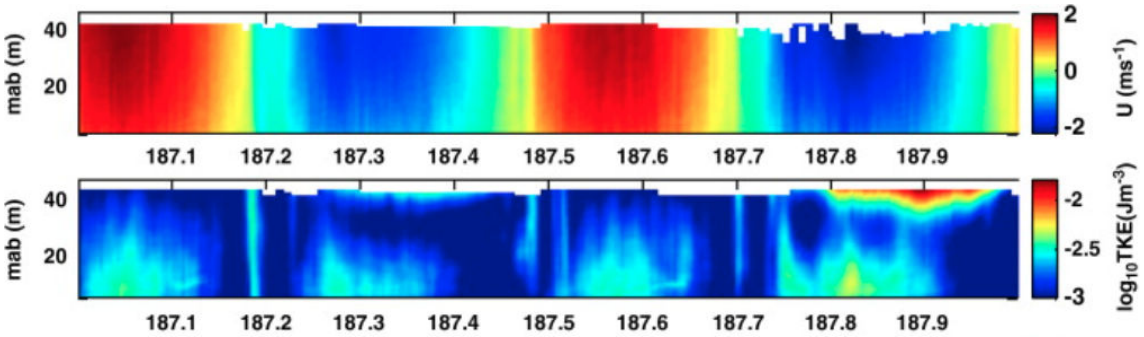

Figure 1.5: Depth–time series of flow characteristics in the Fall of Warness site . From [104]

vortex structures arise due to the high shear velocities. Once formed, structures spread with a complex dynamic which remains poorly understood. These structures, due to their size and intensity, can damage machines and disrupt their operation, that is why information about turbulence is essential for optimizing the design of wind or water turbines [141]. They produce vibrations of the turbine elements, which induces fatigue. The quantification of these strains requires a detailed knowledge of the turbulence properties of the upstream flow. In [34], Clark proposes to classify turbulent processes according to the nature of the flow and using three scales:

- Small vortices (length smaller than the blade string), inducing a local modification of the flow, and affecting the blade surface boundary layer properties (skin friction and transition location), altering mean drag and lift of a blade section.
- Medium sized vortices (smaller than the diameter of the turbine), not affecting the mean flow but causing unsteadiness of the mean flow by exerting snap loading (as blades pass through eddies, local angles of attack change) affecting blade bending modes and amplitudes.
- Finally, large size vortices (larger than the diameter of the machine), inducing a significant variability of the mean flow. The wake distortion of a turbine alters the mean mass flux through the downstream turbines, thus affecting mean loads.

It is essential to be able to have access to the different scales of turbulence that impact the functioning of the turbines in terms of structural stresses and performance.

Turbines performance are mostly investigated by evaluating their power P and thrust F_x, expressed respectively using the dimensionless coefficient C_P and C_T, which read:

$$\begin{cases} C_P = \frac{P}{\frac{1}{2}\rho\pi R^2 U_\infty^3} \\ C_T = \frac{F_x}{\frac{1}{2}\rho\pi R^2 U_\infty^2} \end{cases} \tag{1.7}$$

where ρ is the fluid density, R is the rotor radius and U_∞ is the upstream fluid velocity magnitude. These coefficients depend on the Tip-Speed-Ratio (TSR), defined as the ratio between the blade tip rotation velocity and the incident flow velocity ($TSR = \frac{\Omega R}{U_\infty}$). Several studies have been carried out to define the optimal operating point of turbines, achieved for values closed to $TSR = 4$, with nearly 40% of the energy recovered ($C_P = 0.4$) [27, 8, 91].

The influence of turbulence on the power and the thrust of TECs, as well as their wake have been examined experimentally in [98] and [18]. These measurements consist of installing a turbine model in a flume tank and a towing tank respectively, and varying the turbulent intensity in the flume. Figures 1.6 and 1.7 present respectively the power and thrust coefficients of turbines for the turbulent intensities of 3% and 15% obtained from the measurements of [98]. According to these results, increasing turbulence intensity reduces the power and the thrust by over 10% in extreme cases.

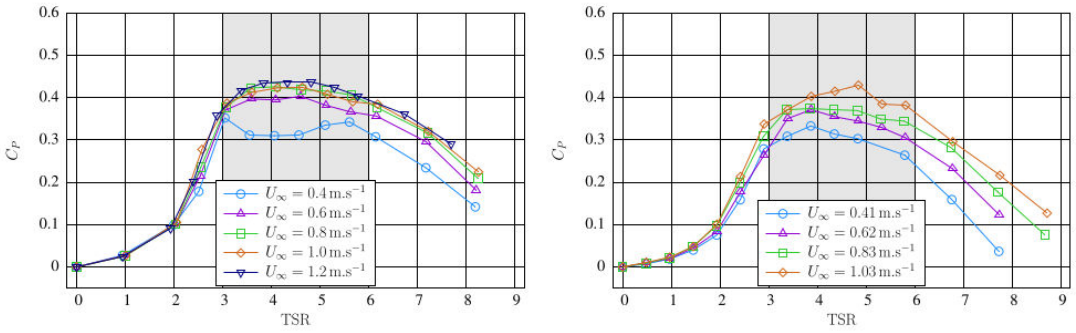

(a) $I_\infty = 3\%$ (b) $I_\infty = 15\%$

Figure 1.6: Evaluation of the power coefficient C_P function of the TSR, for $I_\infty = 3\%$ (left) and $I_\infty = 15\%$ (right). From [98]

It also causes a reduction in flapwise and edgewise blade root bending moments, but increases their fluctuations. At least, wakes dissipate much faster with high turbulent intensity.

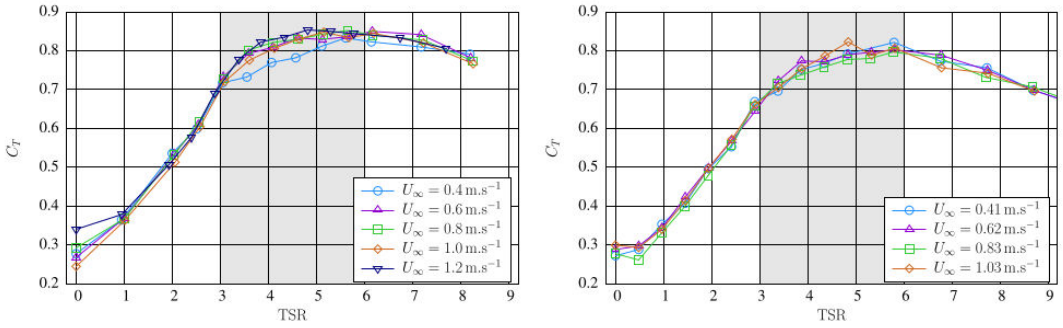

(a) $I_\infty = 3\%$ (b) $I_\infty = 15\%$

Figure 1.7: Evaluation of the thrust coefficient C_T function of the TSR, for $I_\infty = 3\%$ (left) and $I_\infty = 15\%$ (right). From [98]

This interaction has also been studied numerically in [105], where horizontal axis tidal turbine operating over an irregular bathymetry has been simulated. It confirmed that dune-induced turbulence enhances wake deficit recovery. It induces moreover sudden drops in the turbines' instantaneous performance as well as large fluctuations in the hydrodynamic loadings on the blades (up to 20% as observed in [17, 135]), the latter being a potential risk of fatigue failure of the blades.

These numerous studies provide a better understanding of the challenges faced by tidal turbines when operating in very turbulent flows and in the presence of complex bed forms, such as dunes or rocks. They also highlight the importance of considering velocity and turbulence data of future tidal turbine deployment sites in their structural design.

1.2.5 Influence of seabed morphology on vortex generation

In the vicinity of solid walls, the average velocity of a fluid is characterized by high gradients. It increases the production of turbulence due to shearing effects and make flows strongly anisotropic. This area of high gradients is called the boundary layer [31][45]. Viscous phenomena are prevalent near the walls. Characteristic velocity and length scales are defined in this area from the viscous friction on the wall τ_p, which is:

$$\tau_p = \mu \frac{\partial u}{\partial z}|_{z=0} \tag{1.8}$$

where the location $z = 0$ denoted the interface fluid-solid and μ is the dynamic viscosity. It enables the definition of a local friction velocity $u_\tau = \sqrt{\tau_p/\rho}$ with ρ being the fluid density. Moreover, a dimensionless distance to walls and a dimensionless velocity are introduced, denoted respectively by $z^+ = zu_\tau/\nu$ and $u^+ = u/u_\tau$. From these notations, it is possible to evaluate the shape of the averaged velocity profile in the different areas of the boundary layer. The near-wall region can be divided into three layers [148]:

- The viscous sublayer $(0 < z^+ < 8)$, where turbulence is negligible. In this area the velocity profile is linear, given as $u^+ = z^+$.
- The buffer layer $(10 < z^+ < 30)$ in which the velocity profile has no simple expression, characterizing the connection between the viscous sublayer and the logarithmic layer.
- The logarithmic layer $(= 30 < z^+)$, where the velocity profile get a logarithmic shape. For hydraulically smooth flow, the profile reads:

$$u^+ = \frac{1}{\kappa}\ln\left(\frac{zu_\tau}{\nu}\right) + 5.2 \tag{1.9}$$

  and for a rough flow:

$$u^+ = \frac{1}{\kappa}\ln\left(\frac{z}{k_s}\right) + 8.5 \tag{1.10}$$

  where k_s is the roughness size.

To better characterize the friction regime, it is possible to use input boundary conditions reproducing the average velocity profile of these different layers with the Reichardt's law [148], given by :

$$\frac{u}{u^*} = \frac{1}{\kappa}\ln(1+\kappa z^+) + 7.8\left(1 - e^{-\frac{z^+}{11}}\right) - \frac{z^+}{11}e^{-0.33z^+} \tag{1.11}$$

The seabed morphology and the bottom roughness of tidal flows have a great influence on the flow boundary layer, in which most coherent turbulent structures are generated [128]. The viscous boundary layer disappears in favor of a new layer: the rough sublayer [61]. Its thickness can be defined as the height at which the statistical flow quantities become uniform in the normal wall directions. Experience shows that this thickness is in the order of 2 to 5 times the roughness size. In this

layer, wakes form around the asperities, which give the statistical flow characteristics of a three-dimensional motion.

As studied in [68, 67], it has been shown that eddies of scale comparable to the roughness elements are created near the wall, and are lifted up rapidly by large-scale coherent structures to flood the flow field well above the roughness sublayer, in addition to those generated by the energy cascade. In [94], simulations of rough turbulent channel flows laden with inertial particles are performed and compared to a smooth channel flow. The roughness has a major impact since, in the flat set up, most of the particles are observed near the wall. However, the addition of roughness to the wall make the particles tend to stay away from the wall region. It exhibits higher turbulent kinetic energy, both near the wall and in the separated shear layer [152]. Most of literature findings support the Townend's wall similarity hypothesis [143], assuming that both rough wall and smooth wall statistics overlap in the outer layer [40] [149], and consequently that this layer is largely independent of wall condition.

The roughness effects induce large numbers of vortices near the bottom which propagate vertically with an upward inclination that increases with the distance to the wall. Two main types of coherent structures have been identified in [121]. Quasi-streamwise vortices are the main constituents in the buffer layer region, appearing to be shorter in rough wall flows [39]. In the upper log and wake regions, hairpin-shaped eddies are the most common [47] [132], illustrated in Figure 1.8. These coherent structures form a characteristic angle of 45° with the wall [121, 63] while propagating, and grow so long that the vortice remains in a region of shear.

Moreover, important variations of the bottom geometry can cause very energetic swirling structures in the water column. In [114], Kolk vortices are examined. They can be observed behind ribs and dunes, causing a boil phenomenon while ascending up to the free surface. The analysis of the instantaneous flow field over these obstacles reveals that the flow over large-scale roughness elements is characterized by spatial non-uniformities that are not present in flow over uniformly distributed small-scale roughness, such as sand and gravel. In these cases, the outer layer is influenced by the wall.
It displays regions of separation behind the roughness elements with fluctuating reat-

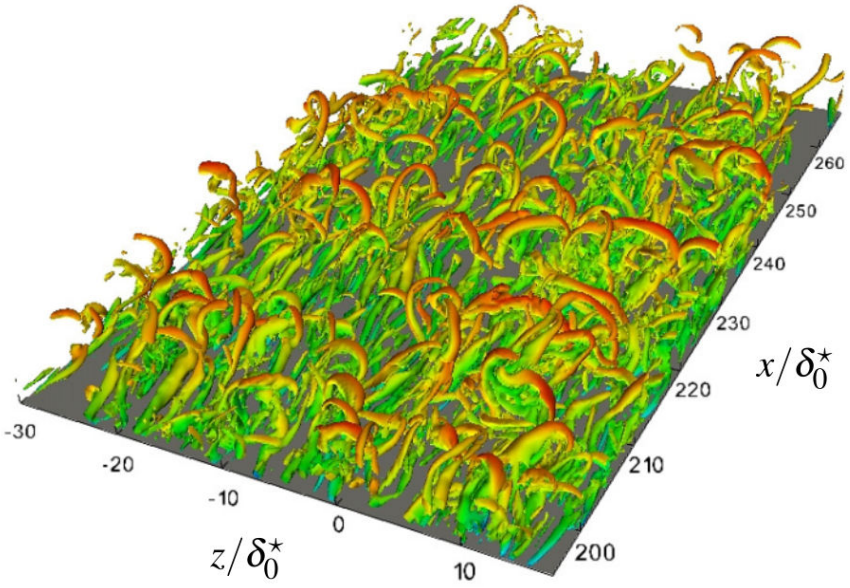

Figure 1.8: Hairpin vortices in turbulent boundary layers. From [47]

tachment points downstream of the roughness crests, and a distinct inner layer where the flow is strongly affected by the protrusion of the obstacles. In addition, a shear layer can be identified developing from the obstacle crest. Most energetic turbulent structures are generated in this area. According to the experiments of [71], the presence of an obstacle in a flow promotes the creation of this shear layer, where Kelvin-Helmotz instabilities [136] are generated from the velocity difference between the outer flow and the recirculation area. Then, these events merge, pair up or interact to form hairpin structures ejected towards the free surface to form large boils.

The floor inclination effect on turbulence wakes developed behind the obstacles is moreover investigated in [70]. The presence of an inclined floor is responsible for the appearance of a stagnation point in the shear layer, which is assumed to increase the emission of turbulent structures that reach high altitudes in the water column.

1.2.6 The Alderney Race

The Alderney Race (Raz Blanchard in French) refers to the passage where one of the most powerful tidal currents in Europe occur. It is located between the western tip of Cap de la Hague and the Channel Island of Alderney, at the northern entrance

of the Déroute Passage. This site is characterized by a mean spring tidal range of around 6m, a mean spring tidal current magnitude of about 2.5 ms^{-1} and a water depth in the range of $25-65$m [139]. These characteristics make the Alderney Race a very interesting site for installing TECs farms [100, 99, 11]. The French Environment and Energy Management Agency organized a Call for Expressions of Interests in September 2013 for the installation of a first allowed zone for turbines placement. Figure 1.9 shows the Alderney Race location as well as this tidal allowed zone (illustrated with the white polygon), coloured by the bathymetry of region.

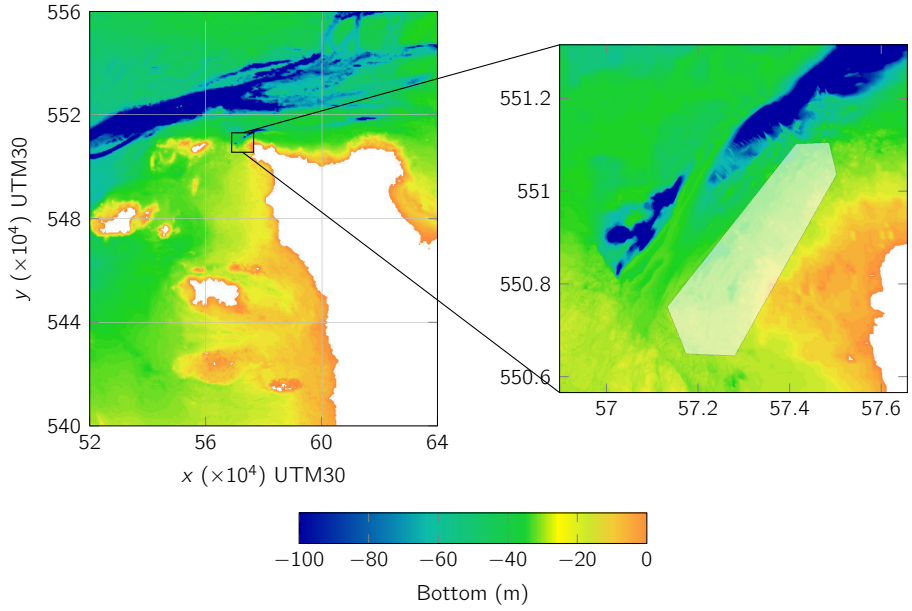

Figure 1.9: Alderney Race site and allowed zone for the installation of the pilot farms.

Tidal energy could then be extracted by installing machines in these sites. Turbines would enable the transformation of the kinetic energy of water into mechanical energy, which can then be converted into electrical energy by an alternator. The location of the turbines in these area is determined using three criteria [139], which are respectively the available tidal power resource, the water depth and the distance to the coast which should be as small as possible to permit the link between the tidal farm and the coast.

According to [35] in which the whole English Channel seabed is mapped, the seabed in the Alderney Race in mainly composed of pebbles and rocky outcrops (without sediment). An illustration of this rocky bottom is presented in Figure 1.10, showing a picture of the Alderney Race seabed taken during ADCP cells installation.

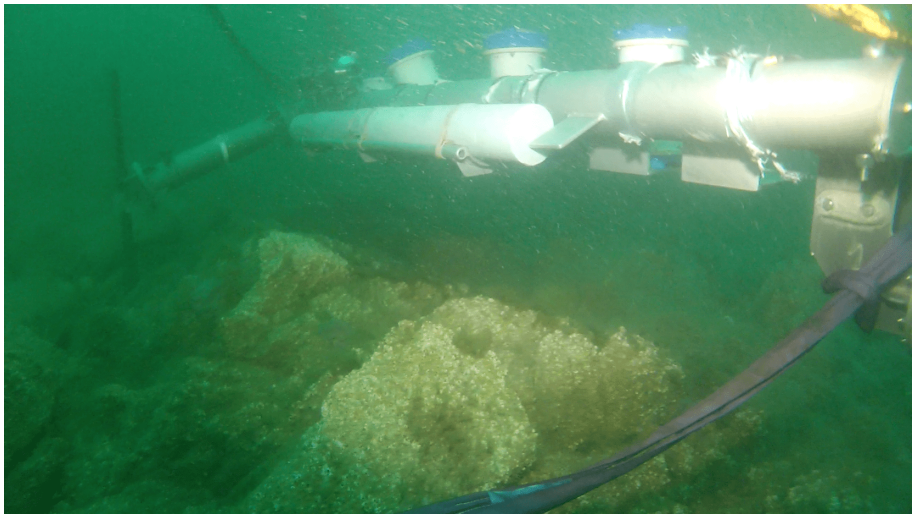

Figure 1.10: Seabed of the Alderney race, photographed during the removal of ADCP devices, THYMOTE project.

1.3 Turbulence closure for regional modelling: a prospective tool

1.3.1 Turbulence modelling approaches : DNS, LES, RANS

The most commonly used governing equations for the motion of an incompressible fluid are the Navier-Stokes equations, which link the three components of velocity u_i and the pressure p with partial differential equations. They are obtained by applying the conservation laws of mass and momentum, and read:

$$\begin{cases} \dfrac{\partial u_i}{\partial x_i} = 0 \\ \dfrac{\partial u_i}{\partial t} + u_j \dfrac{\partial u_i}{\partial x_j} = -\dfrac{1}{\rho}\dfrac{\partial p}{\partial x_i} + \dfrac{\partial}{\partial x_j}\left(\nu \dfrac{\partial u_i}{\partial x_j}\right) + f_i \end{cases} \tag{1.12}$$

Despite the fact that the study of the Navier-Stokes equations has not so far shown the existence of regular solutions in the general case, numerical methods involving a discretisation of space and time can however be used to best approach this solution. This introduces a dilemma between precision and calculation cost. The finer the discretisation is, the more precise the results are, and the more costly the calculation is in terms of execution time. Moreover, turbulence is a complex phenomenon involving a wide spectrum of space-time scales. Solving all these scales would therefore require a very fine discretisation of the computing domain and time.

The DNS (Direct Navier-Stokes) approach consists of solving all the flow scales without using any particular model. This requires an extremely fine discretisation to simulate the largest turbulent structures, but also the smallest dissipative scales. As an illustration, a flow of characteristic size $D = 1m$ and velocity average $U = 0.1ms^{-1}$ is considered. The corresponding Reynolds number is $Re = \frac{UD}{\nu} = 10^8$. The number of points per dimension to use to describe all the scales of movement can be estimated with $\frac{D}{\eta} = Re^{3/4} = 10^6$ which is extremely expensive. The DNS approach is therefore very little used in the industry, but remains widely used to generate baseline data in the research community.

In order to reduce the expensive costs of the DNS approach, several alternatives have emerged. They involve solving more or less important parts of the energy spectrum of the flow. The most widely used approach in the industry for turbulence modelling is the Reynolds Averaged Navier-Stokes (RANS) method, which consists of averaging the equations of motion. In this method, turbulent fluctuations in a flow are not resolved, but are averaged by using a time filter applied to the fluid motion. The principle of the approach is to decompose each quantity f of the flow into an average component $\bar{f}$ and a fluctuating component f_0, such as $f = \bar{f} + f'$. The values inherent to the resolution are then:

$$\bar{u_i} = \frac{1}{T}\int_0^T u_i dt, \quad \bar{p} = \frac{1}{T}\int_0^T p dt \tag{1.13}$$

Then the Navier-Stokes equations are averaged and become the Reynolds equations, which read:

$$\frac{\partial \bar{u}_i}{\partial t} + \frac{\partial \bar{u}_i}{\partial x_j}\bar{u}_j = -\frac{1}{\rho}\frac{\partial \bar{p}}{\partial x_i} + \nu\frac{\partial^2 \bar{u}_i}{\partial x_j \partial x_j} + \frac{\partial R_{ij}}{\partial x_j} \tag{1.14}$$

This operation introduces a new term, called Reynolds tensor $R_{ij} = -\overline{u_i' u_j'}$, which characterizes the interactions between velocity fluctuations. Since this tensor is unknown, it must be modeled. Several methods have been developed for this, but the most common is to assume that Reynolds tensions behave similarly to Boltzmann constraints. Using the Boussinesq approximation [22], we can directly link the Reynolds tensor components to the $\boldsymbol{S}$ deformation rate tensor with the expression:

$$R_{ij} = \frac{2}{3}k\delta_{ij} - 2\nu_T S_{ij} \tag{1.15}$$

where $k = \sum_{i=1}^{3} \bar{u}_i'^2$ is turbulent kinetic energy, $\boldsymbol{S}$ is the strain rate tensor ($S_{ij} = \frac{1}{2}\left(\frac{\partial \bar{u}_i}{\partial x_j} + \frac{\partial \bar{u}_j}{\partial x_i}\right)$) and ν_T is turbulent viscosity, which must then be estimated by a tur-

bulent model.

Several models have been designed with varying degrees of precision and complexity. The algebraic closures, otherwise called zero equations models, aim to link the eddy viscosity ν_T directly to the characteristic values of the turbulent flow. A dimensional analysis indicates ν_t can be written as a product of a velocity and a length, which turbulence models aim to evaluate.
For more complex cases, eddy viscosity can be evaluated by one or several transport equations. Depending of the transported value, it enables the knowledge of more turbulent characteristics, such as the turbulent kinetic energy. These new equations are added to the Navier-Stokes system, increasing the computation cost. The most used turbulence model is $k-\varepsilon$ [80], which involves solving two equations: one turbulent kinetic energy equation (k) and one turbulent dissipation rate ε equation. A popular model in aerodynamics is also the Spalart-Allmaras model, which solves only one equation for a viscosity-like variable. The statistical modelling of turbulence proposed by the RANS methods thus makes it possible to study the average quantities of a turbulent flow. However, some studies require knowledge of unsteady quantities, which cannot be provided by this method. In the cases of clear scale separation, the Unsteady RANS (URANS) method can be advocated [52], which involves calibrating the different settings of turbulence models to capture the desired scales. Nevertheless, in the case of fluid-structure interactions for example, more detailed data are required, such as extreme events or frequencies of turbulent structures.

A final type of approach for turbulence modelling is the Large-Eddy-Simulation (LES) method [125, 123, 116] (otherwise called subgrid modelling), which can be considered as intermediate between RANS and DNS. Indeed, whereas the RANS methodology models the whole turbulent spectrum and DNS does not involve any modelling, the LES involves dividing the spectrum into two parts. The larger turbulent structures will then be directly solved with the equations of motion, and the smaller ones will be modeled using a subgrid model. To do this, the equations of motion are filtered spatially (and not temporally as for the RANS methodology), in order to keep only the most important flow fluctuations.

1.3.2 Turbulence modelling in environmental softwares

Numerical modelling is used to evaluate the flow characteristics of tidal sites [139, 100, 113]. Turbulence in environmental flow is prominent. In geophysical flows, it is mostly modeled with Reynolds-averaged Navier-Stokes (RANS) approaches [139, 20, 10], which involves evaluating the averaged flow without describing thoroughly the turbulence statistics with a low computational cost. The RANS approach is thus the only method used in environmental softwares (Delft3D, Mike3, TELEMAC-3D, MARS-3D). Indeed, environmental applications involve most of the time considerable dimensions which is not possible to discretise finely enough to use more accurate turbulence modelling methods, such as LES or DNS. The most prevalent are thus algebraic models (constant viscosity, mixing-length model) and the $k-\varepsilon$ models.

As mentioned in the section 1.2.4, turbulence structures have a considerable influence on tidal turbines, by both affecting their lifetime and their performance. We expect that turbulence modelling would enable the identification of the main eddies involved in tidal flows. However, since the URANS modelling simulates the averaged flow over a time period, it does not permit the investigation of abrupt variation of velocity, such as the ones due to the seabed morphology.

Due to the rise of calculation resources, Large-Eddy-Simulations are now envisaged for such applications. This method enables the computation of the six components of the Reynolds stress tensor, and allows the simulation of the flow fluctuations and thus of the biggest turbulent scales. However such methods are not yet implemented in the main environmental softwares, such as TELEMAC, presented hereafter.

Research on tidal LESs has mainly focused on wakes [8, 9, 56, 105], but a recent work has been dedicated to ambient turbulence modelling characterisation. A DES (Detached Eddy Simulation) approach has been attempted in the calculation of flow in the Strait of Minas (Canada) and appear to give encouraging results [151]. This preliminary work shows that it is possible to reproduce certain flow characteristics on a morphology with a complex geometry. Many improvements are nevertheless needed to be able to use the numerical model operationally, as the numerical results

are not quantitatively compared to in situ turbulence measurements. The hard points identified concern the management of the free surface, the imposition of turbulence in the LES model, the calibration of the background roughness, the calculation times and the choice of the technique used to visualize the results.

1.4 TELEMAC-3D for regional modelling

TELEMAC-MASCARET is a suite of softwares for simulating tidal flows, and is commonly used to investigate such applications [65]. The TELEMAC-3D code solves such three-dimensional equations as the free surface flow equations (with or without the hydrostatic pressure hypothesis) and the transport-diffusion equations of intrinsic quantities (temperature, salinity, concentration). Its main results, at each point in the resolution mesh in 3D, are the velocities in all three directions and the concentrations of transported quantities. Water depth is the major result as regard the 2D surface mesh. The TELEMAC-3D's prominent applications can be found in free surface flow, in both seas and rivers. The software can take numerous natural processes into account, such as the influence of temperature and/or salinity on density, the bottom friction, the Coriolis force, or the influence of weather elements). It involves furthermore more or less complex turbulence models and diffusion of tracers.

As an illustration, the influence of waves on the tidal kinetic energy resource in the Fromveur Strait is studied in [57] using TELEMAC-3D forced with the TPXO tidal database and coupled with the spectral wave model TOMAWAC [4]. The numerical results have been compared very successfully with a series of in situ measurements of significant wave height, peak wave period, mean wave direction, as well as with data on current amplitude and direction. The need of a three dimensional model to describe tidal flows is moreover illustrated in [15] in which the water quality of the Liffey Estuary and the Dublin Bay has been estimated. The latter is modeled using the SUBIEF-3D model, based on the hydrodynamics of the TELEMAC-3D model in one case and of the TELEMAC-2D model in the other. In this study, the two-dimensional simulations were less sensitive to the effect of wind due to the depth-averaging of the hydrodynamics. In [19] the sediment transport process in the Alderney Race site is investigated using TELEMAC-2D and the module SISYPHE

[2], showing very satisfying results concerning the tidal flats evolution.
TELEMAC is a good candidate to simulate tidal flows, for the main reasons that it is open-source, is massively parallel, involves tides database (TPXO) and can be coupled with the wave module (TOMAWAC).

1.5 Objective of the work

1.5.1 THYMOTE project

The THYMOTE (Tidal Turbulence: Modeling, Observation and tank TEsts) project is a 2016-2019 French national scientific project. Its goal is to better understand the turbulent processes in tidal flows (and particularly the Alderney Race site) by providing a thorough characterisation of the turbulent statistics, to finally help the industry or technology developers to design and test their devices (see Figure 1.11). The industrial benefits of the project concern primarily the calculation of turbine fatigue and efficiency, but also the optimisation of machine placement in the farms.

Figure 1.11: Turbulent structures observed at the free surface in the Alderney Race. Source: Le tour des ports de la Manche 2013

The first technical axis concerns in situ measurements. Due to the hard environmental conditions of the Alderney Race, taking measurements in this area remains challenging and only few data have been gathered yet. Moreover, the measurement tools such as ADCP cells, used to carry on vertical profiles of velocity, are not efficient enough to capture all the turbulent scales in the water column, whereas ADV measurements are sufficiently accurate but only at one point of space. The project should thus fill this information gap with an ambitious measurement campaign.

A second dimension of the turbulence studies is realized using flume tank experiments. These test facilities would enable the accurate measurement of the turbulence induced by the rough obstacles at the bottom, and consequently the study of flows occurring over a complex bathymetry.

The third scientific approach is numerical modelling. A main advantage of numerical simulations is that they permit the characterisation of a flow at each location of a very large domain. In the THYMOTE project framework, two turbulence modelling LES approaches are applied to characterize the turbulence in Alderney Race flow at multiple scales. These methods (RANS,LES) rely on several numerical tools such as the Finite Element method (FEM) or Lattice-Boltzmann method (LBM), in order to perform simulations both at regional and local scales. The regional scales modelling of turbulence in the Alderney Race site is the objective of this PhD.

1.6 Synthesis

According to the numerous studies in the framework of the tidal energy extraction technology development, the ambient turbulence of tidal sites could strongly influence turbines performance and fatigue. Turbulence has thus to be thoroughly characterized a priori both to anticipate the energy production and to optimize the machine locations. Numerical simulations enable nowadays the characterisation of entire tidal flows using the RANS turbulence modelling. This approach aims to simulate the temporally averaged flow quantities, but is limited in describing the turbulence, which is the main advantage of using an LES method. Thanks to the rise of our calculation resources, this method is envisageable to simulate environmental

flows but has yet to be implemented. In this thesis framework, an LES approach has to be developed. This PhD work proposes in a first step to make the environmental code TELEMAC-3D evolve to integrate new features such as LES and, in a second step, to investigate turbulence in tidal flows using this methodology.

This development implies the investigation of both LES turbulence models, for which a review is described in the next chapter. This method would finally permit the accurate characterisation of the turbulent statistics of tidal flows and the identification of the most energetic turbulent structures which could strongly influence the tidal turbines functioning. The work of this PhD is within these four parts:

- Chapter 2 outlines the standard LES formulation. The method concept is briefly explained, and particular LES studies in hydraulics are taken as reference. The methodology to be implemented and applied for LES in tidal application is at last discussed.

- In Chapter 3, the TELEMAC-3D theoretical and numerical backgrounds are presented.

- Chapter 4 deals with the implementation of the LES approach in TELEMAC-3D. Several developments are described, which are mainly subgrid models, boundary conditions and numerical schemes. TELEMAC-LES is then validated using experimental results from the literature. Finally, the LES based methodology for simulating tidal flows is introduced.

- In Chapter 5, the Alderney Race model is then described, as well as data obtained using ADCP measurements used as reference. Results of averaged flow and turbulence statistics obtained with RANS, LES and ADCP are compared. A thorough analysis of numerical simulations is finally realized.

Chapter 2

Subgrid Modeling : State of the art

I am an old man now, and when I die and go to heaven there are two matters on which I hope for enlightenment. One is quantum electrodynamics, and the other is the turbulent motion of fluids. And about the former I am rather optimistic.

H. Lamb

L'idée de base de la méthode LES s'appuie sur de simples observations physiques [79] définissant la cascade d'énergie. Chaque structure tourbillonnaire semble transmettre son énergie dans des structures plus petites suivant un processus universel. En ayant supposé que les plus petits tourbillons jouent un rôle purement dissipatif, le concept de filtrage de l'écoulement a été introduit. Dans ce chapitre, la théorie globale de la LES est exposée, de part la phénoménologie de la turbulence, ainsi que les procédures numériques utilisées pour ce type de méthode. Puis la méthodologie sélectionnée pour nos applications futures est présentée.

The main concept of LES is based on simple observations [79] defining the energy cascade. Each swirling structure seems to transfer its energy into smaller ones in a universal way. Assuming that the smallest vortices have purely dissipative effects, the concept of filtering the flow has been introduced. In this chapter, the global theory of LES is explained, from the turbulence phenomenology to the numerical procedures involved in those methods. Then the most suitable models for a tidal energy application are finally discussed.

2.1 Theory of LES

2.1.1 Key concepts

The phenomenology of turbulence [79] has identified a multiscale behaviour. From a chaotic aspect, the decay of the vortex structures seems to be carried out according

to a universal model. The large turbulent scales, produced by the mean flow are very energetic and seem to depend strongly on the flow pattern such as geometry. On the other hand, small eddies seem to have a much more universal, homogeneous and isotropic behaviour. They also seem to play an essentially dissipative role. Large vortex structures transfer their energy along the energy cascade [119], and smaller ones dissipate it.

The idea of the LES is then to solve only large turbulent structures, and to model the smaller ones. It enables also the simulation of the unsteady flow behaviour while reducing the number of degrees of freedom required for direct numerical simulations. Figure 2.1 presents an illustration of a DNS velocity field compared to the corresponding LES velocity field. In a similar way to the RANS approach, the LES

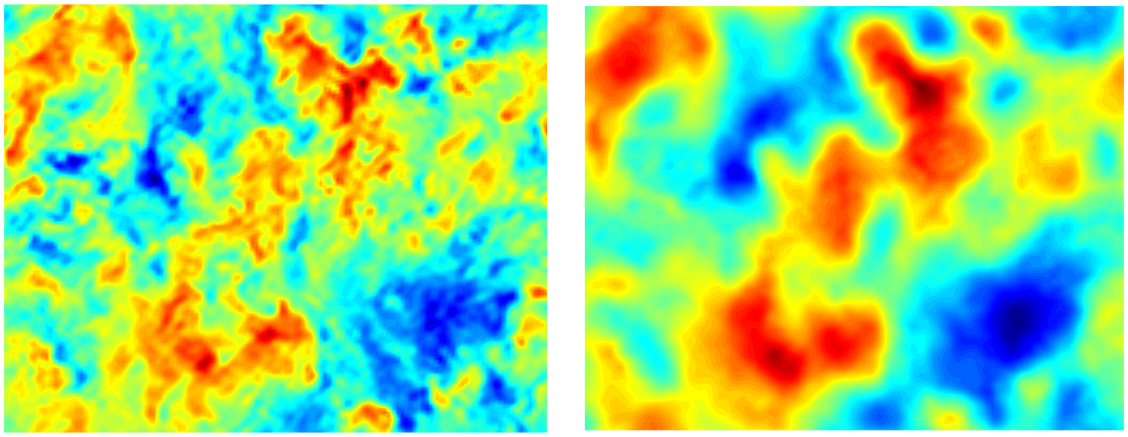

Figure 2.1: From left to right: DNS velocity field and filtered one, from [88].

method introduces an operation on the equations of motion. However, this is no longer a temporal average but a spatial filtering which will divide the turbulent scales into two categories. The larger ones are then simulated using motion equations, whereas the smaller ones are modeled using a subgrid model.

2.1.2 Governing equations filtering

To conceptualize the distinction between the resolved scales and the modeled scales [122], each f quantity is written as the sum of a filtered part marked $\tilde{f}$ and a fluctuating part f'. The filtered component can then be defined as the average of the quantity over a certain control volume V characterized by spatial discretisation. Theoretically, the filtering operator is written by using a convolution product [82],

and reads:

$$\tilde{f}(\boldsymbol{x},t) = \int_V G(\boldsymbol{x},\boldsymbol{x'},\Delta) f(\boldsymbol{x'},t) dV' \tag{2.1}$$

when applied to a variable f. In this formulation, $\boldsymbol{x}$ is the position vector where $\tilde{f}$ has to be calculated, and $\boldsymbol{x'}$ is the integrated space variable. The G function is the Δ width filter function which satisfies the property:

$$\int_V G(\boldsymbol{x},\boldsymbol{x'},\Delta) dV' = 1 \tag{2.2}$$

with a view to standardisation.
This spatial filter can be applied explicitly or can be directly induced implicitly by the discrete approximation of the governing equations. Once the filter is applied to the quantity f, the residual variable is defined by:

$$f'(\boldsymbol{x},t) = f(\boldsymbol{x},t) - \tilde{f}(\boldsymbol{x},t) \tag{2.3}$$

so that the initial quantity can be written as:

$$f(\boldsymbol{x},t) = \tilde{f}(\boldsymbol{x},t) + f'(\boldsymbol{x},t) \tag{2.4}$$

Applying the filter operation to the Equations 1.12 leads to the following filtered equations:

$$\begin{cases} \dfrac{\partial \tilde{u}_i}{\partial x_i} = 0 \\ \dfrac{\partial \tilde{u}_i}{\partial t} + \dfrac{\partial \tilde{u}_i}{\partial x_j}\tilde{u}_j = -\dfrac{1}{\rho}\dfrac{\partial \tilde{p}}{\partial x_i} + \dfrac{\partial}{\partial x_j}\left(\nu \dfrac{\partial \tilde{u}_i}{\partial x_j}\right) - \dfrac{\partial \tau_{ij}}{\partial x_j} \end{cases} \tag{2.5}$$

where τ_{ij} are the subgrid stresses, representing the effects of the unresolved fluctuations on the resolved motion. The components of this tensor read:

$$\tau_{ij} = \widetilde{u_i u_j} - \tilde{u}_i \tilde{u}_j \tag{2.6}$$

which need to be modeled by using a subgrid model.

2.1.3 Subgrid modelling

As seen in section 2.1.2, subgrid modelling relies on the filtered Navier-Stokes equations resolution (Equation 2.5). The subgrid stresses tensor $\boldsymbol{\tau}$ being an unknown, this tensor has to be evaluated using a subgrid model. However, it is important to differentiate the treatments between the decomposition introduced for the RANS

approach and the one for the LES, since statistical averaging and filtering do not follow the same mathematical properties, such as idempotence.
There are two main approaches to estimate this tensor [125]. Structural modelling, built on mathematical foundations, seeks to directly reconstruct the tensor. Functional modelling, based on more physical concepts, aims to estimate the effects of this tensor by assuming that the action of subgrid scales on resolved scales is essentially an energetic process. In hydraulics, the most widespread approach is functional modelling. The role of the subgrid models is also to bring a dissipative effect to the flow, while allowing the transfer of energy between the resolved scales [123].

Most subgrid models in use presently are eddy viscosity models [112]. As part of the RANS modelling, Boussinesq introduced the notion of turbulent viscosity [22]. Replicated and applied to subgrid modelling, the subgrid viscosity ν_t has been introduced in [131, 85] in order to link the anisotropic subgrid stress components to resolved quantities. This formulation reads:

$$\tau_{ij} - \frac{1}{3}\tau_{kk}\delta_{ij} = -2\nu_t \tilde{S}_{ij} \tag{2.7}$$

where $\tilde{S}_{ij}$ is the filtered strain rate tensor, defined by:

$$\tilde{S}_{ij} = \frac{1}{2}\left(\frac{\partial \tilde{u}_i}{\partial x_j} + \frac{\partial \tilde{u}_j}{\partial x_i}\right) \tag{2.8}$$

Concerning the isotropic part of this tensor, it is supposed to act as a pressure, so the filtered pressure $\tilde{p}$ is redefined into P for convenience writing with:

$$P = \tilde{p} + \frac{1}{3}\tau_{kk} \tag{2.9}$$

In most cases, the subgrid viscosity ν_t is obtained algebraically to avoid solving additional complex equations, that could increase the cost of calculations.
There are two other approaches to define subgrid models. For homogeneous flows, it is convenient to use spectral models, defined in Fourier space [32], [83]. An other way considering physical processes is to derive the subgrid scale energy equation. It is then solved directly or simplified by considering equilibrium assumptions [153].

2.2 Numerical framework

LES requires particular attention to the numerical methods used to implement it. Since the main concept of the method is to filter the fluid motion, spatial and

temporal discretisation have also to be sufficiently fine. Moreover, specific boundary conditions can be precribed, both to ensure the stability of the calculations and to reduce their complexity.

2.2.1 Spatial and temporal discretisation

In practice, the filtering operation proposed by LES is performed by the spatial and temporal discretisation on which the numerical method relies. The need to resolve accurately high wavenumber turbulent fluctuations implies thus both sufficiently fine meshes and higher-order schemes (at least at the second order [112]). Indeed, a certain mesh size can only solve structures with dimensions larger than its discretisation.

According to Pope in [116], the filter must retain at least 80% of the turbulent scales without which the inertial effects of intermediate structures are not reproduced. The application of the filtering operation on a $1D$ function is illustrated in the figure 2.2. A too coarse discretisation does not allow the reproduction of the abrupt variations of the filtered quantity. Moreover in [38], the minimum cells required to resolve the

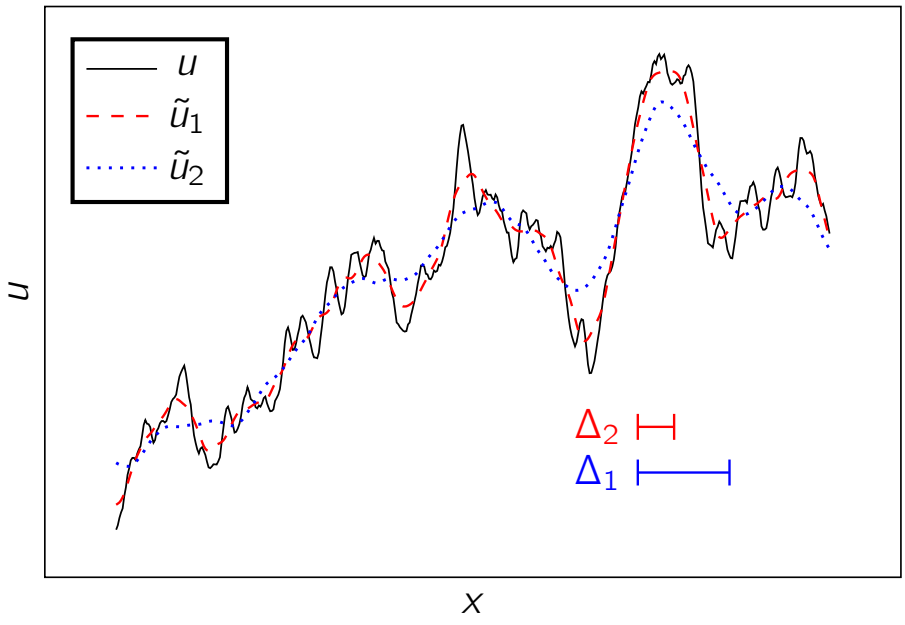

Figure 2.2: Filtering of a function.

largest scales is investigated using two-point correlations, and has been evaluated to eight cells.

Regardless of turbulence modelling, the time discretisation is usually determined by the stability requirements of numerical schemes. The (Courant-Friedrichs-Lewy) CFL condition requires that the time step be less than $\Delta t = CFL.\Delta x/|\boldsymbol{u}|$ where the maximum allowable Courant number also depends on the numerical scheme used. With LES, the physical constraint in addition to resolve turbulent fluctuations requires a time step to be less than the time scale of the smallest resolved scale of motion, and so $\Delta t \leq \Delta x/|\boldsymbol{u}|$.

2.2.2 Boundary and initial conditions for LES

In order to solve the partial differential equations in a finite domain, boundary and initial conditions have to be specified for each boundary of the domain. This section exhibits the different approaches for determining suitable conditions for Large-Eddy simulation computations. These conditions can be of various types, involving most of the time solid walls and free surface. Artificial boundaries can be introduced too in order to limit the size of the computation domain, such as inflow and outflow conditions. It can require the direct specification of the values at the boundaries, with the so-called Dirichlet conditions, or the definition of the gradients of the quantities with the Neumann conditions.

Inflow boundary conditions

The inflow has a strong influence on the quantities evolution in the calculation. Indeed, in hydraulics, flows are dominated by the convective phenomena. So the imposed values of the velocity and the pressure have to be as realistic as possible. The most popular approach is to prescribe Dirichlet boundary condition over the inlet area, but it assumes that the velocity fluctuations are known. Mostly for transitional or turbulent unsteady flows, which involve a lot of space-time modes, several techniques have been devised to furnish all the required information and minimize the error induced. Those techniques are furthermore widely used for the treatment of hybrid RANS/LES methods interfaces.

An intuitive idea for providing all the required information in the inlet area consists of introducing a little slice of flow placed at the upstream of the real computation domain, in which a precursor simulation is done. So that this simulation leads to

satisfying results, the geometry of the precursor domain, its outflow grid and the temporal resolution have to match as much as possible with the conditions at the inlet of the computation domain. In addition, the precursor calculation is realized with periodic boundary conditions in the streamwise direction, in order to get a fully developed flow. Then, the data obtained at the outflow of this section is considered as the inflow condition for the main simulation. This kind of method is quite precise, but it leads to a relatively important increase of the computation resources. Indeed, the precursor simulation can in the one hand be realized entirely before the real one, that means the data obtained is stored for each time step ; or the computation can be done in parallel with the real simulation. Whereas the first option involves some important storage resources, the second one induces a non-negligible increase of the computational time.
The alternative of computing a precursor simulation for determining the inflow conditions is to generate by introducing a synthetic turbulence at the inlet plane [81, 78, 90, 74]. These artificial fluctuations are then superimposed onto a time averaged velocity profile.

Outflow boundary conditions

The treatment of outflow boundary conditions requires less effort than the inflow ones. Particularly in hydraulics, where most flows are convection dominated, the outlet boundary has a negligible influence on the upstream flow. So, the simplest approach is to assume zero gradients along streamwise grid lines, such as :

$$\frac{\partial u_i}{\partial x_i} = 0 \tag{2.10}$$

However, if the outlet boundary is not placed far enough of the computational domain, some eddies can be convected to this region, that may induce negative velocities and negative pressure gradient. Therefore, a typically alternative used is a convective boundary conditions, which leads to solve an unsteady 1D transport equation, that is :

$$\frac{\partial u_i}{\partial t} + u_{conv}\frac{\partial u_i}{\partial x_i} = 0 \tag{2.11}$$

It requires the previously evaluated term U_{conv} thanks to the global mass conservation and then, the velocity components are calculated by using a first order backward difference scheme.

2.3 LES and environmental flows

Most environmental flows are turbulent and are bounded by at least one solid surface. In such flows, the major part of the turbulence production occurs in regions very close to the wall, named the viscous sublayer (see Section 1.2.5). Their modelling requires consequently to take into account the small turbulent structures in these areas.
A first option is to use a no-slip boundary condition at the wall. It consists of defining a fine enough spatial discretisation, both in the normal to the wall axis and the wall parallel directions to accurately resolve the boundary layer. The higher the Reynolds number of a flow is, the more the discretisation requires points, which is hardly affordable for environmental applications (often characterized by a significant Reynolds number).
The near-wall region can otherwise be modeled by specifying a correlation between the velocity in the outer flow and the stress at the wall. It involves a priori the specification of the wall roughness, but permits the use of a much coarser grid. The fluid velocity is then calculated at a point far from the wall. The distance from the wall at this point must be high enough so that the viscosity effects are negligible compared to the turbulent impacts. It must also be low enough for the logarithmic law to still be valid. Taking $\boldsymbol{P}$ to be the fluid node closest to the wall, according to [80], the law applied to the position z of this node then reads:

$$\boldsymbol{u_H}(\boldsymbol{P}) = u_\tau(\boldsymbol{P}) \left(\frac{1}{k} \ln(z(\boldsymbol{P})) + \boldsymbol{C} \right) \tag{2.12}$$

where u_τ is the friction velocity (estimated using empirical formulations) and $\boldsymbol{C}$ is a constant.
For both options, some grid resolution recommendations found in the literature are shown in the table 2.1.

	Δx^+	Δy^+	Δz_0^+
Wall resolved LES [112]	100	40	2
Wall resolved LES [30]	100	20	1
Wall modeled LES [112]	500	300	150

Table 2.1: Recommended grid resolution for LES of wall bounded flows.

2.3.1 Hybrid methods

Hybrid methods between RANS and LES approaches have been developed to reduce the subgrid modelling calculation costs. Indeed, capturing all the turbulent energy-carrying structures requires a very fine spatial discretisation, which is not always affordable for the simulation of large or high Reynolds number flows. In order to lighten the calculation, it is then possible to couple the LES methodology with less expensive approaches such as RANS modelling. These coupling concepts are mainly based on zonal decompositions of the turbulence modelling methodologies [125].

Detached Eddy Simulation

Detached-Eddy-Simulation (DES) is a method introduced in [134] for simulating flows in which turbulence outside the boundary layer is significant. Under these conditions, the solution depends only slightly on the solid walls. This method then proposes to treat near-wall areas with a RANS-type modelling and use a subgrid modelling elsewhere. Area differentiation does not involve an interface, since the type of modelling depends on a defined length scale in the flow. Regions in which this scale is smaller than the mesh size are assigned to the RANS model, whereas the LES is defined in other cases. In practice, the DES is based on a RANS turbulence model (which is mainly the Spalart-Allmaras model [133] or the $k-\omega$ model [93]). The main modification needed to produce an LES behaviour is to redefine the models' turbulent length scale using the grid resolution.

Embedded LES

The embedded LES approach involves using an LES methodology only in a defined subregion of the calculation domain and a RANS modelling outside. To reduce the complexity of the calculation, it is like using the LES only in an area of interest, or where the flow is too complex to be treated with a RANS approach. The main difficulty of the nested LES lies in the establishment of the interfaces between the subdomains, corresponding to the coupling regions between the two modelling methods. These interfaces must be specified according to their orientation with respect to the flow direction to characterize them as an inlet surface, side surface or outlet surface.

In order to get an LES solution as precise as possible, the information given by the RANS model on an interface has to be completed with an unsteady velocity field with realistic turbulent fluctuations, while remaining compatible with the RANS solution. For providing these turbulent fluctuations, the first idea (recycling method) is to use a precursor calculation which can evaluate some realistic structures that are then used by the LES model. In open channels, this calculation often characterizes a developed flow in a straight channel for which the cross section is the same than those of the LES subdomain, combined with periodic boundary conditions. However, the computational cost of this precursor calculation is not negligible, so an alternative suggests to generate as realistic as possible synthetic turbulent fluctuations according to a selected turbulent energy spectrum.
Across the RANS to LES interfaces, there is no need to provide further information, but a procedure is required to allow the LES and RANS subdomains to communicate. The LES fluctuations can indeed disturb the RANS resolution. A popular approach is also to use a convective outflow boundary condition in the LES region, and then evaluate the statistical mean-flow and the turbulence quantities from the LES solution. The averaged values are then prescribed on the interface [150].

2.3.2 LES in hydraulics

In [137], LESs of an open channel flow over two dimensional dunes have been performed. The numerical grid is sufficiently fine (about 9 million points), so the resolution is sufficiently fine to avoid near-wall treatment. The dynamic version of the Smagorinsky model [86, 54] is used for these simulations. The mean velocity field, the streamwise and wall-normal turbulent intensities as well as the Reynolds shear stress obtained by the numerical simulations agree well with experiments from [114].

A Detached Eddy Simulation (DES) study of the flow at the confluence of the Kaskaskia River and the Copper Slough stream in Illinois have been realized in [37]. The results have been compared to experimental measurements from [118]. The obtained numerical predictions are suggestive of possible real-world processes, including interactions between streamwise oriented helical cells and Kelvin-Helmholtz vortices. Flows in sharp curved open channel have also been studied using DES in [36].

DES and LES methods are compared in [127], where a flow over a periodic ar-

rangement of smoothly contoured hills is investigated. This kind of flow has been introduced in [92] and has become a standard benchmark case for testing turbulence modelling approaches. A typical reference is a high-resolved large-eddy simulation performed in [51]. The flow geometry is composed of periodic hills of height h, a streamwise extent of $L_h = 3.86h$ and separation $L_x = 9h$. The channel width and the water depth are respectively $L_y = 4.5h$ and $L_z = 3.035h$. Periodic conditions are used at both streamwise and spanwise boundaries. The Reynolds number calculated with the bulk velocity and the hill height is $Re = 60000$ in the experimental situation, but it has been reduced in order to make a feasible fine-grid LES, given $Re = 10595$.

Two turbulence models have been applied, which are the dynamic Lilly model [86] and the WALE model [102]. Moreover, several DES approaches have been used in [127]. A summary of the simulations performed for this case is given in Table 2.2 and Figure 2.3. Their main characteristics are compared, which are here t_a the averaging time, t_x the flow-through time, $()_s$ the separation point and $()_r$ denotes the reattachment one. (SJ : Saric & Jakirlic, BJ : Breuer & Jaffrezic, DC : Deng & Chikhaoui, TF : Terzi & Frôhlich, PM : Peller & Manhart).

Case	Grid	Model	$\Delta t U_b/h$	t_a/t_x	$(x/h)_s$	$(x/h)_r$
LES-ref	$281 \times 222 \times 200$	DSM	0.0018	141	0.190	4.694
DES-SJ	$160 \times 100 \times 60$	SA	0.0105	31	0.214	5.123
DES1-SJ	$160 \times 100 \times 45$	SA	0.0105	30	0.214	5.012
DES2-SJ	$160 \times 100 \times 30$	SA	0.0105	28	0.214	4.792
LES-SJ	$160 \times 100 \times 30$	SM	0.0105	28	0.182	4.902
LES1-BJ	$160 \times 100 \times 60$	SM	0.004	69	0.214	4.576
LES2-BJ	$160 \times 100 \times 30$	DSM	0.004	71	0.247	4.262
DES-BJ	$160 \times 100 \times 30$	SA	0.004	67	0.182	5.235
HYB-BJ	$160 \times 100 \times 30$	OE	0.004	65	0.279	4.792
DES-DC	$160 \times 100 \times 30$	SA	0.007	200	0.187	5.013
DES1-DC	$80 \times 100 \times 30$	SA	0.007	90	0.214	4.957
DES-TF	$160 \times 100 \times 30$	SA	0.008	93	0.182	5.123
LES-IB-PM	$221 \times 173 \times 106$	DSM	0.004	80	0.270	4.270

Table 2.2: Summary of the computations of flow over hills, after [127]

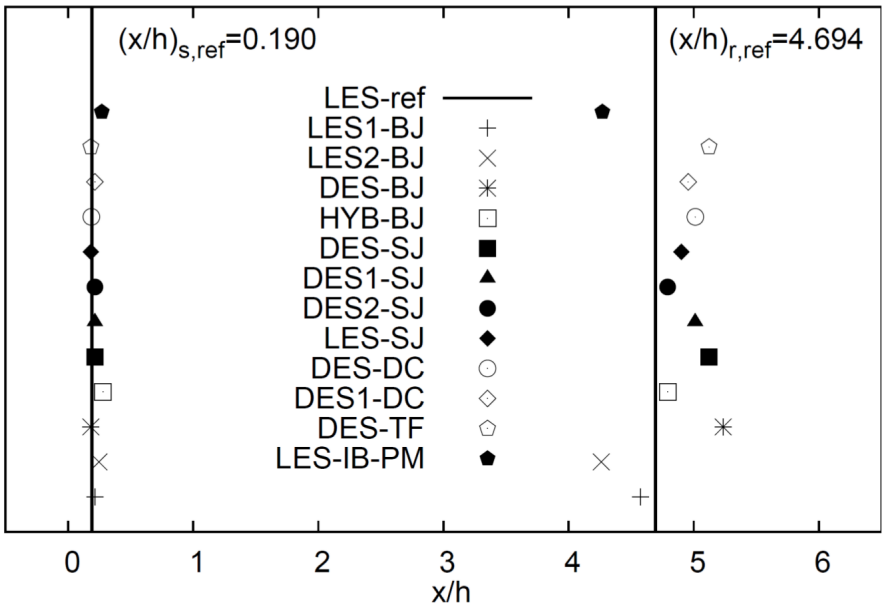

Figure 2.3: Comparison of predicted separation and reattachment locations, from [127]

Mean streamwise velocity and Reynolds shear stress profiles are also compared with the different turbulence models. The DES results exhibit a good behaviour but also a little deficiency respect to the LES2-BJ data. It predicts indeed a too short recirculation zone. By comparing the results obtained with both coarse and fine grids, LES or DES yielded results of similar quality. Saric provides evidence to suggest that DES might achieve significant advantages over LES thanks to its lower computational cost, unless the interface between the LES and RANS models moves outside the boundary layer.

The flow over periodic hills has also been studied in [52], investigating the DES method and some improvements, such as Delayed Detached Eddy Simulation (DDES). The high resolved LES from [51] used as reference, several inflow boundary conditions have been studied, which are namely a periodicity, a vortex method and a random method. The initial condition used for the DDES computation is at last defined in three different ways. The first case involves a precursor RANS simulation, which evaluates the mean flow field, the second case is an arbitrary initialisation, that is here $u = 1$ and $v = w = 0$, and the last one is based on the use of instantaneous data evaluated by a previous simulation. Differences between the variants of DES

are hardly visible near walls, but the results appear to depend strongly on the initial conditions.

2.3.3 LES of very high Reynolds number flows

The higher is the Reynolds number of a flow, the finer it has to be discretised. Without the available computer resources, simulations of very high Reynolds number flows have to be coarse [52]. By reducing the grid resolution, the impact of the model on the resolved flow field increases. If large amounts of kinetic energy are unresolved the LES results start to deteriorate. The turbulent production is not resolved anymore whereas the dissipation is overestimated. In these cases, a traditional model such as the Smagorinsky model cannot yield satisfactory results. However, simulations of atmospheric boundary layers have been successfully performed by using a new class of subgrid models [7], named minimum dissipation models [147, 124, 6], based on the invariants of the resolved strain rate tensor. The Anisotropic Minimum Dissipation (AMD) model has been used to simulate a flow driven by a velocity of 10ms^{-1} in a domain of size $5\text{km}\times5\text{km}\times2\text{km}$. Simulation results obtained with this model show a good agreement with theoretical predictions and filed observations, for both the mean flow and Reynolds stresses.

2.4 Synthesis

In the context of a thesis project, the turbulence induced by the sharp bathymetry of the Alderney Race has to be studied, with the issue of installing marine current turbines. An LES approach is envisaged, which will require to be implemented into the environmental software TELEMAC-3D. The goal is also to seek an affordable way to model this kind of free surface flow. The review of the LES methods leads to move towards DES. The latter acts indeed as a wall model, and avoids the considerable mesh refinement needed near solid walls, present in most environmental flows. This method is very common in hydraulics and has shown very good results compared to LES results, particularly in the cases involving coarse discretisations. However, TELEMAC-3D involves an efficient wall model (see section 3.1) based on physical prescriptions such as the roughness coefficient. This boundary condition enables, as DES, a relatively coarse discretisation near the walls and so a considerable reduction of the simulations' computational cost (see Table 2.1). Basic LES models are also

prioritized to be developed in TELEMAC-3D. The implementation would furthermore require the addition of specific boundary conditions, particularly to introduce velocity fluctuations at the inlet section of computational domains. At last, as explained in [96], most of numerical methods used for efficient RANS computations are not appropriate for LES. In contrast to RANS where the steady or unsteady solutions are smooth, turbulent flows have broad band spectra. Numerical procedures used for robust RANS computations are often inaccurate in the representation of the medium to small resolved eddies in LES. Consequently, at least second order and non dissipative numerical schemes are seeking to solve the filtered Navier-Stokes equations.

Chapter 3

TELEMAC-3D numerical framework

Science cannot solve the ultimate mystery of nature. And that is because, in the last analysis, we ourselves are a part of the mystery that we are trying to solve.

M. Planck

Ce chapitre présente le code TELEMAC-3D de la suite TELEMAC-MASCARET, largement utilisée pour simuler des écoulements marins [76, 97, 48, 57, 15]. Logiciel open source implémenté en Fortran, ce dernier a été priorisé pour cette étude du fait de sa flexibilité (maillages non-structurés) et donc facilitant la discrétisation de bathymetries complexes, ainsi que de bonnes performances de calcul grâce à sa parallélisation [97]. Il intègre différents modules permettant la simulation de phénomènes physiques tels que le transport sédimentaire, la propagation de vagues ou encore la qualité d'eau. Les fondements numériques de TELEMAC-3D sont décris ici.

This chapter presents the code TELEMAC-3D of the TELEMAC-MASCARET suite, widely used to simulate coastal hydraulics [76, 97, 48, 57, 15]. This open-source code written in Fortran has been selected among similar environmental software, since the usage of triangular mesh makes the code more flexible in the representation of bathymetry with complex geometry. Moreover the code has good performance on distributed memory computers [97], and has several modules which allow the simulation of physical processes such as sediment transport, wave propagation and water quality. The TELEMAC-3D numerical background is described here.

3.1 TELEMAC-3D theoretical background

TELEMAC-3D is a software initiated by EDF R&D [65, 73] developed with the computer language Fortran. It belongs to the TELEMAC-MASCARET suite which is designed for the simulation of environmental flows in the presence of a free surface

[64]. The application fields of the software focus on the maritime environment via the study of tidal currents, but also river domains. Many natural processes can be modeled, such as wave propagation or sediment transport. In addition, the CPU parallelisation of the software makes it possible to realize large models [97], by modelling for example the hydrodynamics of a whole sea. To perform this type of study, the code solves three-dimensional hydrodynamic equations.

3.1.1 Formulation

As part of the study of a free surface flow, we place ourselves in a space domain noted Ω in a reference $R = (0, x, y, z)$ (z designating the vertical axis), and whose boundary is noted Γ. In this context, the equations of motion governing turbulent flow for a Newtonian fluid are [14] :

- Mass conservation:

$$\frac{\partial \rho}{\partial t} + \nabla \cdot (\rho \boldsymbol{u}) = 0 \tag{3.1}$$

- Momentum conservation :

$$\frac{\partial \boldsymbol{u}}{\partial t} + (\boldsymbol{u} \cdot \boldsymbol{\nabla})\boldsymbol{u} = \frac{1}{\rho}\boldsymbol{\nabla} \cdot \boldsymbol{\sigma} + \boldsymbol{g} + \boldsymbol{F} \tag{3.2}$$

- Transport of tracer(s) (such as temperature) :

$$\frac{\partial T_i}{\partial t} + \boldsymbol{u} \cdot \boldsymbol{\nabla} T_i = \nabla \cdot (\nu_{T_i} \boldsymbol{\nabla} T_i) + q_{T_i} \tag{3.3}$$

- A state equation :

$$\rho = \rho(T_i, p) \tag{3.4}$$

where $\boldsymbol{F}$ designates the external forces acting on the fluid (other than weight and pressure), $\boldsymbol{\sigma}$ is the Cauchy stress tensor, $\boldsymbol{g}$ is the gravity, μ is the dynamic viscosity and T_i corresponds to the tracers.
Geophysical flows often involve the assumption of fluid incompressibility, which assumes that density is independent of pressure. In configurations involving a constant temperature and the absence of variation of an active tracer such as salinity, the conservation of the mass is therefore expressed as:

$$\nabla \cdot \boldsymbol{u} = 0 \tag{3.5}$$

This implies that the volume of fluid is conserved around time, as is the mass.
The assumption of Boussinesq [22] is introduced to estimate Cauchy's constraints tensor $\boldsymbol{\sigma}$. In this formulation, this tensor reads:

$$\boldsymbol{\sigma} = -p\boldsymbol{I} + 2\rho\boldsymbol{\nu}\boldsymbol{D} \tag{3.6}$$

where $\boldsymbol{D}$ is the Navier-Stokes tensor, which is defined by:

$$\boldsymbol{D} = \frac{1}{2}\left(\boldsymbol{\nabla u} + \boldsymbol{\nabla u}^T\right) - \frac{1}{3}(\nabla \cdot \boldsymbol{u})\boldsymbol{I} \tag{3.7}$$

In Equation 3.6, $\boldsymbol{\nu}$ is the turbulent viscosity tensor, taking into account molecular viscosity but also effects of turbulence. In practice, this tensor is supposed to be diagonal.
In the present framework, no tracer is taken into account, so the final equation set reads:

$$\begin{cases} \nabla \cdot \boldsymbol{u} = 0 \\ \dfrac{\partial \boldsymbol{u}}{\partial t} + (\boldsymbol{u} \cdot \boldsymbol{\nabla})\boldsymbol{u} = -\dfrac{1}{\rho}\boldsymbol{\nabla} p + \dfrac{1}{\rho}\boldsymbol{\nabla} \cdot \left(\mu \left[\boldsymbol{\nabla u} + \boldsymbol{\nabla u}^T\right]\right) + \boldsymbol{g} + \boldsymbol{F} \end{cases} \tag{3.8}$$

3.2 Numerical methods

3.2.1 Spatial discretisation

The mesh elements used with TELEMAC-3D are prisms (illustrated in figure 3.1), with three vertically oriented quadrilateral faces, and two triangular faces corresponding to the top and bottom of the prism (not necessarily horizontal).

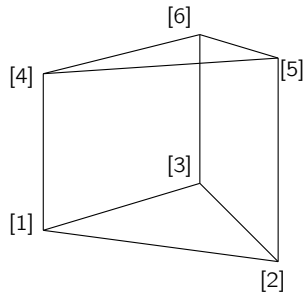

Figure 3.1: Element used for the spatial discretisation in TELEMAC-3D.

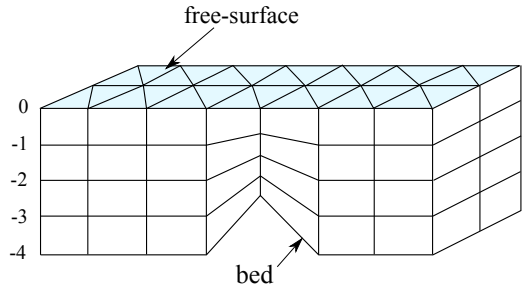

Figure 3.2: Typical grid used with TELEMAC-3D. Source : theoretical guide TELEMAC-3D [3].

The meshes result from a vertical extrusion by layers of unstructured 2D mesh. This has the advantage of having excellent practicality of use since a 3D simulation only requires the discretisation of a 2D domain, the algorithm of TELEMAC-3D being in charge of the extrusion. A typical mesh is shown in figure 3.2. However, this method does not allow the reproduction of neither submerged vertical walls, nor nonlinear waves since the extrusion is carried out from the bottom to the free surface. In other words, the functions associating both the free surface and the bottom elevation to the horizontal coordinates are injective.

The finite element method involves approximating a quantity f on such an element from the values resulting from its six vertices, via an interpolation method. The approximation of f is then noted f_h and is written :

$$f_h = \sum_i^N f_i \varphi_i \tag{3.9}$$

where f_i designates the nodal values of f on the prism and φ_i are Lagrange interpolation functions associated to the six nodes. In order to facilitate the calculation of the different matrices involved in the equations resolution, the evaluation of the quantities is based on a reference element, illustrated in the figure 3.3.

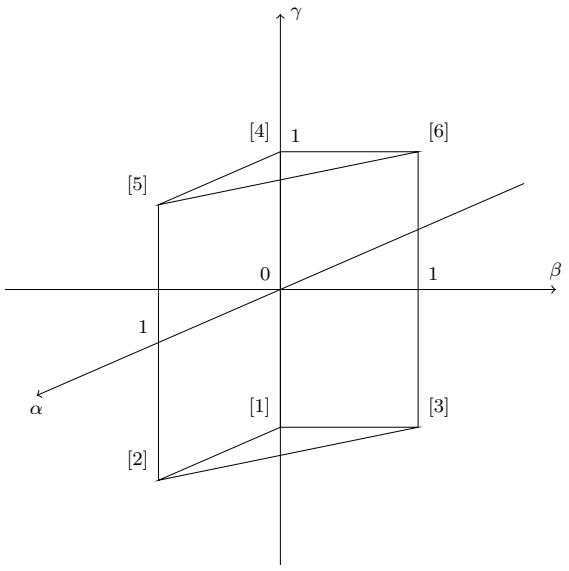

Figure 3.3: Sketch of the reference element in the coordinate system $(0, \alpha, \beta, \gamma)$.

This method involves establishing a variable change of the coordinates of the space for each prism, in order to perform the calculation from an element with simple dimensions. A reference domain Ω_{ref} is introduced, characterized by the reference $(0,\alpha,\beta,\gamma)$. In this benchmark, the basic functions associated with the respective nodes of the reference element are :

$$\begin{cases} \psi_1 = (1-\alpha-\beta)(1-\gamma)/2 \\ \psi_2 = \alpha(1-\gamma)/2 \\ \psi_3 = \beta(1-\gamma)/2 \\ \psi_4 = (1-\alpha-\beta)(1+\gamma)/2 \\ \psi_5 = \alpha(1+\gamma)/2 \\ \psi_6 = \beta(1+\gamma)/2 \end{cases} \tag{3.10}$$

Once the quantities of interest have been evaluated in this reference coordinate system, it is necessary to return to the real prism. The required variable change noted G, defining the variables of the real prism space from the reference domain Ω_{ref} is written :

$$\begin{cases} x = (1-\alpha-\beta)x_1 + \alpha x_2 + \beta x_3 \\ y = (1-\alpha-\beta)y_1 + \alpha y_2 + \beta y_3 \\ z = \frac{1-\gamma}{2}(1-\alpha-\beta)z_1 + \alpha z_2 + \beta z_3) + \frac{1+\gamma}{2}(1-\alpha-\beta)z_1 + \alpha z_2 + \beta z_3) \end{cases} \tag{3.11}$$

The determinant of the Jacobian of this transformation has to be expressed for the calculation of the different differential operators. It can be computed with:

$$\begin{aligned} |\boldsymbol{J_G}| =& \frac{1}{2}((x_2-x_1)(y_3-y_1)+(x_1-x_3)(y_2-y_1))) \\ & \times((1-\alpha-\beta)z_4+\alpha z_5+\beta z_6-(1-\alpha-\beta)z_1+\alpha z_2+\beta z_3) \end{aligned} \tag{3.12}$$

Finally, the basic functions of an Ω element read:

$$\varphi_i(x,y,z) = \psi(G^{-1}(x,y,z)) \tag{3.13}$$

3.2.2 Transformation sigma (σ)

Since the free surface evolves over time, the mesh allowing discretisation of the space domain must also be movable. To do this, TELEMAC-3D relies on a variable change for the vertical coordinate z with the sigma [110] transformation to make the spatial domain immobile. This variable change is written for the vertical coordinate z^* transformed [58]:

$$z^* = \frac{z-b}{\eta-b} \tag{3.14}$$

where b is the bottom altitude and η is the free surface elevation. The generalisation of this method among the different planes composing the mesh reads:

$$z^* = i_p - 1 + \frac{z - z_{i_p}}{z_{i_p+1} - z_{i_p}} \tag{3.15}$$

where the ip indexation designates the plan number of the considered point. The elements in the transformed mesh, noted here Ω^*, are composed as well of three vertical rectangular faces instead of trapezoidal, and the triangular faces are horizontal. A two-dimensional schematic illustration of the σ transformation is given in the figure 3.4.

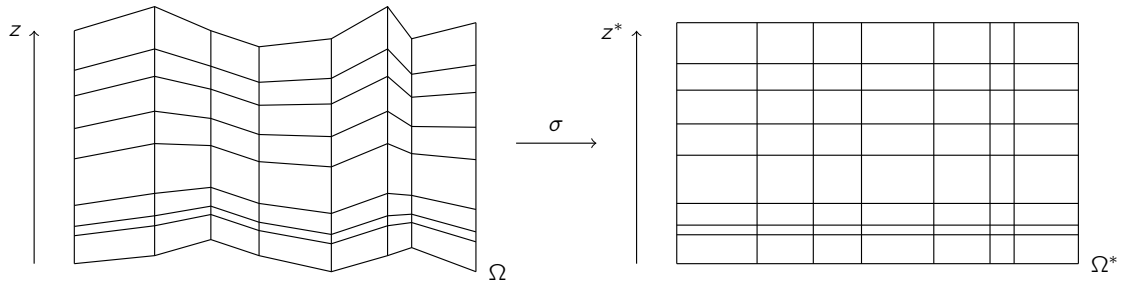

Figure 3.4: Sketch of σ transform.

A velocity noted here $\boldsymbol{c}$ is assigned to the transformed mesh, such as:

$$\boldsymbol{c} = \left.\frac{\partial z^*}{\partial t}\right|_{\Omega^*} . \boldsymbol{e_z} \tag{3.16}$$

which must be considered when solving the different equations in the transformed coordinate system. Using this variable change, the set of equations solved by TELEMAC-3D reads:

$$\begin{cases} \dfrac{\partial \boldsymbol{u}}{\partial t} + ((\boldsymbol{u} - \boldsymbol{c}) \cdot \boldsymbol{\nabla})\boldsymbol{u} = -\dfrac{1}{\rho}\boldsymbol{\nabla}(p_h + p_d) + \dfrac{1}{\rho}\boldsymbol{\nabla} \cdot \left(\mu_E \left[\boldsymbol{\nabla u} + \boldsymbol{\nabla u}^T\right]\right) + \boldsymbol{g} + \boldsymbol{F} \\ p_h = g\rho(\eta - z) + p_0 + g\rho \displaystyle\int_z^\eta \frac{\Delta\rho}{\rho} dz \\ \dfrac{\partial \eta}{\partial t} + \nabla_H \cdot \left(\displaystyle\int_b^\eta \boldsymbol{u}_H dz\right) = F_b \\ \nabla \cdot \boldsymbol{u} = 0 \end{cases} \tag{3.17}$$

where p_h and p_d are respectively the hydrostatic and the dynamic pressures, $\nabla_H \cdot$ and $\boldsymbol{u_H}$ are the horizontal gradient operator and the horizontal velocity, μ_E is the effective viscosity, F_b is the conditions prescribed on the bed boundary.

3.2.3 TELEMAC-3D algorithm

TELEMAC-3D solves the 3D Navier-Stokes equations with free surface using a finite element method on a $\boldsymbol{\sigma}$ transformation. In a domain Ω in which the boundaries correspond respectively to the bottom, to the free surface and to the side walls noted Γ_b, Γ_s and Γ_l, the algorithm is decomposed into three steps with a fractional steps method. From a velocity field u^n and an elevation of the free surface η^n, the first step is to solve the advection step of the Navier-Stokes equations.

$$\frac{\boldsymbol{u^a} - \boldsymbol{u^n}}{\Delta t} + (\boldsymbol{u_c^n}.\boldsymbol{\nabla})\,\boldsymbol{u^a} = 0 \quad \text{in} \quad \hat{\Omega} \tag{3.18}$$

where $\boldsymbol{u_c^n}$ designates the advection velocity.
TELEMAC-3D allows the use of various numerical schemes, such as the characteristics method, the SUPG formulation or the N and PSI distribution schemes. In this first step, the broadcast term is also included in the resolution for the vertical velocity case w. From the advected velocity field, TELEMAC-3D then solves the diffusion step for the horizontal velocities (noted with $\boldsymbol{u_H}$), after evaluating the new turbulence parameters and the different source terms to take into account. Also, the new free surface elevation η^{n+1} is calculated here. The algorithm then resolves:

$$\begin{cases} \frac{\boldsymbol{u_H^d} - \boldsymbol{u_H^a}}{\Delta t} - \nu \Delta \boldsymbol{u_H^d} + \dfrac{\boldsymbol{\nabla} p_h^{n+1}}{\rho} = \boldsymbol{g} \quad \text{in} \quad \hat{\Omega} \\ \dfrac{\eta^{n+1} - \eta^n}{\Delta t} + \nabla \cdot \int_{b^n}^{\eta^n} \boldsymbol{u_H^d} dz = 0 \quad \text{on} \quad \Gamma_s \end{cases} \tag{3.19}$$

with the boundary conditions:

$$\begin{cases} \rho \nu \boldsymbol{\nabla} \boldsymbol{u_H^d}.\boldsymbol{n_s} = \tau_s \boldsymbol{n_s} \quad \text{on} \quad \Gamma_s \\ \boldsymbol{u_H^d}.\boldsymbol{n}_{b,l} = 0 \quad \text{on} \quad \Gamma_{b,l} \\ (\rho \nu \boldsymbol{\nabla} \boldsymbol{u_H^d} \boldsymbol{n}_{b,l}).\boldsymbol{t}_{b,l} = -\kappa(\boldsymbol{u}).\boldsymbol{t}_{b,l} \quad \text{on} \quad \Gamma_{b,l} \end{cases} \tag{3.20}$$

where $\Gamma_{b,l}$ is here $\Gamma_b \cup \Gamma_l$.
Finally comes the continuity step, aimed at evaluating the new dynamic pressure

distribution p_d and the final velocity field, based on the Chorin-Temam algorithm [33] [138]. This methodology consists of solving the Poisson equation to evaluate pressure, then a correction is applied to velocities with the formulations :

$$\begin{cases} \Delta p_d^{n+1} = -\frac{\rho}{\Delta t} \nabla \cdot \boldsymbol{u^d} \quad \text{in} \quad \hat{\Omega} \\ \boldsymbol{u}^{n+1} = \boldsymbol{u^d} + \frac{\Delta t}{\rho} \boldsymbol{\nabla} p_d^{n+1} \quad \text{in} \quad \hat{\Omega} \end{cases} \tag{3.21}$$

with the boundary conditions for the pressure given by:

$$\begin{cases} p_d^{n+1} = 0 \quad \text{on} \quad \Gamma_s \\ \boldsymbol{\nabla} p_d^{n+1} . \boldsymbol{n}_{b,l} = 0 \quad \text{on} \quad \Gamma_{b,l} \end{cases} \tag{3.22}$$

Once this last step is completed, TELEMAC-3D starts a new iteration.

3.3 Useful physical processes modelling

3.3.1 Solid wall treatment - Law of walls

In industrial applications, the description of the fluid domain already requires a large number of points and it is often not possible to refine the mesh near solid walls (the mesh size in the viscous sublayer should be of the order of ν/u^*) [116]. TELEMAC uses the technique of the laws of walls, i.e. that the grid of the fluid domain does not exactly touch the solid wall. The first calculation point is located in the logarithmic zone of the velocity profile (at $z = 30(\nu/u^*)$ or more). In practice, this method relies on a Robin boundary condition [59], which consists of prescribing both the velocity and its derivative with respect to the normal to the solid wall. It is expressed as:

$$\tau_{xz} = \mu \frac{\partial u}{\partial n} = -\frac{1}{2} \rho C_f u^2 \tag{3.23}$$

where ρ is the density of the fluid, μ its dynamic viscosity, C_f the friction coefficient, u the flow velocity and τ_{xz} the shear stress exerted. The flow being three-dimensional, the boundary condition imposed on the bottom is exerted on the horizontal velocity field $\boldsymbol{u} = (u, v)$ according to the relation:

$$\mu \frac{\partial \boldsymbol{u}}{\partial \boldsymbol{n}} = -\frac{1}{2} \rho C_f \|\boldsymbol{u}\| \boldsymbol{u} \tag{3.24}$$

To evaluate this friction coefficient, several formulations are proposed:

- Chezy :

$$C_f = \frac{2g}{C^2} \tag{3.25}$$

- Strickler :

$$C_f = \frac{2g}{K^2 h^{1/3}} \tag{3.26}$$

- Manning :

$$C_f = \frac{2gM^2}{h^{1/3}} \tag{3.27}$$

- Nikuradse :

$$C_f = \frac{1}{\kappa} \frac{1}{(\ln(\frac{30}{e}\frac{h}{k_s}))^2} \tag{3.28}$$

where C, K, M and k_s are respectively the Chézy, Strickler, Manning, and Nikuradse coefficients, e is the mathematical constant κ is the Von Karman constant and h is the water depth.

3.3.2 Turbulence modelling

In environmental flows, the regime is always turbulent. The associated Reynolds number, evaluated with $Re = \frac{UL}{\nu}$ (where U and L are respectively the velocity and the characteristic length of the flow) is often very important, well beyond the 2000 magnitude defining the transition from a laminar to turbulent regime. To model such flows, most applications rely on Reynolds-Averaged Navier-Stokes (RANS) modelling, which consists of solving only the average flows without looking at the fluctuations. Using this RANS approach, TELEMAC-3D solves the Reynolds equations [65], characterizing the average flow. By introducing the average operation noted here $\bar{()}$ and decomposing each flow quantity into an average and fluctuating part ($f = \bar{f} + f'$), these momentum equations read:

$$\frac{\partial(\rho \bar{u_i})}{\partial t} + \frac{\partial(\rho \overline{u_i u_j})}{\partial x_j} = -\frac{\partial p}{\partial x_i} + \frac{\partial}{\partial x_j}(\tau_{ij} + R_{ij}) + \rho F_i + \rho g_i \tag{3.29}$$

where τ_{ij} is the viscous stress, such as:

$$\tau_{ij} = \mu \left(\frac{\partial u_i}{\partial x_j} + \frac{\partial u_j}{\partial x_i} \right) \tag{3.30}$$

$R_{ij} = -\rho \overline{u_i' u_j'}$ is here the Reynolds stress tensor, unknown and characterizing the correlation of velocity fluctuations. To evaluate this tensor, a closure is necessary,

which consists of estimating the second order moments from the first order moments. To do this, Boussinesq's model [22] proposes to write Reynolds' stresses in a similar way to Boltzmann's constraints, with the expression given by :

$$R_{ij} = \frac{2}{3}k\delta_{ij} - 2\nu_T \bar{S}_{ij} \tag{3.31}$$

where $\bar{\boldsymbol{S}}$ is the averaged strain rate tensor, given by:

$$\bar{S}_{ij} = \frac{1}{2}\left(\frac{\partial \bar{u}_i}{\partial x_j} + \frac{\partial \bar{u}_j}{\partial x_i}\right) \tag{3.32}$$

and k is the turbulent kinetic energy, which is worth the Reynolds tensor trace. The different turbulence models involve evaluating the turbulent viscosity rated ν_T. TELEMAC-3D offers models with zero equation models such as the mixing length model [117] as well as two equations closures, like the $k-\varepsilon$ model [80].

3.3.3 Tide modelling

To model tides, the water depth as well as the horizontal velocity at the open boundaries nodes have to be prescribed at each time step of the calculation with respect to tide data. The prescription of a quantity f (elevation or velocity) rely on a sum of harmonic constituents[129], such as:

$$f(\boldsymbol{x},t) = \sum_i f_i(\boldsymbol{x},t) \tag{3.33}$$

where the f_i are expressed as:

$$f_i(\boldsymbol{x},t) = B_{f_i}(t)A_{f_i}(\boldsymbol{x})\cos\left(2\pi\frac{t}{T_i} - \phi_{f_i}(\boldsymbol{x}) + \phi_i^0 + g_i(t)\right) \tag{3.34}$$

In this formulation, T_i is the period of the constituent, A_{f_i} is its amplitude, ϕ_{f_i} and ϕ_i^0 are respectively its phase and the initial phase and at least $B_{f_i}(t)$ and $g_i(t)$ are nodal factors. Those three last terms are corrections introduced to take into account the slow variations induced by the moon orbit tilting on the equator. The coefficients A_{fi} and ϕ_{f_i} are constant depending only on the location. Databases can be used to provide such values, with for instance the method of Janin and Blanchard [72], the LEGOS atlases [108, 107], the TPXO global tidal solution [46] and the PREVIMER atlases [111]. The water depth and velocities of each constituent are then summed

to obtain values to prescribe on liquid boundaries:

$$\begin{cases} h = \sum_i h_i - b + z_{mean} \\ u = \sum_i u_i \\ v = \sum_i v_i \end{cases} \tag{3.35}$$

where b de notes the bottom elevation and z_{mean} is the level used to calibrate the sea level.

3.4 Synthesis

The knowledge of the TELEMAC-3D theoretical and numerical backgrounds is essential to allow the integration of an LES method into the solver. The code has therefore been dissected, from the physical concept to the finite element discretisation. Since the model was designed primarily to solve the shallow water equations in three dimensions, it does not involve an accurate treatment of the vertical dimension nor a fully tridimensional resolution. The evolution of the code to integrate an LES approach will not be so trivial.

Chapter 4

Evolution of a RANS code to LES

Hofstadter's Law: It always takes longer than you expect, even when you take into account Hofstadter's Law.

D. Hofstadter

Dans ce chapitre, les différents développements nécessaires à l'implémentation de la LES sont présentés. Cela consiste principalement en l'ajout de modèles de sous-maille, mais aussi de conditions aux limites particulières et de schémas numériques non dissipatifs. Ces méthodes sont par la suite validées en comparant les résultats obtenus avec TELEMAC-3D à des données issues de mesures expérimentales réalisées en laboratoire. Les premiers résultats de suivi de détachements tourbillionnaires issus du fond et migrant vers la surface sont présentés.La simulation des écoulements marins en utilisant la LES nécessite à la fois un domaine de calcul avec une emprise suffisamment grande pour prendre en compte les échelles de marées, mais aussi une discrétisation suffisamment fine pour pouvoir capter les échelles turbulentes. Une fois la méthodologie LES implémentée, la simulation de ces écoulements demande des processus supplémentaires. La stratégie employée pour la modélisation de la turbulence marine est finalement présentée, s'appuyant sur une LES imbriquée.

In this chapter, the several developments required to implement an LES approach are presented. It relies mainly on the implementation of subgrid models, but also of specific boundary conditions and non-dissipative numerical schemes. These methods are then validated by comparing TELEMAC-3D results to experimental data from laboratory experiments. First results of vortex shedding from the bottom and migrating to the surface are presented. Performing Large-Eddy-Simulations of tidal flows would require a large enough domain to take into account the tide scales, with a very fine resolution to consider the turbulent scales. Once the LES methodology implemented, performing such simulations on tidal flow requires additional processes.

The turbulence modelling strategy based on an embedded LES method is finally presented.

4.1 Developments for LES

Solving the governing-equations requires first to discretise them in time and space. To remain consistent with the numerical basements of TELEMAC-3D, the developments described here rely on a fractional step method, which enables the separate treatment of the different transport equation terms. The time derivative of a variable named f is approximated by a centered formulation which reads:

$$\left.\frac{\partial f}{\partial t}\right|_{n+\frac{1}{2}} = \frac{f^{n+1} - f^n}{\Delta t} + o(\Delta t^2) \tag{4.1}$$

and the other terms involved in the equations are treated explicitly or implicitly.

Let Ω be a non empty bounded open space in $\mathbb{R}^n$, for which the boundary is Γ. The vectorial transport equations are multiplied by a vectorial test function $\boldsymbol{\omega}$ and integrated over each control volume.

The implementation of a Large-Eddy-Simulation approach in a solver like TELEMAC-3D requires four main developments:

- First, it is necessary to integrate the chosen subgrid models.
- Special boundary conditions may also be useful to stabilize the calculation or to reduce its numerical costs.
- LES also requires the use of a non-dissipative and at least order 2 numerical scheme in time and space, in order to efficiently transport flow fluctuations.
- Finally, post-processing requires the addition of tools for calculating flow statistics, as well as the identification of turbulent structures.

This part of the thesis presents a non-exhaustive list of the developments made in TELEMAC-3D to implement the LES methodology, working in parallel. In addition to these techniques for introducing the LES methods, the Spalart-Allmaras RANS turbulence model has been added in the Navier-Stokes solver.

4.1.1 Subgrid models

The subgrid methods developed in TELEMAC-3D are presented here. The selected subgrid models are respectively the Smagorinsky model [131], the WALE model [102] and the Anisotropic Minimum Dissipation model [124]. More details about these models are available in chapter 2.

Smagorinsky model

The most popular model in the literature (and also the first model developed) is the Smagorinsky model [131]. The anisotropic part of the subgrid tensor is directly evaluated with the deformation rate tensor from the resolved scales $\tilde{S_{ij}}$ and a subgrid viscosity ν_t with Equation 2.7. Then the subgrid viscosity remains to be constructed. By dimensional analysis, the latter can be written as a product of a l length scale and a v speed scale, resulting from subgrid motion. On physical grounds, the largest unresolved scales are the size of the numerical filter (noted $\tilde{\Delta}$). Therefore, the l scale is directly related to $\tilde{\Delta}$ via a constant C_s called the Smagorinsky constant, and reads:

$$l = C_s\tilde{\Delta} \tag{4.2}$$

The estimation of the characteristic velocity v is based on the mixing length theory [117], written as the product of a characteristic length (which is now known) and the filtered strain rate tensor standard.

$$v = l.|\tilde{S}| = C_s\tilde{\Delta}|\tilde{S}| \quad \text{where} \quad |\tilde{S}| = \sqrt{2\tilde{S}_{ij}\tilde{S}_{ij}} \tag{4.3}$$

The Smagorinsky's subgrid viscosity finally reads:

$$\nu_t = l^2|\tilde{S}| = (C_s\tilde{\Delta})^2|\tilde{S}| \tag{4.4}$$

The Smagorinsky constant C_s has no unique value in the literature [116, 123]. In general, its value varies between $C_s = 0.065$ and $C_s = 0.2$ depending on the nature of the flow modeled and numerical schemes.

WALE model

The WALE (Wall-Adapting Local Eddy-viscosity) model [102] is an extension of Smagorinsky's model. This has been designed to perform well for near-wall subgrid

viscosity without the need for a damping function. The subgrid viscosity reads:

$$\nu_t = (C_W \Delta) \frac{(S^d_{ij} S^d_{ij})^{3/2}}{(\tilde{S}_{ij} \tilde{S}^{5/2}_{ij}) + (S^d_{ij} S^d_{ij})^{5/4}} \tag{4.5}$$

with

$$S^d_{ij} = \frac{1}{2}(g^2_{ij} + g^2_{ji}) - \frac{1}{3}\delta_{ij} g^2_{kk}, \quad g_{ij} = \frac{\partial \tilde{u}_i}{\partial x_j} \quad \text{and} \quad C_W = 0.325 \tag{4.6}$$

The main advantage of the model is that it correctly predicts the behaviour of the eddy viscosity near solid surfaces i.e. verifying $\nu_t = O(z^3)$. Moreover, despite using a constant coefficient, the model predicts a zero value for the subgrid viscosity in laminar shear flow and can be used to correctly simulate flows with regions in which relaminarisation or transition to turbulence occur.

Minimum dissipation model

A recent approach in subgrid modelling uses minimum dissipation models [147] [6], which aim to provide the minimum eddy dissipation required to dissipate the energy of the subgrid scales. It was first introduced for isotropic grids in [147] by using the invariantes of the strain rate tensor, and extended into an Anisotropic Minimum Dissipation model (AMD) in [124]. These models rely on the assumption that the subgrid scales' energy of the LES solution do not increase. The AMD subgrid viscosity reads:

$$\nu_t = C \frac{\max[-(\delta x_k \partial_k u_i)(\delta x_k \partial_k u_j) S_{ij}, 0]}{(\partial_l u_m)(\partial_l u_m)} \tag{4.7}$$

where C is a constant for which the value depends on the order of the numerical schemes. According to [124], it is set to $C = 0.3$ with a central second order accurate method.

4.1.2 Inlet turbulent boundary condition

Due to the importance of the Reynolds number in turbulent flows, convection has a very strong influence on the evolution of the various quantities in the calculation. Thus, the values imposed within the border of entry must be as realistic as possible. The aim here is therefore to impose an average flow, but also to add consistent fluctuations. For this, the most intuitive idea is to use a preliminary simulation. However, this technique is very expensive. An alternative based on the same idea is periodicity, which involves introducing upstream the quantities obtained downstream

of the calculation domain. However, for flows with complex geometry, this is not always valid. In such configurations, artificial turbulence injection may be considered.

Synthetic Eddy Method (SEM)

The Synthetic Eddy Method (SEM) is a method introduced in [74] to generate artificial turbulence upstream of the computational domain. It involves generating fluctuations on the input velocity field, from a prescribed Reynolds tensor. For this, N virtual eddies are created within a three-dimensional area built around the inflow surface. The dimensions of this volume are defined by:

$$\begin{cases} x_{j,min} &= \min\limits_{x\in S, i\in 1,2,3}(x_j - \sigma(x)) \\ x_{j,max} &= \max\limits_{x\in S, i\in 1,2,3}(x_j + \sigma(x)) \\ \Delta x_j &= x_{j,max} - x_{j,min} \end{cases} \tag{4.8}$$

where σ is a length scale for the vortices, evaluated with:

$$\sigma = \max(\min(\frac{k^{3/2}}{\varepsilon}, \kappa\delta), \bar{\Delta}) \tag{4.9}$$

where k is the turbulent kinetic energy, ε denotes the turbulent dissipation rate, κ is the Von Karman constant, δ is defined as the half water depth and $\bar{\Delta}$ is the width of the numerical filter involved in the LES method. Each of the vortices is given a random position in this domain, as well as a direction of rotation for the three dimensions. Figure 4.1 illustrates the virtual box defined around the inlet section. Then the velocity fluctuations are defined from these vortex structures, with the expression:

$$u_i' = \frac{1}{\sqrt{N}} \sum_{k=1}^{N} c_i^k f_\sigma(\boldsymbol{x} - \boldsymbol{x}^k) \tag{4.10}$$

where the function f is:

$$f_\sigma(\boldsymbol{x} - \boldsymbol{x}^k) = \prod_{j=1}^{3} \sqrt{\Delta x_j} \sqrt{\frac{3}{2\sigma}} \left(1 - \frac{|x_j - x_j^k|}{\sigma}\right) \tag{4.11}$$

and c_i^k designates the intensity of the k^{th} vortice in the i^{th} direction, such as:

$$c_i^k = a_{ij}\varepsilon_j^k \tag{4.12}$$

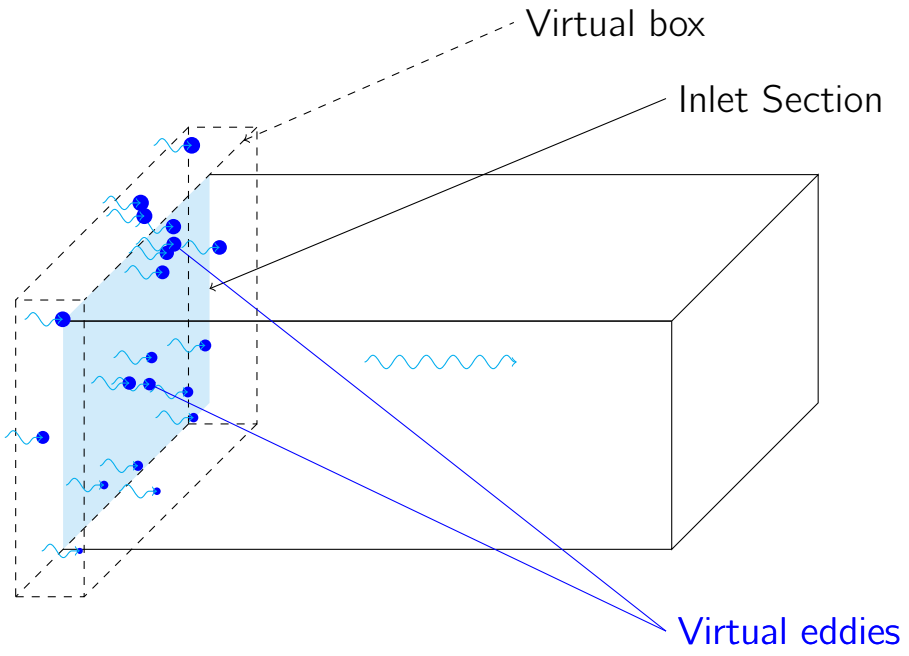

Figure 4.1: Sketch of the Synthetic Eddy Method concept.

Here $\varepsilon_j^k \in \{-1,1\}$ is the orientation of the k^{th} eddy in the j^{th} dimension and a_{ij} is the Cholesky decomposition of the Reynolds stress tensor, given by:

$$\begin{pmatrix} \sqrt{R_{11}} & 0 & 0 \\ R_{21}/a_{11} & \sqrt{R_{22}-a_{21}^2} & 0 \\ R_{31}/a_{11} & (R_{32}-a_{21}a_{31})/a_{22} & \sqrt{R_{33}-a_{31}^2-a_{32}^2} \end{pmatrix} \tag{4.13}$$

The R_{ij} are the Reynolds stresses, which are the input parameters of this method. Indeed, the SEM has the advantage of introducing a fluctuation field based on a user-defined Reynolds tensor, that can be adapted to each flow configuration. Finally, at each time step, each vortex is transported in its generation zone with the average flow. After some time, these turbulent structures leave their domain. In this case, they are reintroduced upstream, with new spanwise and vertical coordinates, as well as new random orientations. This method gives very good results provided that a Reynolds tensor is prescribed in accordance with the desired flow. To estimate the inflow turbulent kinetic energy, a RANS turbulence modelling can be performed beforehand.

Divergence Free Synthetic Eddy Method (DFSEMiso)

The DFSEMiso is a method introduced in [115] based on the SEM [74], seeking to construct zero divergence artificial turbulence. For this, the method is based on the same principle as the SEM presented in the previous subsection, namely the definition of vortices transported in a 3D domain, and inducing velocity fluctuations on a specified section. Unlike the SEM of [74], flow fluctuations are not defined in the velocity field, but in the vorticity field. The vorticity fluctuations $\boldsymbol{\omega}$ are then written:

$$\boldsymbol{\omega}'(\boldsymbol{x},t) = \sqrt{\frac{1}{N}} \sum_{k=1}^{N} \boldsymbol{\alpha}^k(t) g_\sigma \left(\frac{\boldsymbol{x} - \boldsymbol{x}^k}{\sigma} \right) \tag{4.14}$$

where $\boldsymbol{\alpha}^k$ is the intensity of the k^{th} vortex, σ is a vortex length scale and g_σ is a shape function which depends on the vortex position. By prescribing the velocity field at zero divergence, it is directly related to vorticity using the expression :

$$\nabla^2 \boldsymbol{u} = -\nabla \times \boldsymbol{\omega} \tag{4.15}$$

The components of the velocity fluctuations can then be written:

$$\boldsymbol{u}'_i = \sqrt{\frac{1}{N}} \frac{q_\sigma(d^k)}{(d^k)^3} \varepsilon_{ijl} r^l_j \alpha^k_l \tag{4.16}$$

where $r^k_i = \frac{x_i - x^k_i}{\sigma}$, $d^k = \sqrt{(x_i - x^k_i)^2}/\sigma$ and ε is the Levi-Civita tensor [101]. The shape function q_σ is given by :

$$q_\sigma(d^k) = \sqrt{\frac{16 V_B}{15\pi\sigma^3}} (\sin(\pi d^k))^2 (d^k) \tag{4.17}$$

where V_B is the volume of the generation box in which vortices are defined. The intensities α^k_n are evaluated by using the eigenvalues of the Reynolds stress tensor, denoted λ_i. They read:

$$(\alpha^k_i)^2 = \sum_{k=1}^{3} \lambda_k - 2\lambda_i \tag{4.18}$$

Conversely to SEM, the DFSEMiso method does not enable the prescription of the non-diagonal components of the Reynolds tensor, but it can be possible by extending the method into the main DFSEM method, although it requires more calculation.

To validate the two methods presented in the previous sections (SEM and DFSEMiso), these latter are tested on a flat channel flow with a constant averaged

velocity at the inflow. The size of vortices σ_k and the prescribed Reynolds stress components at the inlet are respectively:

$$\sigma_k = \min(\max(\min(\frac{\nu(k^+)^{3/2}}{\varepsilon^+ u_\tau}, \frac{1}{2}\kappa h_r), \Delta), d_w) \tag{4.19}$$

and

$$R_{ij} = \begin{cases} \frac{2}{3}k^+ u_\tau^2 & \text{if} \quad i = j \\ 0 & \text{else} \end{cases} \tag{4.20}$$

where ν is the kinematic viscosity, h_r is the reference water depth, Δ is the grid spacing, d_w is the distance to solid walls, u_τ is the friction velocity and k^+ and ε^+ are respectively the dimensionless turbulent kinetic energy and turbulence dissipation rate, defined with analytical law from [148]:

$$\begin{cases} k^+ = 0.07(z^+)^2 \exp(-\frac{z^+}{8}) + 4.5\frac{(1-\exp(-\frac{z^+}{20}))}{(1+4z^+/Re_\tau)} \\ \varepsilon^+ = \frac{1}{\kappa}\frac{1}{(z^{+4}+15^4)^{1/4}} \end{cases} \tag{4.21}$$

where z^+ is the dimensionless distance to solid wall and Re_τ is the Reynolds number based on the friction velocity. Figure 4.2 presents the vertical profiles of the three diagonal Reynolds tensor components obtained with both methods SEM and DF-SEMiso, compared to the analytical data from Equation 4.19.
These results are very satisfying since both methods give Reynolds stresses very close to the desired values. A single slight discrepancy is observed near the free surface, where the turbulent variables are underestimated.

4.1.3 Outflow boundary condition

The outflow boundary condition is more difficult to impose since the flow cannot be predicted [126]. Theoretically, this involves prescribing the dynamic limit condition defined by:

$$\begin{cases} -p_{in} + \mu\frac{\partial u_n}{\partial n} = -p_{out} + \tau_n^{out} \\ \mu\frac{\partial u_t}{\partial n} = \tau_t^{out} \end{cases} \tag{4.22}$$

In TELEMAC-3D, two types of outflow boundary conditions are available. The first is Thompson's method [140], which is based on the theory of characteristics of

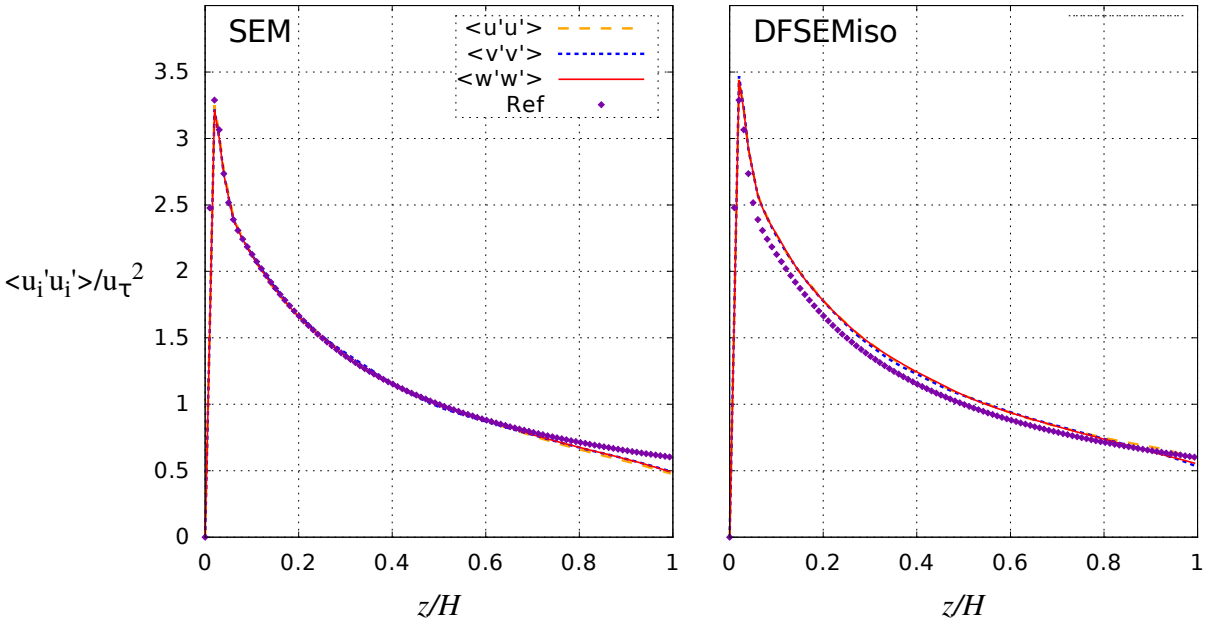

Figure 4.2: Reynolds stress vertical profiles prescribed using SEM and DFSEMiso.

the shallow water equations. Indeed, the method is applied to each plane of the grid, independently of others. It is also adapted to flows which are quasi-horizontal close to the open boundaries (i.e. the vertical velocity is about zero in these areas). When this is not the case, using the Thompson formulation may lead to inconsistencies, increasing numerical dissipation.

The second boundary condition at the outlet assumes that there is no change of the velocity components across the boundary. These conditions specify the pressure (or the water depth) and let the normal gradients of other variables than the normal velocity be null, which yields the set of the conditions [55]:

$$\begin{cases} p = p_{out} \\ \dfrac{\partial u_n}{\partial n} = 0 \end{cases} \tag{4.23}$$

For flow problems dominated by advection a special case of open boundary conditions is needed. The two methods proposed by TELEMAC-3D are not sufficiently efficient, and therefore influence the interior solution and cause instabilities with an LES approach. Due to this, a convective boundary condition has been developed

in TELEMAC-3D, which neglects the diffusive effects near the boundary and assumes that the flow is purely advective. It reads for the normal velocity u_n and $\boldsymbol{c}$ the convection velocity [60]:

$$\begin{cases} p = p_{out} \\ \dfrac{\partial u_n}{\partial t} + \boldsymbol{c}.\dfrac{\partial u_n}{\partial n} = 0 \end{cases} \tag{4.24}$$

which leads to a set of Dirichlet boundary conditions for the next time step.

4.1.4 Non-dissipative advection scheme

Especially for convection, Large-Eddy-Simulation requires high order (at least second order in time and space) and non-dissipative numerical schemes to finely reproduce turbulent scales in the flow. The convection patterns made available in TELEMAC-3D were not adequate:

- The characteristics method is at the order 1 in time and space.
- The SUPG formulation is at the order 1.5 in space with $P1$ finite elements [25].
- The distributive schemes (N and PSI) can reach the second order, but are too much dissipative. Indeed, these schemes prioritize the properties of positivity and conservation [41] [106].

Moreover, the use of a sigma transformation as well as theta time integration schemes ($f = \theta f^{n+1} + (1-\theta) f^n$) contribute to increase the numerical diffusion and the reduction of the different numerical schemes order. This drives the requirement of a new formulation, which is integrated in TELEMAC-3D, corresponding to a finite element centered formulation, based on the second order Adams-Bashforth time integration scheme [12, 42].
To solve a differential equation of the following form :

$$y' = f(t,y) \tag{4.25}$$

The second order Adams-Bashforth's scheme proposes an explicit writing with the following discretisation, between time steps Δt^- et Δt^+:

$$y^{n+1} = y^n + \frac{1}{2}\frac{2\Delta t^- + \Delta t^+}{\Delta t^-}\Delta t^+ f(t^n, y^n) - \frac{1}{2}\frac{\Delta t^+}{\Delta t^-}\Delta t^+ f(t^{n-1}, y^{n-1}) \tag{4.26}$$

With a constant time step Δt, it reads:

$$y^{n+1} = y^n + \frac{3}{2}\Delta t f(t^n, y^n) - \frac{1}{2}\Delta t f(t^{n-1}, y^{n-1}) \tag{4.27}$$

Once implemented, this scheme is tested and assessed with a TELEMAC-3D test case called "cone". This flow characterizes the circular transport of a passive cone-shaped tracer with respect to the vertical axis. In this simulation, the velocity field is fixed, being completely circular around the center of the domain (cf figure 4.3). As an initial condition, a conical concentration of a passive unit amplitude tracer is defined, as shown in figure 4.3.

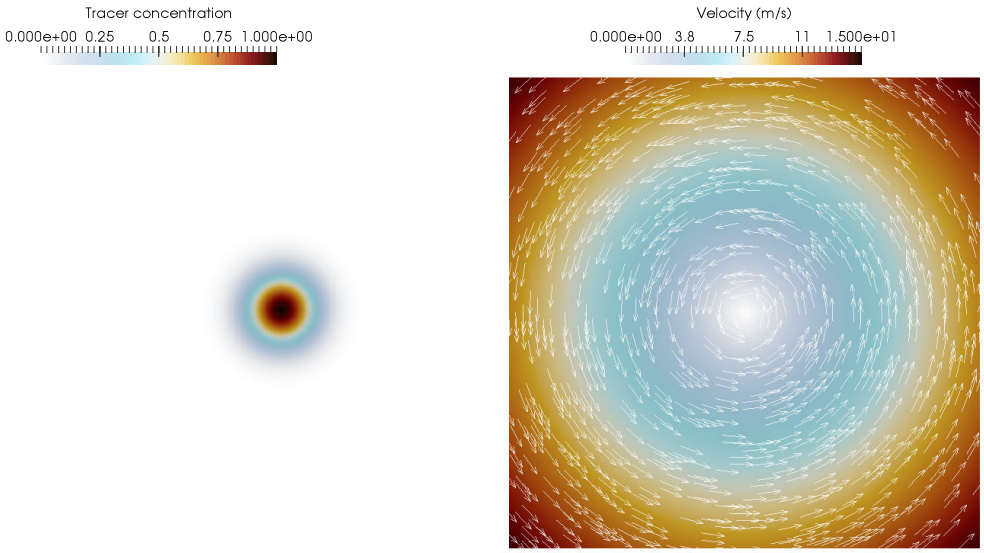

Figure 4.3: On the left : initial tracer concentration. On the right : Fixed velocity field.

After the time needed for the tracer to turn around and return to its initial position, the figure 4.4 presents the results obtained for some of the different convection schemes available in TELEMAC-3D as well as the new centered finite element formulation, based on the Adams-Bashforth time integration scheme.

These results show the low dissipation of the centered formulation. After the tracer did a round, the loss of this new scheme is only 0.2% whereas with the characteristic methods, the SUPG formulation and the PSI predictor-corrector scheme (2nd order) result in an amplitude loss of respectively 83%, 18% and 36%. Table 4.1 and Table 4.2 summarize respectively the dissipation rate achieved by the different

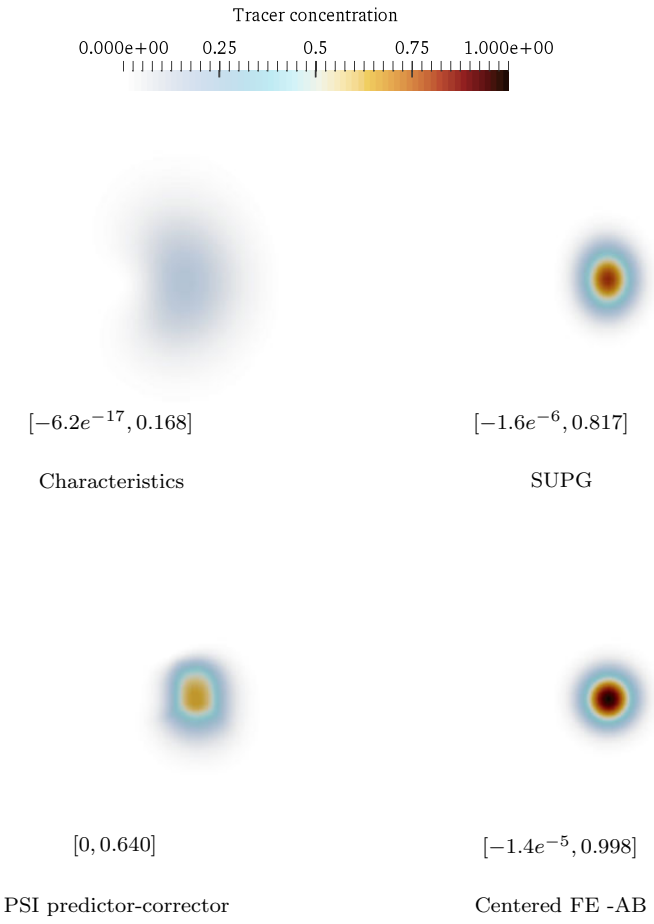

Figure 4.4: Concentration of tracer obtained after one turn for different convection schemes.

schemes after several tracer cycles, as well as the tracer mass conservation.

However, this scheme does not verify the positivity and conservativity properties as does the PSI distribution scheme. Also, using this centered formulation requires the use of low time steps to avoid instability (CFL> 0.2) [49]. In order to make sure that the scheme is of the second order in space, this same simulation was performed at a constant time step with several spatial discretisations. The $2D$ meshes used are unstructured grids. They are extruded vertically in a number of planes to keep the

Tracer cycle number	1	2	3	4
Characteristics	83.13%	90.81%	93.72%	95.30%
SUPG	10.61%	18.43%	24.50%	29.39%
PSI P-C	36.00%	49.06%	57.02%	62.02%
Centered FE-AB	0.18%	0.60%	1.13%	1.71%

Table 4.1: Maximum of tracer concentration loss obtained with several advection schemes.

Tracer cycle number	1	2	3	4
Characteristics	−10.00%	−23.05%	−35.93%	−47.34%
SUPG	0.00%	0.00%	0.00%	0.00%
PSI P-C	−0.07%	−0.38%	−0.99%	−1.92%
Centered FE-AB	0.00%	0.00%	0.00%	0.00%

Table 4.2: Tracer mass variation rate obtained with several advection schemes.

vertical and horizontal discretisation of the same order of magnitude.
When the cone has turned and theoretically returned to its initial position, the standard error L_2 is calculated from the initial time. Figure 4.5 presents the errors obtained in logarithmic scale, which clearly identifies the 2nd order in space of the new formulation implemented in TELEMAC-3D.

The second order Adams-Bashforth time scheme based centered formulation appears to be a good candidate as a velocity convection scheme for LES. Indeed, this model validates the order and non-dissipation properties required to efficiently transport flow fluctuations. Figure 4.6 shows the instantaneous velocity fields obtained in a flat channel with the different convection schemes available in TELEMAC-3D without only the molecular diffusion ($\nu = 10^{-6}\mathrm{m}^2\mathrm{s}^{-1}$), by using the artificial turbulence method presented in section 4.1.2.

4.1.5 New algorithm

The implementation of the new convection scheme in TELEMAC-3D requires a slight modification of the main algorithm of the solver. The main change lies in the convection and diffusion steps. Whereas TELEMAC-3D treats the advection

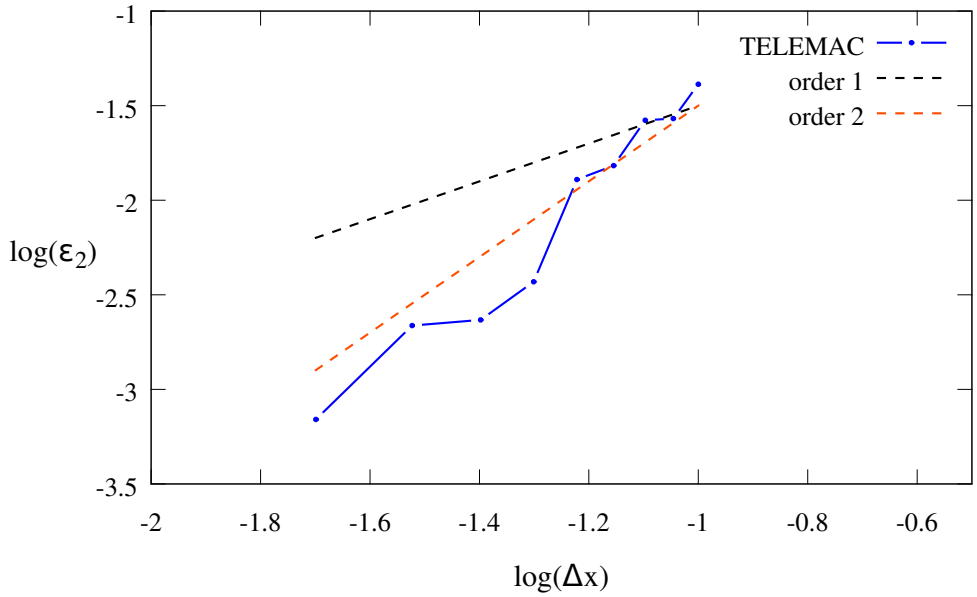

Figure 4.5: Spatial convergence graph for the centered finite element formulation based on the second order Adams-Bashforth time integration scheme.

terms and the diffusion terms separately for the horizontal velocities, the formulation allows the unification of these treatments in a single process. The advection-diffusion treatment relies on the Adams-Bashforth time integration scheme for the advective terms, and the Crank-Nicholson scheme for the diffusive terms. The step reads:

$$\begin{aligned} &\frac{\boldsymbol{u}^{a}-\boldsymbol{u}^{n}}{\Delta t}+\frac{3}{2}\left(\boldsymbol{u}_{c}^{n}.\boldsymbol{\nabla}\right)\boldsymbol{u}^{n}-\frac{1}{2}\left(\boldsymbol{u}_{c}^{n-1}.\boldsymbol{\nabla}\right)\boldsymbol{u}^{n-1} \\ &\qquad -(\nu+\nu_{T})(\frac{1}{2}\Delta\boldsymbol{u}^{a}+\frac{1}{2}\Delta\boldsymbol{u}^{n})=0 \quad \text{in} \quad \hat{\Omega} \end{aligned} \tag{4.28}$$

Then the algorithm solves the new surface elevation η as well as the hydrostatic step

$$\begin{cases} \dfrac{\boldsymbol{u}^{d}-\boldsymbol{u}^{a}}{\Delta t}+\dfrac{\boldsymbol{\nabla} p_{h}^{n+1}}{\rho}=\boldsymbol{g} \quad \text{in} \quad \hat{\Omega} \\ \dfrac{\eta^{n+1}-\eta^{n}}{\Delta t}+\nabla\cdot\displaystyle\int_{b^{n}}^{\eta^{n}}\boldsymbol{u}_{\boldsymbol{H}}^{\boldsymbol{d}}dz=0 \quad \text{on} \quad \Gamma_{s} \end{cases} \tag{4.29}$$

The continuity step aims to evaluate the new dynamic pressure by solving the Poisson equation and to compute the final velocities.

$$\begin{cases} \Delta p_{d}^{n+1}=-\dfrac{\rho}{\Delta t}\nabla\cdot\boldsymbol{u}^{\boldsymbol{d}} \quad \text{in} \quad \hat{\Omega} \\ \boldsymbol{u}^{n+1}=\boldsymbol{u}^{\boldsymbol{d}}+\dfrac{\Delta t}{\rho}\boldsymbol{\nabla} p_{d}^{n+1} \quad \text{in} \quad \hat{\Omega} \end{cases} \tag{4.30}$$

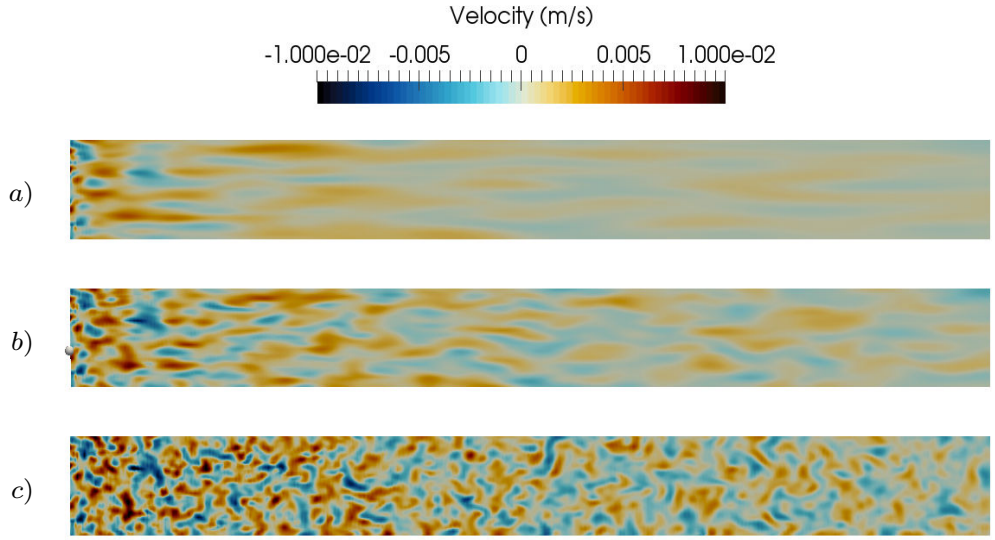

Figure 4.6: Instantaneous spanwise velocity obtained with the convection schemes a) characteristics method, b) SUPG, c) Centered Adams-Bashforth finite element formulation.

Finally, each iteration ends up constructing the effective viscosity (depending on the turbulence model) that will be used at the next time step.

4.1.6 Finite element arrays computation

The implementation of new turbulence models requires the computation of specific quantities such as the vorticity module Ω and the strain rate tensor norm S. These physical values have to be estimated in the finite element framework, by multiplying them by the test functions and by integrating the result on the typical mesh element (triangular with TELEMAC-2D and prismatic with TELEMAC-3D). Within the frame of Telemac-Mascaret system, P_1 finite element is chosen. This choice is mainly justified by the simplicity of implementation and by the fact that a major part of the variational formulation can be integrated analytically. Moreover, it guarantees a theoretical overall second order in space for the algorithm.

Taken f to be a given fluid quantity to derive over the coordinate x. The finite

element formulation involves the computation on each element Ω:

$$D_{fx} = \int_{\Omega} \frac{\partial f}{\partial x} \varphi_i d\Omega \tag{4.31}$$

where $\varphi_{i=1,N}$ designate the basis functions of the element Ω. As explained in Section 3.2, the TELEMAC-3D numerical framework relies on a reference element named Ω_r, motionless, for which the basis functions are $\psi_{i=1,N}$. Moreover, the quantity f is approximated using an interpolated formulation, i.e. $f = \sum_{i=1}^{N} f_i \varphi_i$ where f_i are the element nodal values. So the integrated derivative reads:

$$\begin{aligned} D_{fx} &= \int_{\Omega} \left(\sum_{i=1}^{N} \frac{\partial (\psi_i \circ G^{-1})}{\partial x} \right) \psi_i \circ G^{-1} d\Omega \\ &= \int_{\Omega} \left(\sum_{i=1}^{N} \boldsymbol{J}_{G^{-1}} \frac{\partial \psi_i}{\partial x} \circ G^{-1} \right) \psi_i \circ G^{-1} d\Omega \end{aligned} \tag{4.32}$$

where $\boldsymbol{J}_{G^{-1}}$ is the Jacobian matrix of the transformation G^{-1}. However, this array is equal to $\boldsymbol{J}_{G^{-1}} = \left(\boldsymbol{J}_G \circ G^{-1} \right)^{-1}$, which is also equivalent to:

$$\boldsymbol{J}_{G^{-1}} = \frac{1}{|\boldsymbol{J}_G \circ G^{-1}|} \, {}^{\top}\mathrm{Com}(\boldsymbol{J}_G \circ G^{-1}) \tag{4.33}$$

So now D_{fx} reads:

$$D_{fx} = \int_{\Omega} \left(\sum_{i=1}^{N} \frac{1}{|\boldsymbol{J}_G \circ G^{-1}|} \, {}^{\top}\mathrm{Com}(\boldsymbol{J}_G \circ G^{-1}) \frac{\partial \psi_i}{\partial x} \circ G^{-1} \right) \psi_i \circ G^{-1} d\Omega \tag{4.34}$$

By applying the function G to this integral, it simplifies into:

$$D_{fx} = \int_{\Omega_r} \left(\sum_{i=1}^{N} \frac{1}{|\boldsymbol{J}_G|} \, {}^{\top}\mathrm{Com}(\boldsymbol{J}_G) \frac{\partial \psi_i}{\partial x} \right) \psi_i |\boldsymbol{J}_G| d\Omega_r \tag{4.35}$$

Finally,

$$\boxed{D_{fx} = \int_{\Omega_r} \left(\sum_{i=1}^{N} \, {}^{\top}\mathrm{Com}(\boldsymbol{J}_G) \frac{\partial \psi_i}{\partial x} \right) \psi_i d\Omega_r} \tag{4.36}$$

For each non-linear term, some assumptions are considered to make easy the integration of their corresponding terms. High powers of flow quantities are assumed to be constant per element when they are linked to a non-linear term. Terms with high derivatives are integrated by part in order to retrieve the weak form of the variational formulation. These calculations have been performed using the formal computing software Mathematica.

4.1.7 Post-processing and turbulent structure identification

A final effort concerning the implementation of Large-Eddy-Simulation is to establish the post-processing procedures in order to calculate the average and fluctuating statistical fields during the simulation. This calculation results simply from a temporal averaging of the required quantities, such as the averaged velocities and the six Reynolds stress components. Once the flow is well established, the contributions from each time step are taken into account over a sufficiently long period to have representative statistical data.

The vorticity modulus is a good indicator of coherent structures. It can be computed easily in the whole calculation domain, so it is sufficient to define a threshold value of this quantity, above which a vortex can be identified. However, the problem arises when the vorticity is examined near solid walls. Due to friction, most of the vorticity production occurs in these areas, and it is therefore very difficult to define a unique threshold value to observe all the turbulent structures.

In [69], turbulent structures are identified using the second invariant of the velocity gradient tensor, called Q criterion. This quantity is computed with:

$$Q = \frac{1}{2}\left(\Omega^2 - S^2\right) \tag{4.37}$$

where Ω is the vorticity modulus and S is the strain rate tensor norm. A point of space where the rotation takes precedence over the energy dissipation will be associated with a positive Q criterion, and thus belongs to a swirling structure.

Another criterion named λ_2 [75] is based on local minima of pressure investigation. The Hessian matrix of pressure can be expressed by writing the symmetric part of the Navier-Stokes equations. Then, the swirling terms can be isolated, and the study involves computing the eigenvalues of the tensor $\bar{\bar{\Omega}}^2 + \bar{\bar{S}}^2$, which are real since this tensor is symmetric. In the case of the search for a minimum pressure, two of the eigenvalues ($\lambda_1 < \lambda_2 \leq \lambda_3$) must be positive. Finally, a local minimum of pressure can be identified with the criterion:

$$\lambda_2 \leq 0 \tag{4.38}$$

The several developments performed in TELEMAC-3D are summarized in Table 2, 1 and 3.

The developments presented in the previous section are here used to validate their implementation in TELEMAC-3D. Flows for which experimental measurements are available are reproduced numerically. The results obtained with the LES approach are then compared with these data, which are mainly the statistics (mean velocity profiles, Reynolds stresses) of the turbulent flows. A good representation of these statistics enables the study of instantaneous phenomena, such as vortices identification.
The calculations presented hereafter have been performed on the EDF clusters named Athos and Porthos for which some characteristics are presented in Table 4.3.

	Quantity	CPU Model	RAM
Athos	776	Intel Xeon E5-2600 V2 Ivy Bridge 2.7GHz	64Go
Porthos	585	Intel Xeon E5-2697 V3 2.60GHz (Haswell)	64Go

Table 4.3: EDF Clusters characteristics

4.2 A first validation: Flow past a cylinder

This test case describes a flow past cylindrical pier at a Reynolds number (based on the bulk velocity and the pier diameter) of $Re = 3900$. The pier diameter is $D = 6.3$cm, the bulk velocity is 0.0619 ms^{-1} and the averaged water depth is $h = 3D$. Similar flows have been very commonly studied both experimentally and numerically [28, 66, 109], providing a significant database to compare results.

The flow is discretised over a $20D$ long and $10D$ wide domain, with the pier placed at $5D$ downstream of the inlet section, as illustrated in Figure 4.7. The horizontal grid resolution is approximately 0.55mm at the boundary of the pier and 8mm elsewhere, and the horizontal mesh is extruded over 32 σ-layers along the vertical axis. This resolution corresponds to near wall dimensionless grid spacings of $\Delta x^+ = \Delta y^+ = 1.7$ and $\Delta z^+ = 18$, which match with the recommendations for LES from [112] (see Table 2.1). At the boundaries, a no-slip boundary condition is applied at the pier boundaries and a slip boundary condition at the lateral walls. The bottom is defined with a very small roughness with a Nikuradse law $k_s = 10^{-4}$m. At the inlet, a Reichardt profile is used [148] and a non reflecting boundary condition (see section 4.1.3) is applied at the outlet. Finally, the Smagorinsky model and the WALE model are used as subgrid model.

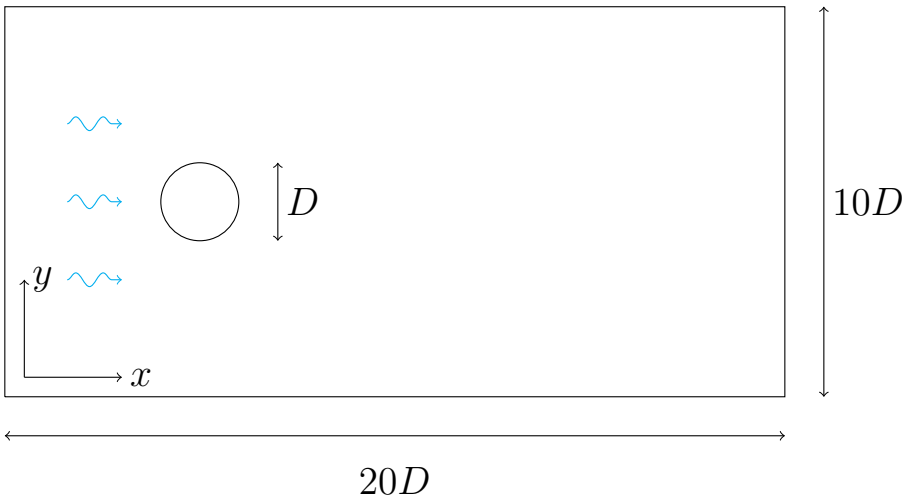

Figure 4.7: Sketch of geometry of the flow past a cylindrical pier.

Figures 4.8 and 4.9 show respectively the averaged streamwise velocity and the

averaged spanwise velocity profiles along the centerline of the cylinder obtained with TELEMAC-3D and compared with the experimental results from [109], obtained using a Particle Image Velocimetry (PIV) method. The agreement between LES results and experimental data is very good for both components of velocity, particularly for those obtained with the LES model, which fit perfectly with the experimental data.

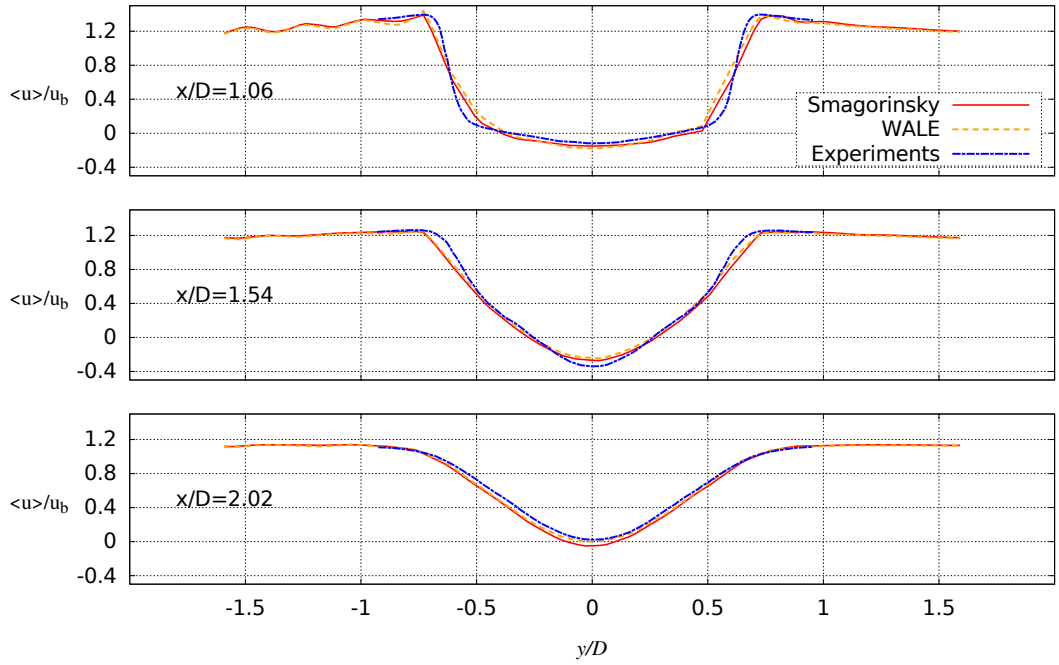

Figure 4.8: Comparison of the lateral profiles of averaged streamwise velocity obtained with LES (Smagorinsky and WALE models) with experimental results from [109].

The comparison of Reynolds stresses $< u'u' >$ and $< v'v' >$ profiles are presented in Figures 4.10 and 4.11. Here again the agreement of both methods is good. The WALE model seems to give better results near the pier but overestimates slightly the turbulent quantities in the wake.

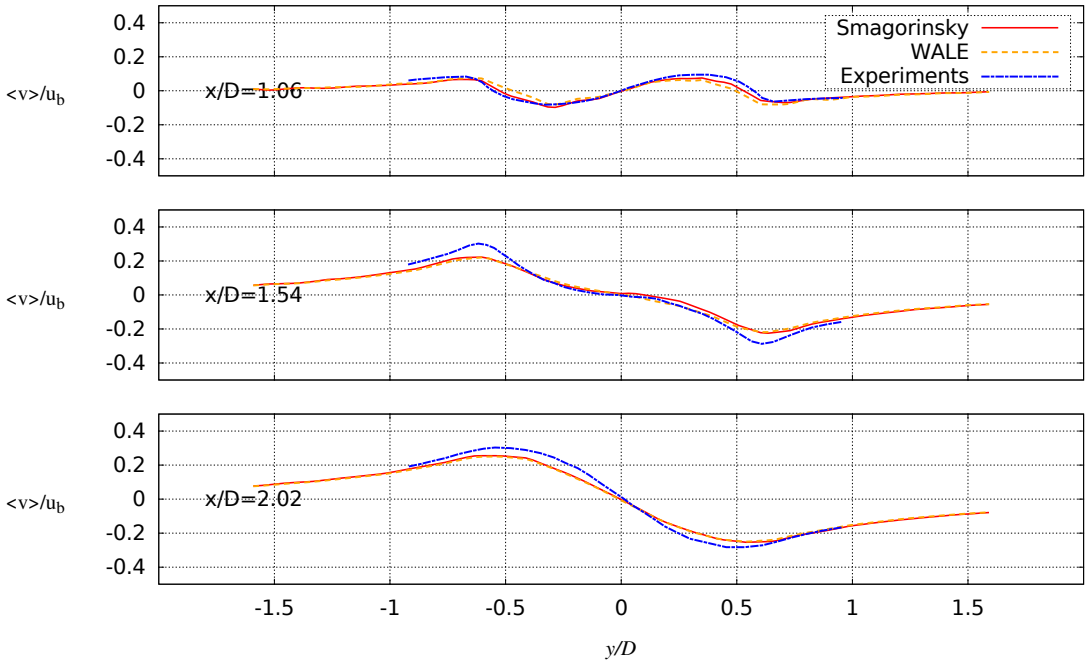

Figure 4.9: Comparison of the lateral profiles of averaged spanwise velocity obtained with LES (Smagorinsky and WALE models) with experimental results from [109].

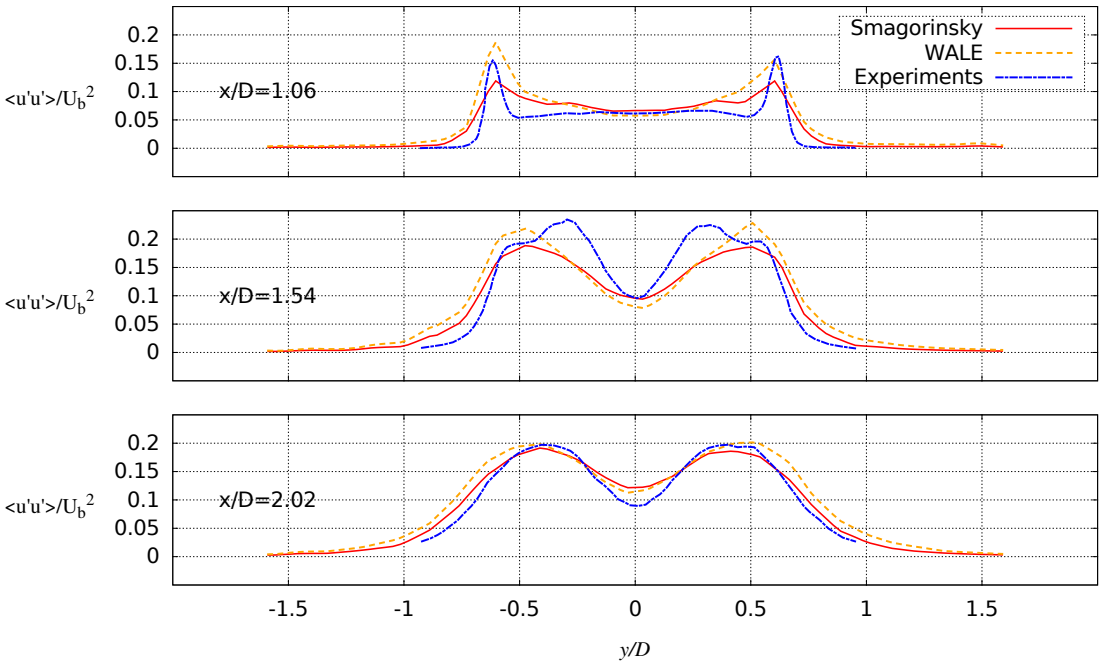

Figure 4.10: Comparison of the lateral profiles of Reynolds stress $< u'u' >$ obtained with LES (Smagorinsky and WALE models) with experimental results from [109].

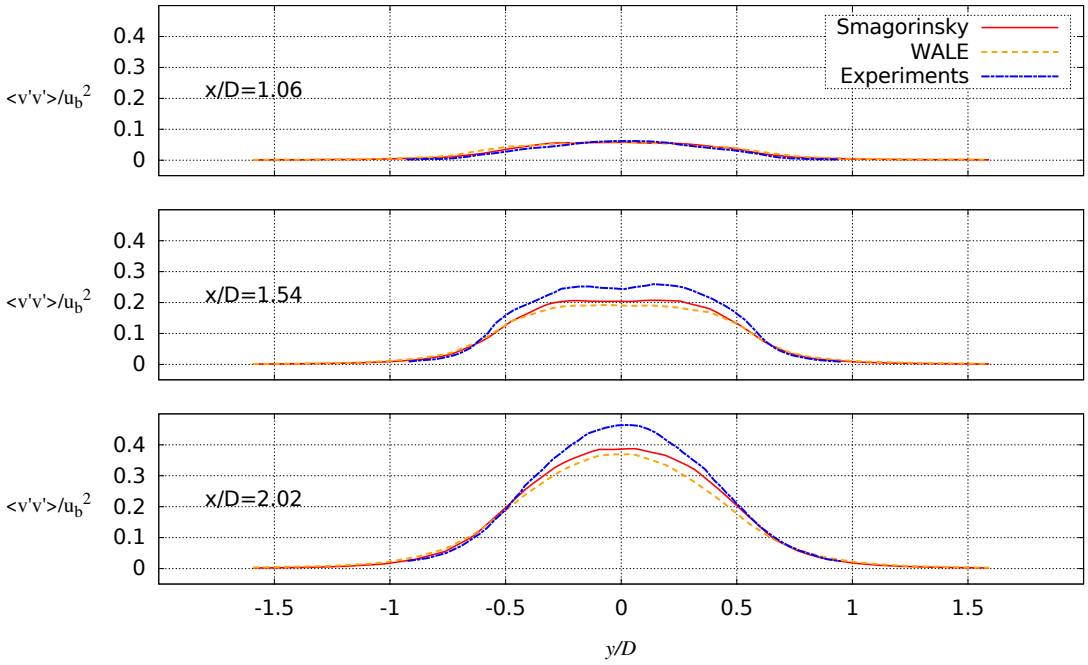

Figure 4.11: Comparison of the lateral profiles of Reynolds stress $< v'v' >$ obtained with LES (Smagorinsky and WALE models) with experimental results from [109].

Turbulence statistics obtained with both subgrid models are overall in agreement with experimental data. The WALE model gives a slightly better description of the flow, which was expected with the use of no slip boundary conditions on the pier, since this model was designed to such an application. Figure 4.12 presents the comparison of the turbulent structures identified with the Q and λ_2 criteria. In this case the λ_2 criterion is much more efficient, since conversely to Q, it allows to identify very elongated turbulent structures in the wake.

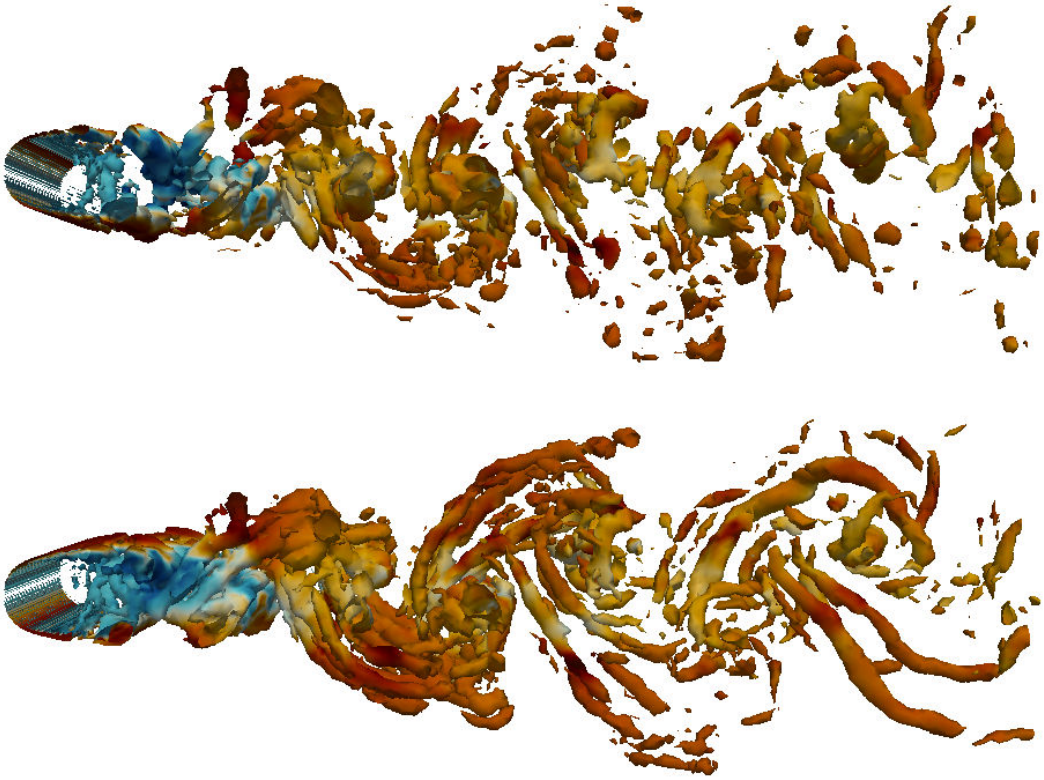

Figure 4.12: Turbulent structures identified with the Q (at the top) and λ_2 (at the bottom) criteria, coloured by the velocity magnitude.

4.3 An initial case study with a complex bathymetry: Flow over dunes

4.3.1 Experimental setup

The acquired experimental data characterizes a turbulent open channel flow over two-dimensional dunes, chosen since it is quite representative of the flow patterns in tidal sites. In this setup, the dune height is $H = 0.08$m and its length is $L = 1.6$m. All other dimensions are given in Figure 4.13. This flow has been studied firstly in [145] with Laser Doppler Velocimetry (LDV) measurements, over a train of three dunes (with a bed roughness to $k_s = 1.6$mm) in a 1.5m wide flume. The maximum flow depth is $h = 0.294$m. With a water discharge of $0.149\text{m}^3\text{s}^{-1}$ in the flume, the corresponding bulk velocity is $U_b = 0.394\text{ms}^{-1}$ and the Reynolds number is approximately 10^6.

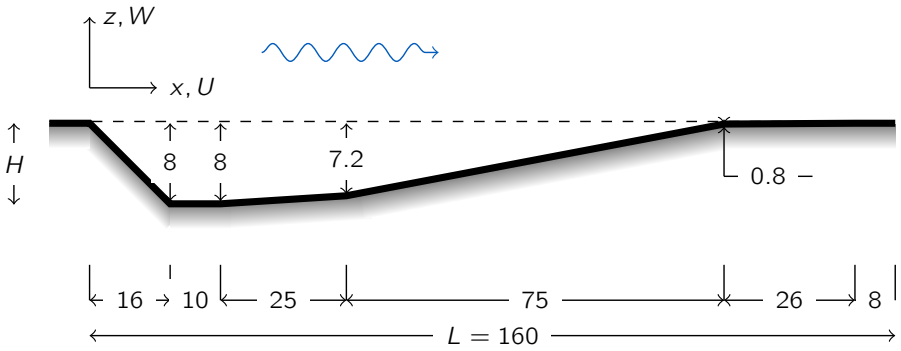

Figure 4.13: Dune profile in the plane (x, z). Dimensions in centimeters.

Measurements were taken on sixteen vertical profiles along the dune. The quantities collected are the averaged streamwise and vertical velocities ($< u >$ and $< w >$ respectively), three Reynolds tensor components ($< u'^2 >$, $< w'^2 >$ and $< u'w' >$) and the turbulent kinetic energy k. Here indexation $< f >$ refers to an average quantity and f' to the component fluctuating with respect to this average ($f' = f - < f >$).

4.3.2 Numerical setup and settings

A single dune has been modeled with TELEMAC-3D based on a 1m wide space domain. Three different grid resolution have been used. The finest mesh (indented with f) is composed of about 1.2×10^6 points. In wall units, and assuming the veloc-

ity friction equal to $u_\tau = 0.02\text{ms}^{-1}$, the dimensionless grid spacings are $\Delta x^+ = 160$, $\Delta y^+ = 120$ and $\Delta z^+ \approx 100$, which correspond to suitable scales according to [112] (in which the recommended LES grid spacings are $\Delta x^+ = 100 - 600$, $\Delta y^+ = 100 - 300$ and $\Delta z^+ = 50 - 150$ with the use of a wall model). A second grid is defined (indented with m) in order to fit with the maximum spacing recommendations, and a third one is coarser (indented with c). For these configurations the time step is set such that the CFL number is of the order of 0.15.

As inlet boundary condition, the mean velocity components of the last vertical profiles (corresponding to the position $x = 1.580\text{m}$ of the previous dune in the experimental configuration) are used to define the inflow boundary condition of the numerical model. To prescribe the inflow turbulence, the Synthetic Eddy Method is used. The Reynolds stresses components are given by the experiments. Both the mean flow and the turbulence incoming from the previous dunes of the experimental setup are reproduced at the inlet of our computational domain. As the turbulent dissipation rate ε is not provided by the experiments, it is evaluated by using a theoretical law for open channel flow which reads [148]:

$$\begin{aligned} \varepsilon &= \varepsilon^+ \frac{u_\tau^4}{\nu} \\ \varepsilon^+ &= \frac{1}{\kappa} \frac{1}{(z^{+4} + 15^4)^{1/4}} \\ z^+ &= \frac{\Delta z u_\tau}{\nu} \end{aligned} \tag{4.39}$$

where Δz is the distance to the bottom. Large-Eddy-Simulation results are compared to these experiments at six positions, defined by the locations $x = 6\text{cm}$, $x = 13\text{cm}$, $x = 21\text{cm}$, $x = 43\text{cm}$, $x = 70\text{cm}$ and $x = 127\text{cm}$ and which we will denote respectively L_1, L_2, L_3, L_4, L_5 and L_6 hereafter.

Figure 4.14 presents the averaged streamwise velocity and the Reynolds stresses $< u'^2 >$ and $< w'^2 >$. The comparison with experimental data shows that, with the three space discretisations, the model gives satisfactory averaged velocity profiles. However, concerning the second order statistics, the coarser grids do not model accurately the Reynolds stresses, particularly the $< w'^2 >$ component. That is why the finer mesh is used hereafter.

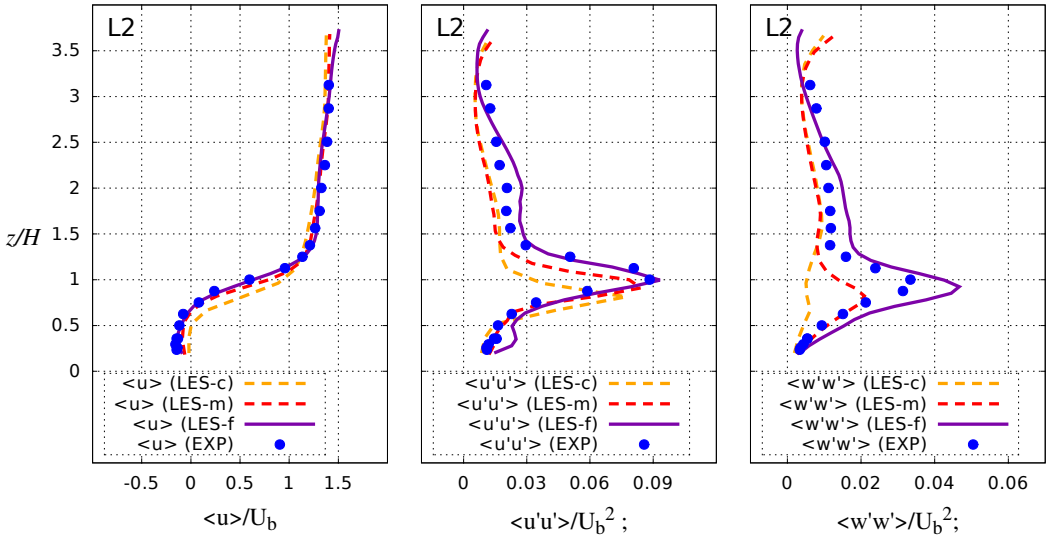

Figure 4.14: Statistics of the flow obtained with the three grids.

4.3.3 Statistics in the channel

Figure 4.15 shows the comparison of the LES with the experimental data over six vertical profiles for the mean streamwise velocity component and the mean vertical velocity, both normalized by the bulk velocity. The agreement is overall good, particularly for the streamwise velocity. Regarding the vertical velocity, it is slightly overestimated (in terms of magnitude) at the location $L3$ and $L6$. In Figure 4.16, the Reynolds stress $< u'^2 >$ and the turbulent kinetic energy k (normalized by the square of bulk velocity) are displayed. The agreement between predicted quantities and experimental data is excellent. The calculation yields a peak energy in the separated shear layer at the same altitude and the same intensity, despite a very small discrepancy for the streamwise Reynolds stress at the position $L5$. Figure 4.17 presents the comparison of the Reynolds stresses $< w'^2 >$ and $< u'w' >$ along the vertical profiles. Here again the agreement with measurements is also good with nevertheless a few discrepancies at the locations $L3$ and $L5$. Figure 4.18 shows average free surface deviation from its average ($z_a = 0.294$m) and normalized by the dune height along the streamwise axis compared by data from experiments [145]. The agreement is overall good, except at the inflow, where the numerical model yields an overestimation of the free surface elevation that is not observable in experiments.

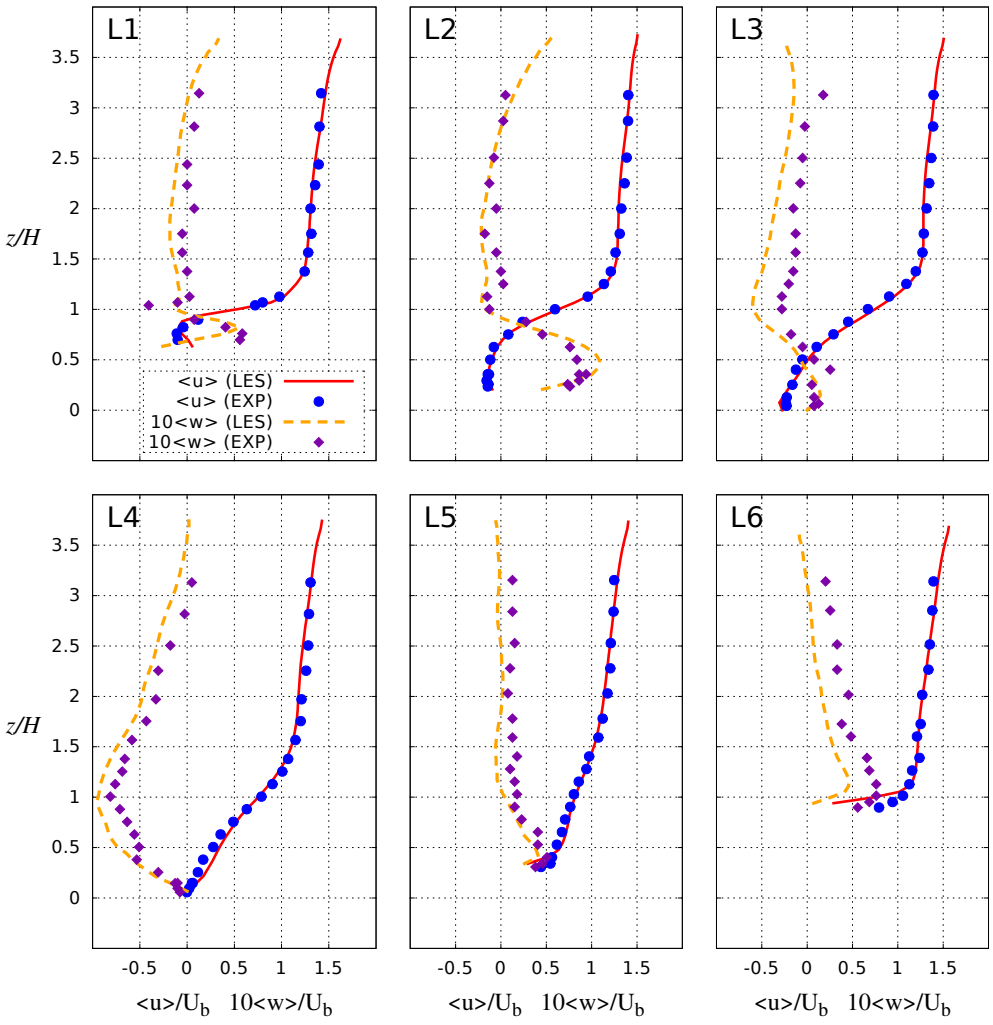

Figure 4.15: Comparison of averaged streamwise and vertical velocity profiles obtained with LES and the experiments from [145]. The vertical velocity component is represented with a factor 10.

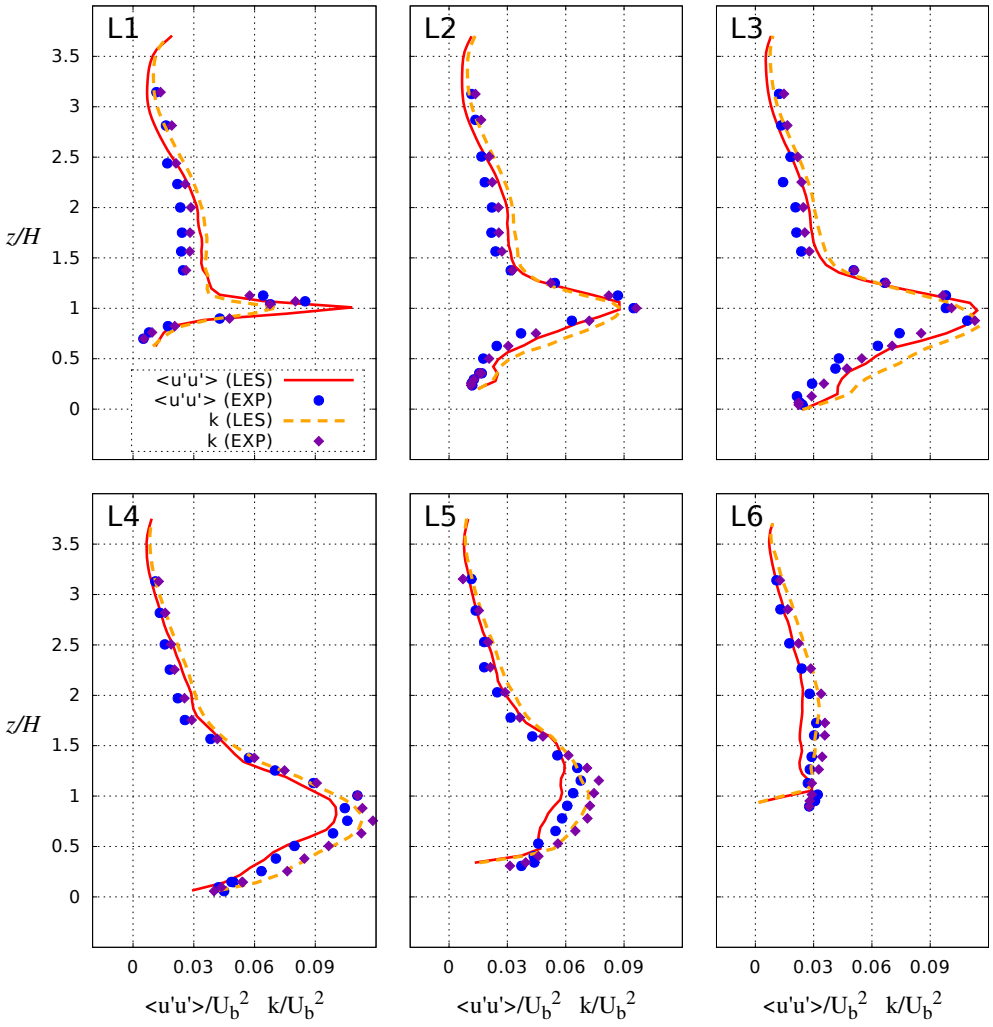

Figure 4.16: Comparison of vertical profiles of the Reynolds stress $< u'^2 >$ and the turbulent kinetic energy k, obtained with LES and the experiments from [145].

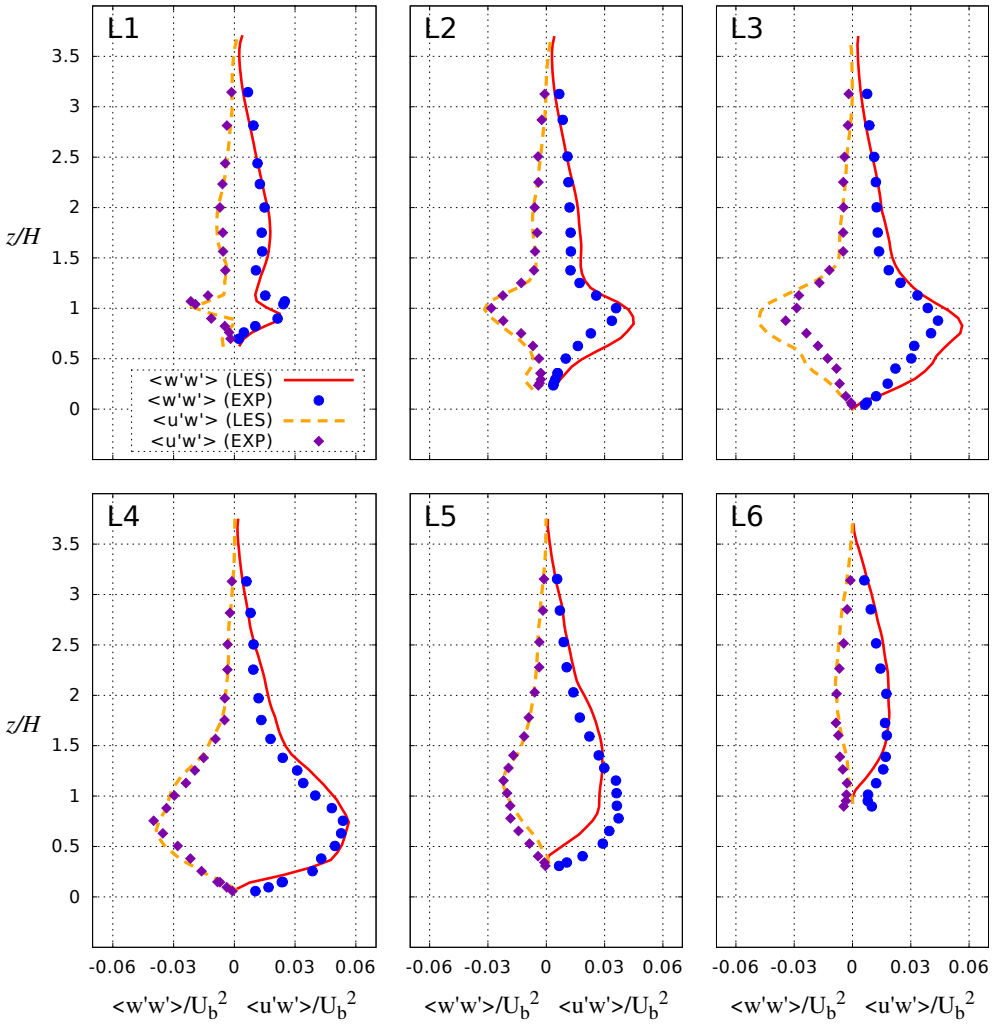

Figure 4.17: Comparison of vertical profiles of the Reynolds stresses $< w'^2 >$ and $< u'w' >$ obtained with LES and the experiments from [145].

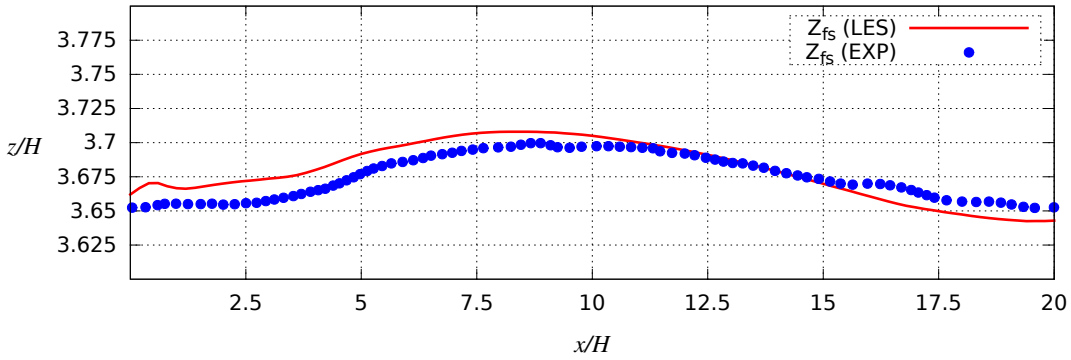

Figure 4.18: Comparison of the mean free surface elevation along the streamwise axis obtained with LES and the experiments from [145].

4.3.4 Coherent eddies identification

The instantaneous flow is subsequently investigated. Isosurfaces of λ_2 criterion [75] enables the identification of the several turbulent structures involved in this flow, illustrated in Figure 4.19 in which the turbulent structures are coloured using their elevation in the water column.

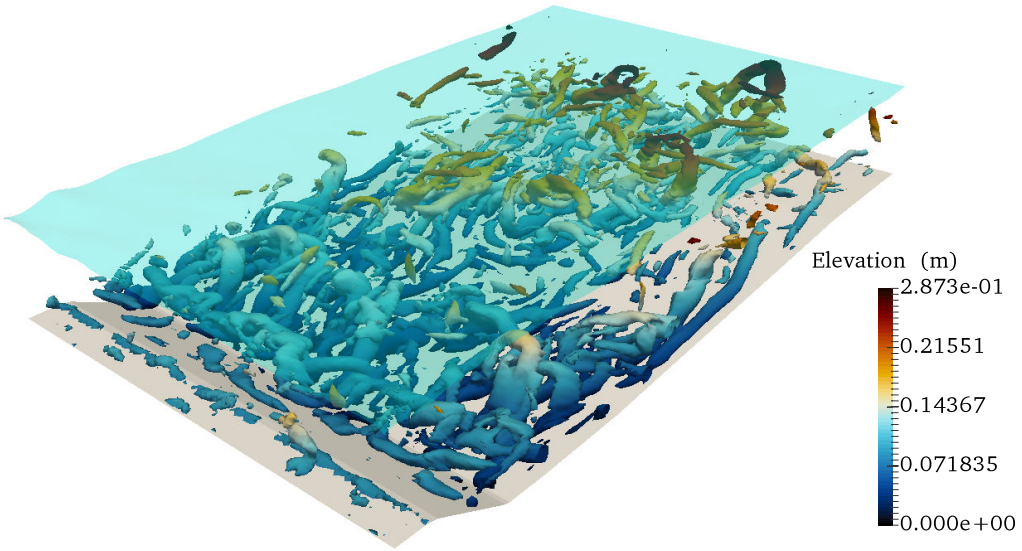

Figure 4.19: Instataneous isosurfaces of λ_2 criterion.

To identify more easily the turbulent structures induced by the dune, the inflow

turbulence has hereafter been suppressed in the simulations. It is also possible to observe discernibly the birth of a hairpin vortex [77, 63] and its progression by juxtaposing several snapshots of an isolated isosurface, as shown in Figure 4.20. As the

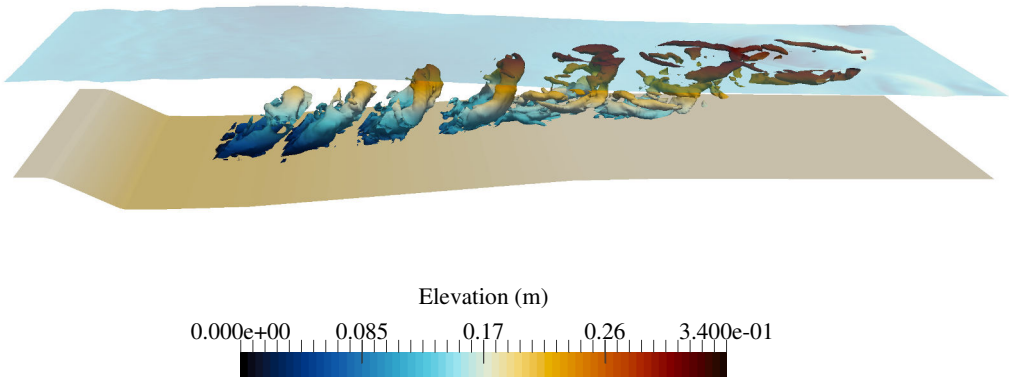

Figure 4.20: Isosurfaces of λ_2 criterion, showing the evolution of a hairpin vortex into a boil.

vortex propagates in the flow, it reaches the free surface. This upwelling is described in [16], in which a schematic model for the interaction of dune-related turbulence with the flow surface is proposed. Figure 4.21 aims to replicate the different stages of this interaction described in [16] by displaying snapshots of the velocity deflection in the plane (x,z) obtained with LES. In these snapshots, λ_2 criterion allows the vortex centers depiction, coloured in black. It highlights the transverse vorticity supporting the vortex during its upwelling. When the tip of the vortex reaches the free surface, this vorticity introduces a shear with the mean flow, that generates a ripple at the free surface. When the vortex pierces the water surface, these ripples turn into a boil which expands as it moves forward, as described in [16]. Figures 4.22 and 4.23 present respectively the effect of such turbulent structures on the free surface. The boil expansion is shown in Figure 4.22, which displays snapshots of velocity deviation at the free surface plane. The upper picture corresponds to the achievement of a

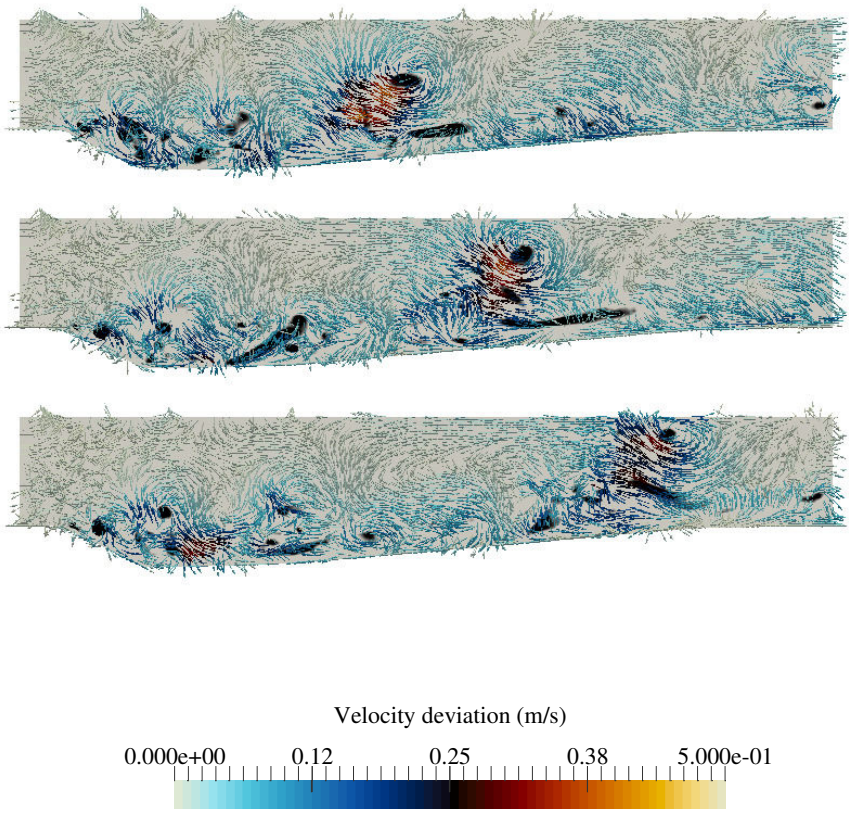

Figure 4.21: Snapshot of the velocity deviation in the (x,z) plane.

hairpin vortex at the water surface, which moves forward and swell in the lower pictures. At the same time, the corresponding free surface deviation (from its average value) is shown in Figure 4.23. The ripple is easily distinguishable at the top. In the lower part of the figure, the wavelet moves forward and becomes circular in shape. These results are in agreement with the description proposed in [16]. However, these numerical simulations do not allow the distinction of the vortex legs erupting at the free surface nor the development of two small vortex tubes behind the boil.

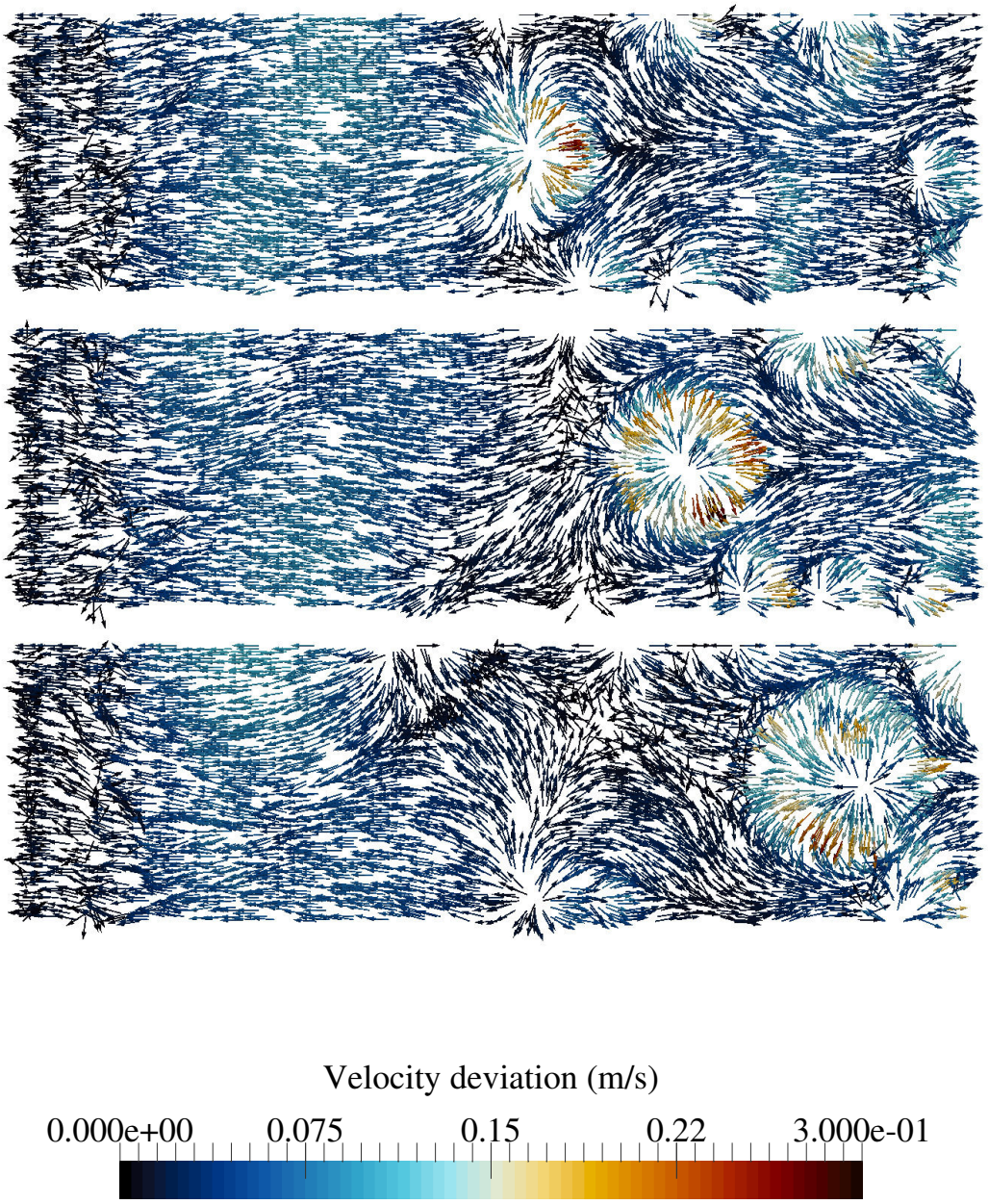

Figure 4.22: Snapshot of the velocity deviation at the free surface.

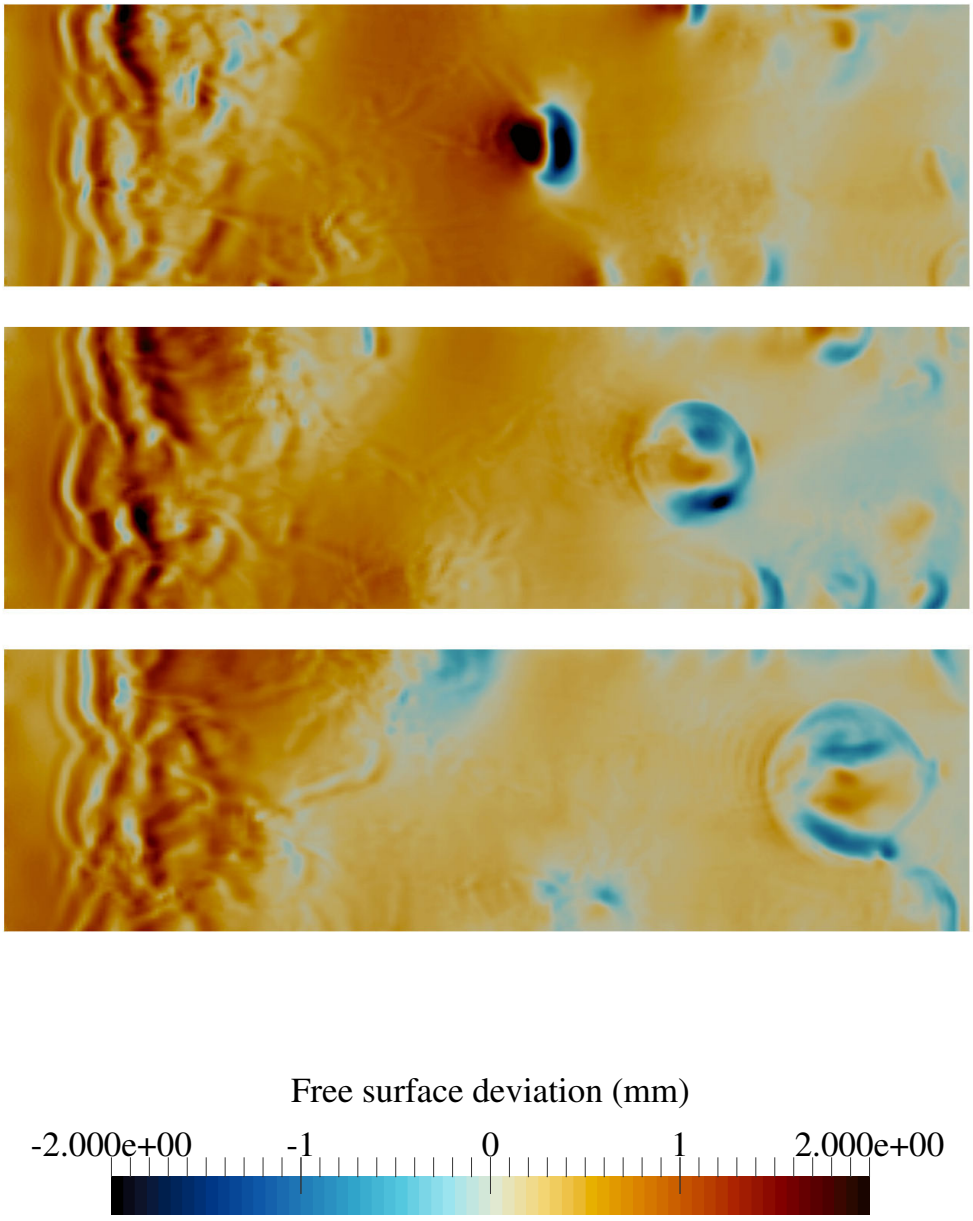

Figure 4.23: Snapshot of the free surface deviation.

4.4 Embedded LES: A strategy to model tidal flows

To investigate turbulence in tidal flows, both the tide scales and the turbulent scales have to be considered. The computational domain must be large enough to allow the tide forcing (based on the TPXO database) to be efficient and of course to cover the Alderney Race site, which is in the order of magnitude of a dozen of kilometers. Moreover, the grid resolution has to be fine enough to overly dissipate the turbulent fluctuations present in the flow. According to the prospective application (see section 4.5.2), the targeted grid sizes are 5 meters for the horizontal directions, and 1 meter over the vertical. The discretisation of such a domain with this resolution would require a two dimensional grid composed of about 10 millions points, extruded in 50 layers over the vertical. However, half a billion degrees of freedom calculation is not affordable with the actual computational resources.

4.4.1 Concept

An embedded LES method has thus been developed. The main idea is to use a coarse discretisation over a large grip Ω. Then, a parcel is defined in this domain, on which the LES method is going to be used. This part is noted Ω_{LES}, and Ω_{RANS} is defined as $\Omega \setminus \Omega_{LES}$. Figure 4.24 illustrated a simple sketch of this domain decomposition. The coupling between the two turbulence modelling approaches can be treated with different methods, and varies depending on the interfaces. A method proposed in [103] consists first of filtering the LES velocity fields to remove the frequencies corresponding to turbulence, then to reconstruct the RANS turbulent viscosity using the filtered quantities. Regarding the information transfer from RANS to LES, it can be enriched using similar methods to those used for typical inlet LES boundary conditions, i.e. periodic boundary condition or synthetic turbulence.

For the targeted applications, the RANS models proposed in TELEMAC-3D were not satisfying in terms of robustness and computational speed. Another RANS model has been selected: the Spalart-Allmaras model, which has nevertheless to be implemented. Between scalar zero-equation models and two-equations models, this one-equation model could be an optimal compromise in terms of computational time but also in terms of richness of the turbulence sources (production, destructions), transport and diffusion. As presented in the section 4.4.2, this model leads to very

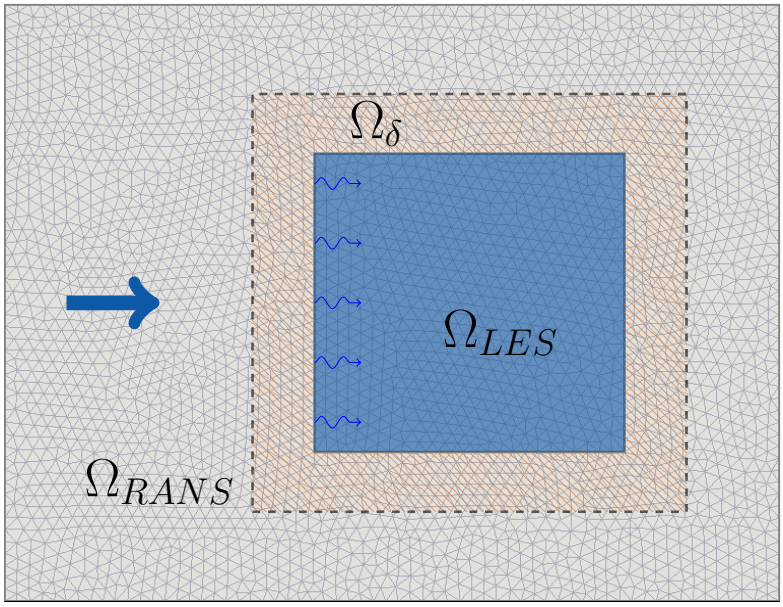

Figure 4.24: Main concept of the embedded LES method.

good results and allows the reconstruction of the required turbulence quantities. It is both faster and more stable than the $k-\varepsilon$ model. The synthetic turbulence generation introduced at the interfaces of the embedded LES requires the prescription of a Reynolds stress tensor as well as the vortices size. The latter are directly evaluated from the turbulence quantities k and ε estimated with the Bradshaw formula (see section 4.4.2).

The coupling has been implemented in such a way that the only required input is a polygone, defined by N_p points of coordinates (x_i^p, y_i^p). This polygon will then define the LES subdomain. From this, the initialisation step attributed to each mesh point its turbulence model, i.e. if its belongs to the RANS domain, the LES domain or if it is on one of the RANS-LES interfaces. The RANS turbulence approach is applied in Ω_{RANS}, but also in Ω_{LES}. However in this case, the turbulence viscosity is computed from the filtered velocity field (filtering based on multiple mass-lumping operations and temporal averages). In this way, the RANS data is computed in the whole computational domain, which avoids introducing discontinuity problems. Afterwards the RANS viscosity in Ω_{LES} is switched by a subgrid viscosity from a LES model. A buffer domain (called Ω_δ in Figure 4.24) has finally be defined to smooth

the transition process between the RANS and LES techniques.

In order to enrich the flow statistics from Ω_{RANS} to Ω_{LES}, an artificial turbulence method (based on DFSEMiso) is used at the corresponding interfaces. For each segment of the LES polygonal subdomain, a virtual eddy box is created (see section 4.1.2). The vortice length scale and intensity are evaluated by using the RANS model estimations of the turbulent kinetic energy k and of the turbulent dissipation rate ε estimated with the Bradshaw formula (see Equation 4.50). The artificial turbulence is assumed to be isotropic, and the three diagonal stresses read:

$$\begin{cases} < u'u' >= (4/5)k \\ < v'v' >= (4/5)k \\ < w'w' >= (2/5)k \end{cases} \tag{4.40}$$

This turbulence is finally injected at the interfaces nodes as a source term in the Navier-Stokes equations. As the subgrid model, the AMD model has been chosen since it has demonstrated its efficiency on very coarse grids (cf section 4.5.2).

4.4.2 Spalart-Allmaras model

The Spalart-Allmaras model was first introduced in [133] to deal mainly with aerodynamic problems. Since then, it has been widely used by the research community [87] and even in some industrial softwares (Code_Saturne, Code_Elsa). The Spalart-Allmaras turbulence model solves one transport equation for a viscosity-like variable $\tilde{\nu}$. Taking into account production, destruction and diffusion terms, the associated turbulent eddy viscosity ν_t is defined as:

$$\nu_t = \tilde{\nu} f_{v1}, \quad f_{v1} = \frac{\chi^3}{\chi^3 + C_{v1}^3} \tag{4.41}$$

where $\chi = \tilde{\nu}/\nu$. The viscosity-like variable $\tilde{\nu}$ is computed by the resolution of the following equation:

$$\begin{aligned} \frac{\partial \tilde{\nu}}{\partial t} + u_j \frac{\partial \tilde{\nu}}{\partial x_j} =& C_{b1}(1 - f_{t2})\tilde{W}\tilde{\nu} - (C_{w1} f_w - \frac{C_{b1}}{\kappa^2} f_{t2}) \left(\frac{\tilde{\nu}}{d}\right)^2 \\ &+ \frac{1}{\sigma}\left[\frac{\partial}{\partial x_j}\left((\nu + \tilde{\nu})\frac{\partial \tilde{\nu}}{\partial x_j}\right) + C_{b2}\frac{\partial \tilde{\nu}}{\partial x_i}\frac{\partial \tilde{\nu}}{\partial x_i}\right] \end{aligned} \tag{4.42}$$

The production term involves a modified vorticity and a damping function, respectively given by:

$$\tilde{W} = W + \frac{\tilde{\nu}}{\kappa^2 d^2} f_{v2}, \quad f_{t2} = C_{t3} \exp(-C_{t4}\chi^2) \tag{4.43}$$

in which d is the distance from the field point to the nearest solid wall

$$f_{v2} = 1 - \frac{\chi}{1+\chi f_{v1}}, \quad W = \sqrt{2\Omega_{ij}\Omega_{ij}} \quad \text{and} \quad \Omega_{ij} = \frac{1}{2}\left(\frac{\partial u_i}{\partial x_j} - \frac{\partial u_j}{\partial x_i}\right) \tag{4.44}$$

The terms in the destruction part are defined as:

$$f_w = g\left[\frac{1+C_{w3}^6}{g^6+C_{w3}^6}\right]^{1/6}, \quad g = r + C_{w2}(r^6 - r), \quad r = \min\left(\frac{\tilde{\nu}}{\tilde{W}\kappa^2 d^2}, 10\right) \tag{4.45}$$

The model makes use of several constants such as the Von Karman constant $\kappa = 0.41$ and the Prandlt constant $\sigma = 2/3$. Other constants originally proposed by the authors in [133] are $C_{b1} = 0.1355$, $C_{b2} = 0.622$, $C_{v1} = 7.1$, $C_{w1} = 3.24$, $C_{w2} = 0.2$, $C_{w3} = 2$, $C_{t3} = 1.2$ and $C_{t4} = 0.5$.

To compute the production and destruction terms, we need to compute the distance d of any node of the mesh to the closest solid boundary. The effort in calculating d can be a significant fraction of the total solution time [144]. For *small* serial (not parallel) softwares, this task can be performed once at the pre-processing step using a classical double loop (one loop over all the mesh nodes and another loop over boundary nodes). However, this algorithm is not compatible with parallel runs where the whole domain is partitioned into subdomains distributed over a number of threads or CPUs. To overcome this task, the algorithm proposed by [144] has been selected. This approach includes the resolution of a Poisson equation which is an efficient and easily parallelable task.

As boundary conditions, $\tilde{\nu}$ has been imposed to be equal to $\tilde{\nu}_{min} = 10^{-6}$ at the solid walls. On liquid boundaries as well as for the initial condition, the viscosity-like variable is assumed to be given by:

$$\tilde{\nu} = C_{\tilde{\nu}} h u_\tau \tag{4.46}$$

In the finite element framework, the implementation of the Spalart-Allmaras model involves solving the strong form of the variational formulation of the equation

4.42. Given any arbitrary set of test functions ψ_i, it reads:

$$\begin{aligned}\int_\Omega \frac{\partial \tilde{\nu}}{\partial t}\psi_i d\Omega + \int_\Omega \boldsymbol{u}.\nabla\tilde{\nu}\psi_i d\Omega = \underbrace{C_{b1}\int_\Omega (1-f_{t2})\tilde{\nu}\tilde{W}\psi_i d\Omega}_{P} \\ \underbrace{-\int_\Omega (C_{w1}f_w - \frac{C_{b1}}{\kappa^2}f_{t2})\left(\frac{\tilde{\nu}}{d}\right)^2\psi_i d\Omega}_{D} \\ \underbrace{+\int_\Omega \frac{1}{\sigma}\nabla.((\nu+\tilde{\nu})\nabla\tilde{\nu})\,\psi_i d\Omega}_{T1} \underbrace{+\frac{C_{b2}}{\sigma}\int_\Omega (\nabla\tilde{\nu})^2\psi_i d\Omega}_{T2}\end{aligned} \tag{4.47}$$

For each non-linear source term, some assumptions are considered to ease the integration of their corresponding terms in 4.47. High powers and high derivatives of $\tilde{\nu}$ and the velocity components are assumed to be constant per element when they are linked to a non-linear term. Hereafter, the final expression of each term of 4.47 are given. The production term (see equation 4.42) is computed by evaluating explicitly P given by:

$$P \approx C_{b1}(1-f_{t2}(\tilde{\nu}^n))\tilde{W}^n\tilde{\nu}^n\int_\Omega \psi_i d\Omega \tag{4.48}$$

In the destruction term, due to the non linearity on $\tilde{\nu}^2$, a semi-implicitation of the expression has been selected. Once discretised temporally, it becomes:

$$D \approx \int_\Omega \left(C_{w1}f_w(\tilde{\nu}^n) - \frac{C_{b1}}{\kappa^2}f_{t2}(\tilde{\nu}^n)\right)\frac{\tilde{\nu}^n\tilde{\nu}^{n+1}}{d^2}d\Omega \tag{4.49}$$

Finally, the first diffusion term is evaluated semi-implicitly whereas the second one is treated explicitly.

Moreover, the Spalart-Allmaras turbulence model permits to evaluate the turbulent kinetic energy k as well as the turbulent dissipation rate ε. The latter can indeed be expressed by using the turbulent viscosity and the strain rate tensor with the relations of Bradshaw [24], which read:

$$\begin{cases} k = f_{v1}^{1/3}\tilde{\nu}\dfrac{S}{\sqrt{C_\mu}} \\ \varepsilon = f_{v1}^{1/2}\dfrac{(\sqrt{C_\mu}k)^2}{\tilde{\nu}+\nu} \end{cases} \tag{4.50}$$

where $C_\mu = 0.09$ is a constant involved in the $k-\varepsilon$ turbulence model and $S = \sqrt{2S_{ij}S_{ij}}$ is the strain rate tensor norm.

90° bend channel: comparison of RANS closures

To validate this model, results are compared with experimental data from [21] and numerical results from [29], as well as results obtained with the TELEMAC-3D $k-\omega$ model and the $k-\varepsilon$ model using TELEMAC-2D (because the TELEMAC-3D $k-\varepsilon$ model crashed). The flow setup describes a channel with two rectilinear sections joined by a 90° bend, for which the dimensions are shown in the Figure 4.25. The discharge is $Q = 2.95 \times 10^{-3}\text{m}^3\text{s}^{-1}$ (corresponding to a bulk velocity of $U = 1.96 \times 10^{-2}\text{ms}^{-1}$) and the mean water depth is $h = 0.175\text{m}$. The Reynolds number is $Re = 35000$ and the Froude number is $Fr = 0.15$. The inlet is in a first part of the channel of width 0.86m. After the bend, the width is $L = 0.72\text{m}$. The 2D computation domain has been discretised with 6845 unstructured elements (with grid spacings of about 4cm), and is extruded over 10 layers on the vertical for using it in 3D. Slip boundary conditions are used at lateral boundaries and a wall model (based on a Chézy law with the coefficient $C = 75$) is defined at the bottom.

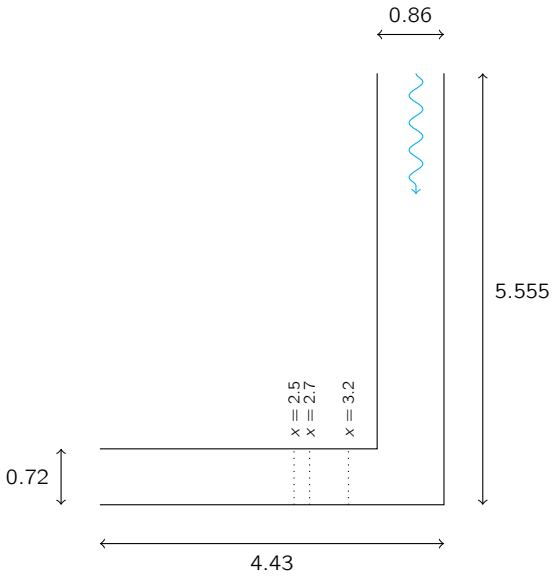

Figure 4.25: Geometry and discretisation of the domain in the (x,y) plane.

The following figures present the comparison of results obtained with the Spalart-Allmaras model (in red), the $k-\omega$ model from TELEMAC-3D, the $k-\varepsilon$ model from [29] (since the $k-\varepsilon$ model of TELEMAC-3D unfortunately crashed for these simulations) and the experiments from [21].

Figure 4.26 also shows the comparison of the depth averaged streamwise velocity profiles at three locations $x = 2.5$m, $x = 2.7$m and $x = 3.2$m. The experimental data and the $k-\varepsilon$ results being the references, the Spalart-Allmaras turbulence model gives very good results, whereas the $k-\omega$ model from TELEMAC-3D leads to a slight underestimation at the first two positions.

Figure 4.27 presents the depth averaged turbulent kinetic energy profiles. Here the experiments and the $k-\varepsilon$ results give very different results at the location $x = 3.2$m, since the numerical model estimates a twice higher turbulent kinetic energy peak. Concerning the turbulence models from TELEMAC-3D, the $k-\omega$ model evaluates energy peaks at both sides of the channel, whereas this peak is present at only one side for the other three methods. Globally, the Spalart-Allmaras model gives the best results compared to experiments, since the corresponding energy is just slightly underestimated in the recirculation area (located in the higher values of y).

Application to the flow over dunes

The flow over dunes presented in Section 4.3 is here again investigated, but with a RANS method. The Spalart-Allmaras model is compared to the $k-\varepsilon$ model available in TELEMAC-3D. The dune morphology has been discretised with a 4cm resolution grid and extruded over 15 sigma layers in the vertical axis. At the inlet, the vertical profile of averaged streamwise velocity from the experiments of [145] is prescribed. At the bottom, a wall model based on the Nikuradse friction law is defined with the roughness $k_s = 1.6$mm. The numerical schemes rely on the second order Adams-Bashforth time integration scheme for the convection and Crank-Nicholson for the diffusion terms. The physical calculation time is 500s, discretised with 0.025s time steps, leading to a CFL (based on the bulk velocity) of about 0.2. In order to investigate the influence of convection scheme, results obtained with the $k-\varepsilon$ model and the characteristic method are also compared. As in Section 4.3, flow statistics are compared along six vertical profiles, defined by the locations $x = 6$cm, $x = 13$cm, $x = 21$cm, $x = 43$cm, $x = 70$cm and $x = 127$cm.

First of all, the computational durations of the two turbulence models can be compared. Using 4 CPUs, the Spalart-Allmaras calculation time is 649s whereas the

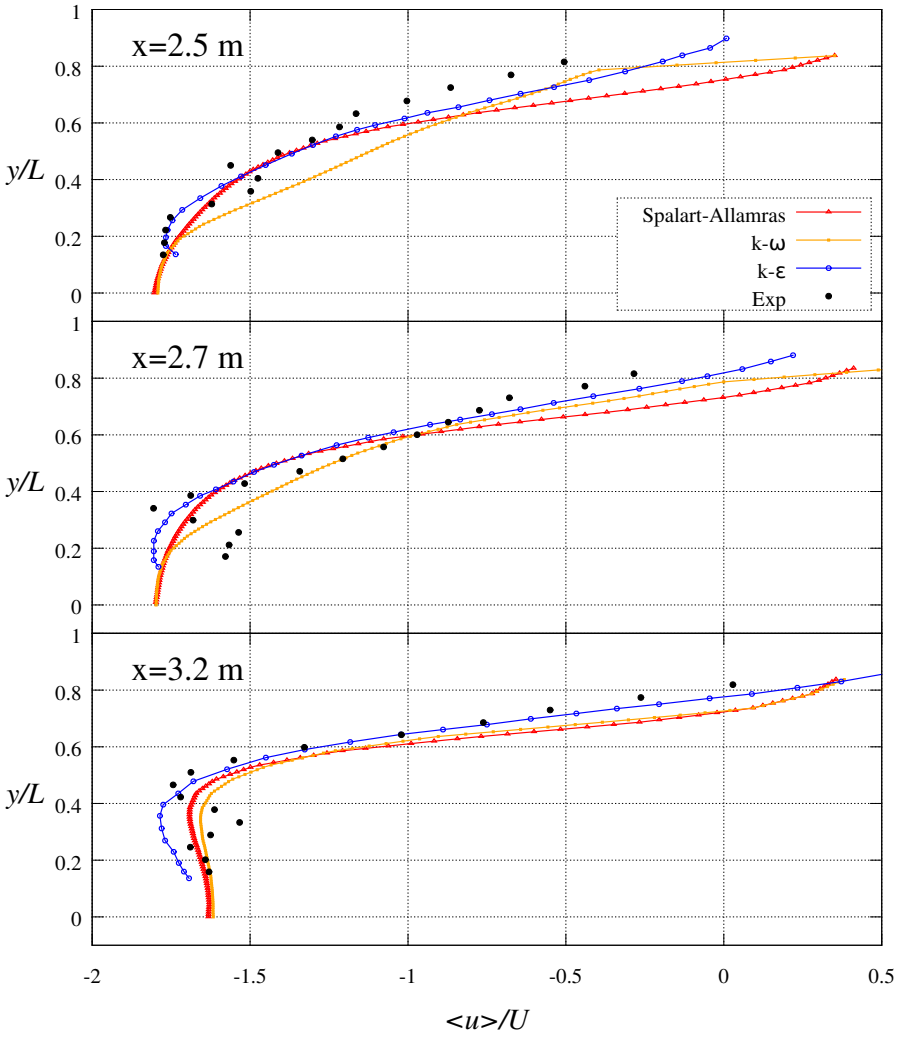

Figure 4.26: Comparison of the streamwise velocity profiles (on the left) obtained with the different methods [29, 21].

one of the $k-\varepsilon$ model is 807s. The Spalart-Allmaras model leads thus to an about 20% faster calculation.

Figure 4.28 shows the comparison of averaged streamwise velocity profiles obtained with the two turbulence models and experiments [145]. The agreement with exper-

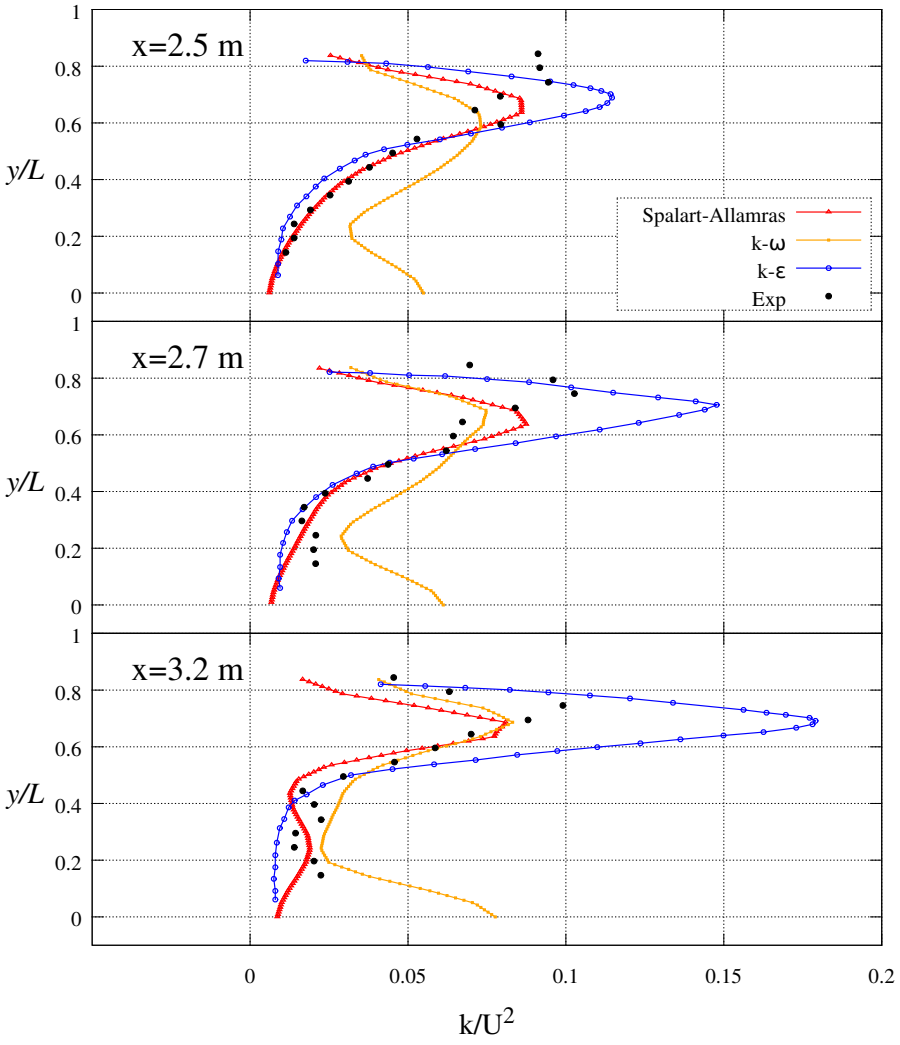

Figure 4.27: Comparison of the turbulent kinetic energy profiles obtained with the different methods [29, 21].

imental data is overall very good for both models, except in the case that uses the characteristic method, which highly overestimates the boundary layer thickness.
The turbulent kinetic energy profiles at the six locations are displayed in Figure 4.29. The Spalart-Allmaras model leads to a better amount of energy at the locations L_1,

L_2 and L_3 (which correspond to the foot of the dune), but dissipates a little more at the other locations. Here again the use of the characteristic method does not give satisfactory results at all.

In brief, the Spalart-Allmaras model gives equivalent or even better results than the $k-\varepsilon$ model with a lower computational time. Moreover, this test case highlights the need of non-dissipative schemes to simulate turbulent flows, even using RANS methods. Another advantage of the Spalart-Allmaras model is that it is easily extensible to a Detached-Eddy-Simulation (DES) method, which is a hybrid method between RANS and LES approaches, introduced in [134]. The modification consists simply of redefining the length scale of the model d in order to take into account the mesh resolution.

4.5 Turbulence modelling strategy

4.5.1 Very Large-Eddy-Simulations

Using LES methods requires fine spatial discretisation, particularly in the case of high Reynolds number flows. Achieving the grid spacings recommended in [112] ($\Delta^+ = 100-600$, $\Delta y^+ = 100-300$, $\Delta z^+ = 50-150$) is not affordable for tidal flows where the Reynolds number is about $Re = 10^8$. It would require a discretisation of a several kilometers wide domain with a grid resolution in the order of magnitude of millimeter. The computational resources being unavailable to achieve this, the resulting spatial discretisation is going to be too coarse. The LES cutoff is also located below the wavenumber range of the most energetic modes and it is not sufficient to simulate the desired quantity of turbulent kinetic energy. VLES is thus fairly counterclaimed and not recommended in the literature [52], but it remains possible to capture the large-scale unsteadiness of flows [53].

Nevertheless, minimal dissipation models have been introduced very recently in [147, 124, 6] for the achievement of Very Large-Eddy-Simulations (VLES) [52], while keeping satisfying turbulence statistics. Such models have indeed been used successfully in [7] and [130] to simulate real scale atmospheric boundary layers, for which both the obtained averaged velocity and turbulent statistics fit with reference.

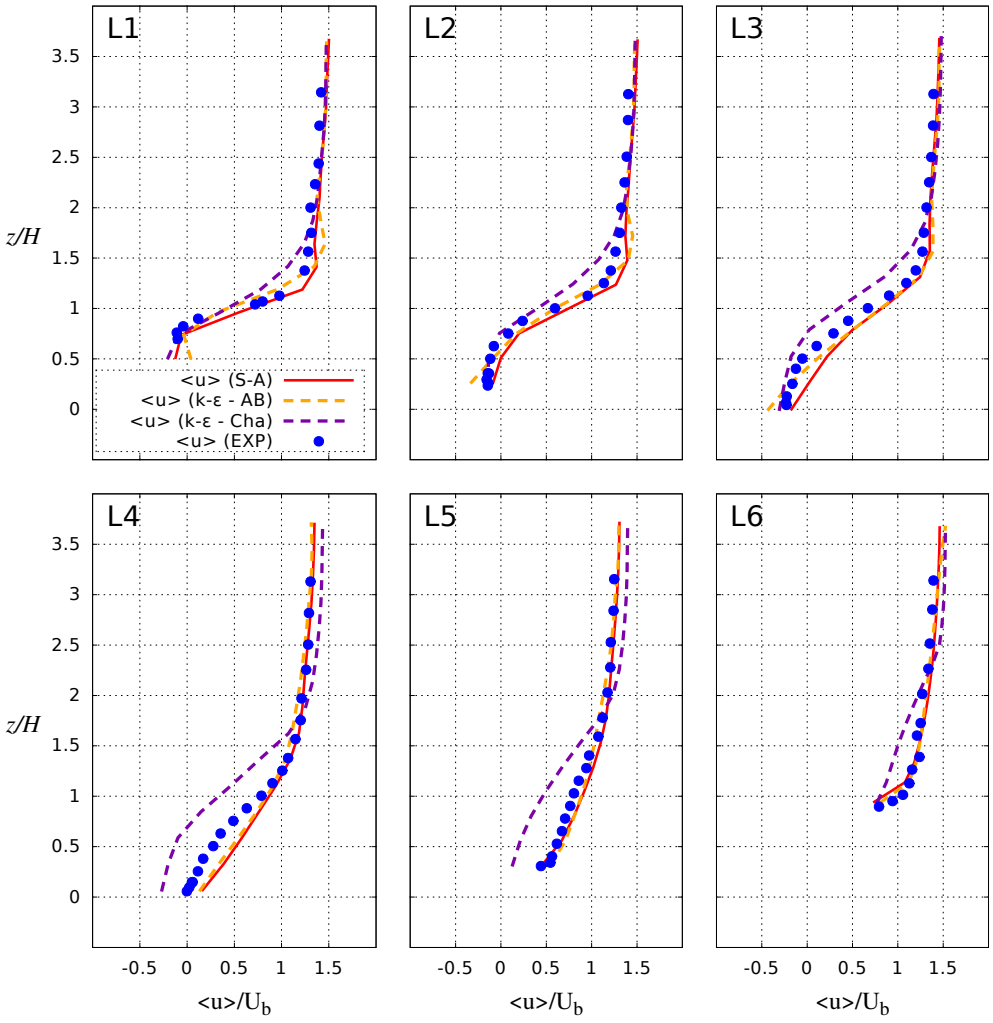

Figure 4.28: Comparison of the averaged streamwise velocity profiles obtained with Spalart-Allmaras (S-A), $k-\varepsilon$ with the characterstics method ($k-\varepsilon$ - Cha) and the Adams-Bashforth centered finite element formulation ($k-\varepsilon$ - AB) and experiments (EXP)[145].

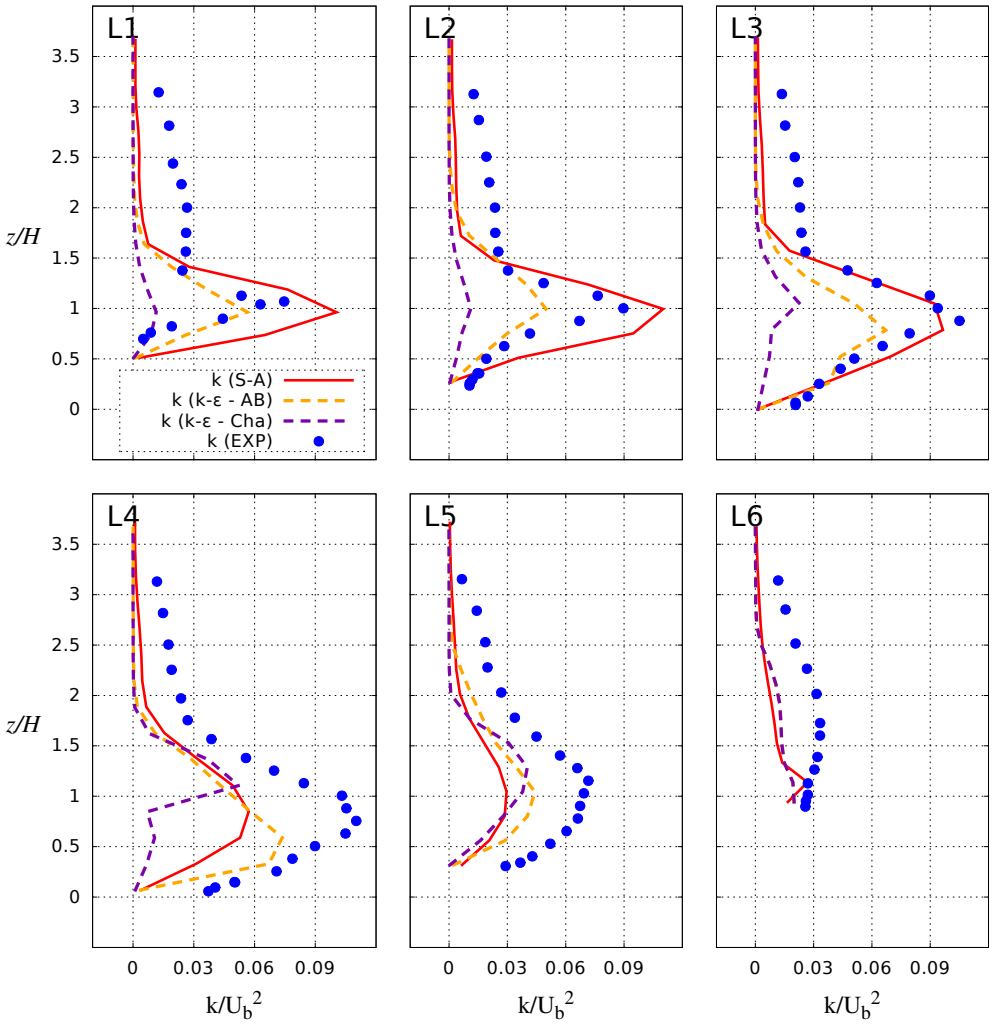

Figure 4.29: Comparison of the turbulent kinetic energy profiles (on the right) obtained with Spalart-Allmaras (S-A), $k-\varepsilon$ with the characterstics method ($k-\varepsilon$ - Cha) and the Adams-Bashforth centered finite element formulation ($k-\varepsilon$ - AB) and experiments (EXP)[145].

In the framework of tidal turbulence modelling using LES, the use of VLES methods is certainly not enticing, but it seems to remain the only way in the waiting for more powerful calculation resources.

4.5.2 Prospective application

Before using these methods to simulate real tidal flow, a channel flow with the same characteristics is investigated in order to evaluate the targeted grid spacings to simulate flows, as well as the recommended subgrid model. Therefore, a computational domain of length 5km and width 1km, with a maximum water depth of $H = 40$m and a bulk velocity of $U_b = 3\text{ms}^{-1}$ has been defined, with a bottom composed of dunes with the same shape as the case described previously in Section 4.3. These dunes are located all along the channel and have a length of $L_d = 100$m and a height of $h_d = 5$m. This flow setup has been discretised with two meshes, with horizontal grid spacings of 5m and 10m respectively, and extruded with 20 and 30 horizontal planes. Considering the Reynolds number (which is $Re \approx 10^8$ based on the bulk velocity and the water depth), the recommended grid spacings in [112] are obviously not verified. As boundary conditions, the Synthetic-Eddy-Method is used at the inlet, and a wall model based on the Nikuradse law ($k_s = 0.1$m) is prescribed at the bottom. In terms of subgrid models, both the Smagorinsky model and the AMD model are used and compared.

The results obtained with the four numerical setups (two subgrid models and two grid resolutions) are compared with the experimental data from [145]. Despite the fact that these data are obtained from a lower Reynolds number flow (see section 4.3), the dimensionless flow statistics are assumed to remain similar. These statistics (averaged velocities and Reynolds stresses) are compared along four vertical profiles along the dunes, located respectively at the abscissa denoted $L_1 = 3.75$m, $L_3 = 13.125$m, $L_4 = 26.875$m and $L_6 = 79.375$m in the dune profile (by analogy with the notation used in Section 4.3). Figure 4.30 presents respectively the averaged streamwise velocity profiles and the vertical velocity profiles obtained with the different numerical models.

Each setting gives correct results regarding the streamwise velocity. Nevertheless, the vertical velocity profiles show great discrepancies between results obtained with the Smagorinsky model and those obtained with the AMD model. The results of the

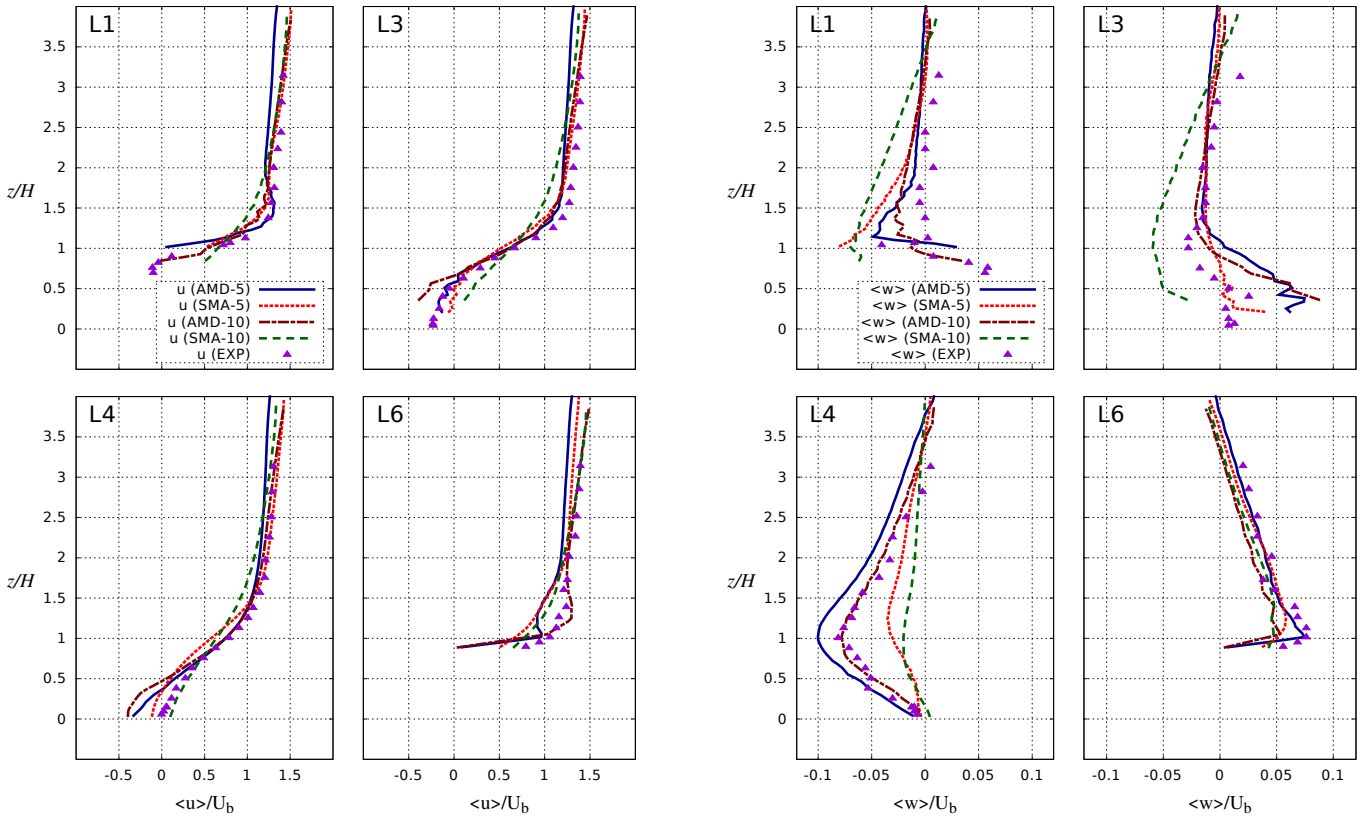

Figure 4.30: Averaged streamwise and vertical velocity profiles obtained with the 5m and 10 grid resolution and two subgrid models (AMD model and SMA for Smagorinsky model), compared with experimental results from [145].

AMD model are similar and remain consistent with the experimental data. However, the Smagorinsky model does not succeed to reproduce the right profile shape, particularly at the location $L3$ where the two discretisations give very different results. Figure 4.31 shows the comparison of turbulent kinetic energy vertical profiles as well as the profiles of the shear Reynolds stress.

Here again, each subgrid model gives very different results. Only the AMD model is able to reproduce a sufficient amount of turbulent kinetic energy at the locations $L1$, $L3$ and $L4$, which is nevertheless overestimated at the position $L6$. Regarding the shear Reynold stress, the same conclusion can be established, with the addition

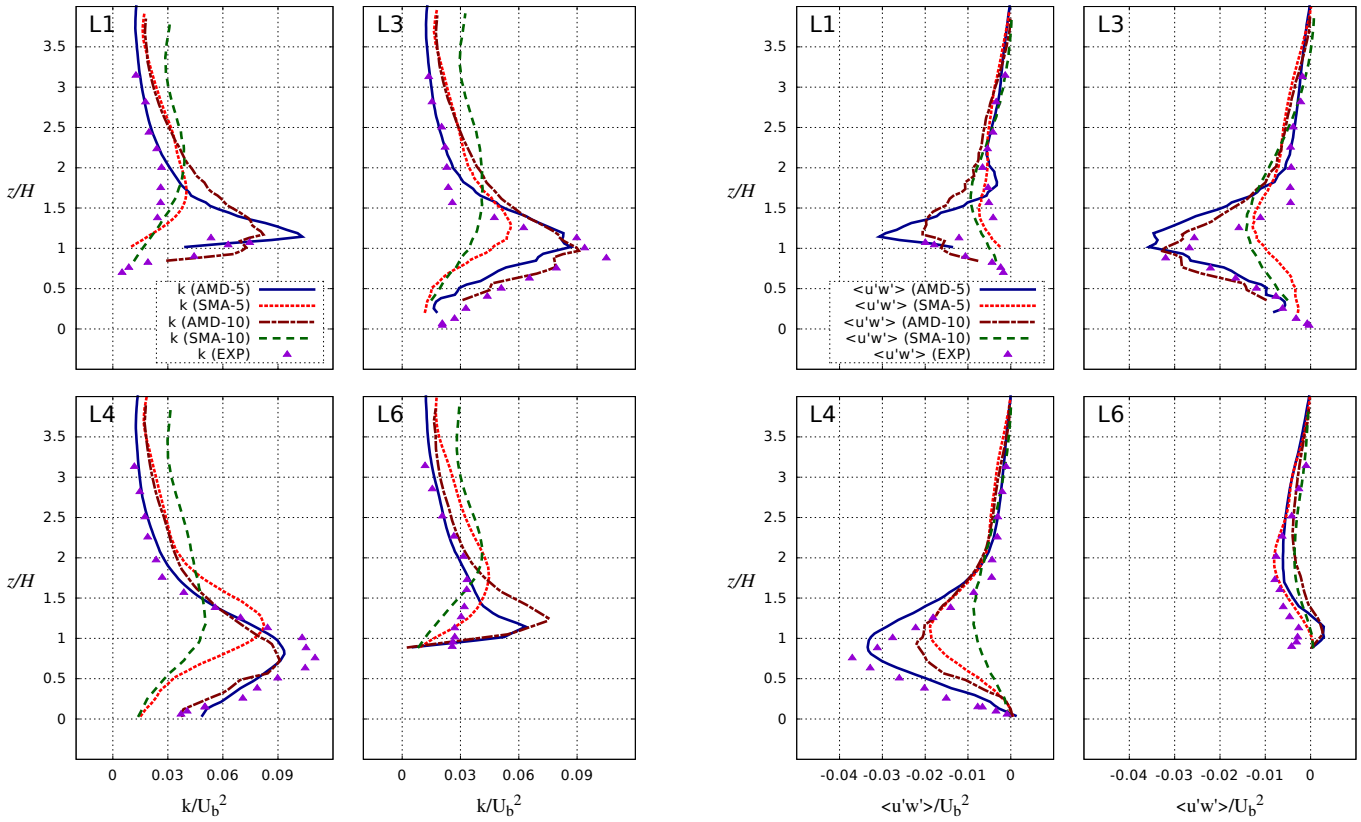

Figure 4.31: Turbulent kinetic energy and Shear Reynolds stress profiles obtained with the 5m and 10 grid resolution and two subgrid models (AMD model and SMA for Smagorinsky model), compared with experimental results from [145].

of an underestimation of the coarser simulation using the AMD model.

This prospective application enables an a priori assessment of using a LES approach to simulate tidal flows.

4.6 Synthesis

A LES approach has been successfully implemented in the environmental software TELEMAC-3D. In addition to the subgrid models, specific boundary conditions have been implemented, such as the Synthetic Eddy Method (SEM) which is used at the

inlet boundary to generate the first velocity fluctuations. Particular attention was given to reduce the numerical dissipation of advection scheme and time discretisation of TELEMAC-3D by introducing a non-dissipative and second order convection scheme. Several numerical assumptions have finally been removed, such as mass-lumping. These developments enable the obtainment of encouraging results. The behaviour of the turbulence indicators is overall very satisfactory, since both the averaged velocity and the Reynolds stresses fit with the experimental measurements results. Moreover, LES simulations permit the identification of main turbulent structures using Q and λ_2 criteria, given additional information about the unsteady behaviour of turbulent flows.

Physical processes simulated by TELEMAC users can be enriched by taking into account flow fluctuations. For instance, LES can considerably improve the study of thermal plume, suspended sediment transport, submarine turbine design or offshore wind farm, which have strong dependencies on the unsteady motion and dissipative effects. New physical processes can also be studied, such as the interaction between vortices and free surface. As illustration, the simulation of a half ring vortex propagating at the free surface is proposed in Figure 4.32. This figure displays a snapshot of such a vortex, initially U-shaped and distorting with turbulent effects.

In the framework of the tidal turbulence modelling objective, the model has finally been extended to enable the simulation of regional scale flows and to model tidal flows turbulence. Due to the high Reynolds number of environmental flows and the considerable cost of Large-Eddy-Simulation, an embedded LES method has been introduced. A such turbulent modelling relies consists of defining a subgrid model only in a small part of the computational domain, whereas a RANS model is used elsewhere. The two chosen turbulence models are respectively the Anistropic Minimum Dissipation model (AMD), which has shown a good behaviour by performing VLESs, and the Spalart-Allmaras model, which has been evaluated faster than the $k-\varepsilon$ model and giving such satisfactory results.

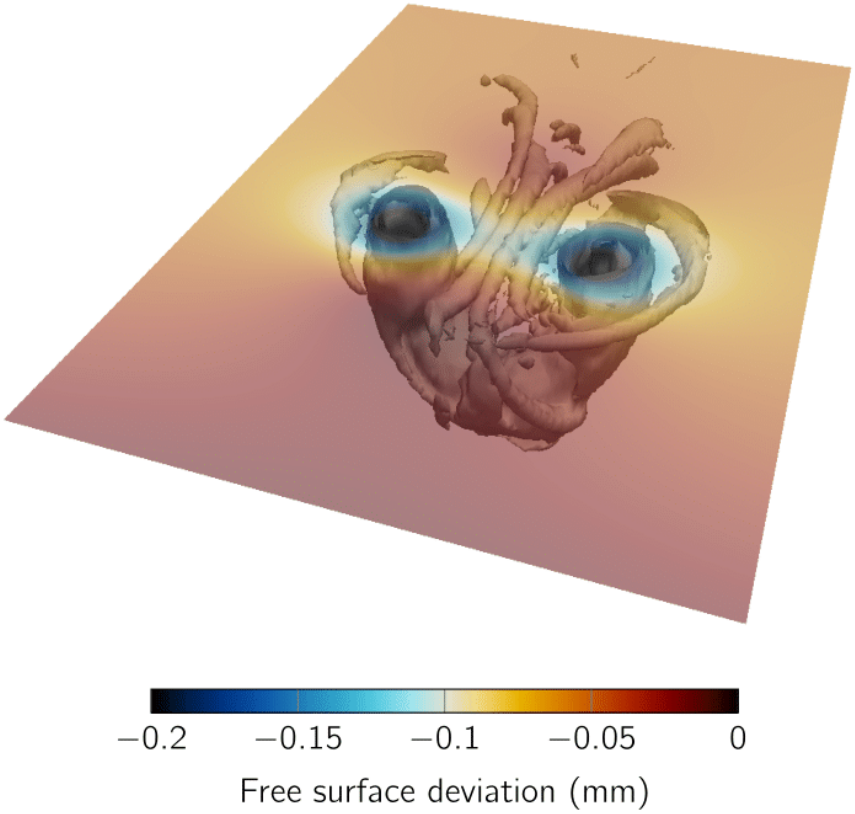

Figure 4.32: Snapshot of a half ring vortex propagating near the free surface.

Chapter 5

Simulations of flow in the Alderney Race

The difference between theory and practice is in theory somewhat smaller than in practice.

Anonymous

Ce chapitre concerne l'application de la démarche décrite au chapitre précédent au Raz Blanchard. Sa construction y est décrite. Le domaine de calcul s'appuie sur une emprise de l'ordre de 100 *km, et deux configurations de marée ont été simulées (coefficients de 28 et 104). Les résultats obtenus avec un modèle RANS, LES imbriquée et mesures ADCP sont alors comparées. Une analyse spatiale des structures cohérentes est enfin réalisée.*

This chapter is about the previously described methodology application to the Alderney Race flow. The computational domain is about 100 km wide, and two tidal phases have been simulated (coefficients of 28 and 104). Then, results obtained with a RANS model, the embedded LES methodology and ADCP measurements are compared. Finally, a spatial analysis of the coherent structures is carried out.

5.1 Alderney Race model

5.1.1 ADCP measurements

The simulations of the Alderney Race site are performed at two dates, which correspond to ADCP measurements times realized in the THYMOTE project framework [5]. These dates correspond to extreme events. First, the 29/09/2017 was characterized by a low tide period with a tide coefficient of 28. Second, the 07/10/2017 corresponded to a period of high tide with a coefficient of 104. These dates correspond actually to the ADCP measurements campaign performed by iXblue and

France Energies Marines in the framework of the project THYMOTE. The measurement station is composed of two ADCPs (Teledyne RDI Workhorse Sentinel 600 kHz). Its theoretical and actual installation locations are given in Table 5.1. This position as well as the device are illustrated in Figure 5.1.

	GPS coordinates ($WGS84$)				
Station	Theoretical		Actual		Depth
	Latitude	Longitude	Latitude	Longitude	
ADCP cage	$49°42,801'$ N	$2°0,193'$W	$49°42,8026'$ N	$2°0,1929'$W	$27-29$m

Table 5.1: Theoretical and actual installation locations of the ADCP measurements station [5].

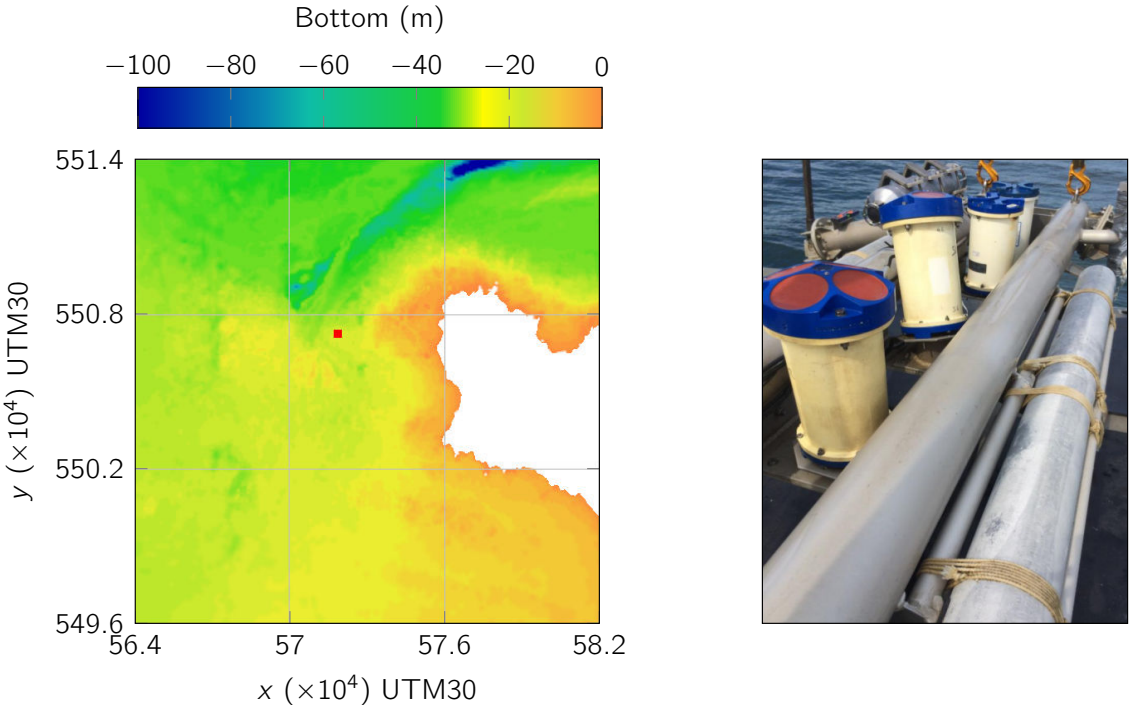

Figure 5.1: Location and image of the ADCP device.

The acquisition mode of the two ADCPs is programmed in "master/slave". An optimal way to measure the flow quantities over a large part of the water column is obtained when the ADCP "Slave" is positioned with a course and pitch shift of $+45°$

and $+20^\circ$ with respect to the ADCP "master". In this configuration, beam 3 of the ADCP slave is vertical and perpendicular to the surface. A sketch of the device is presented in Figure 5.2. The ADCP cell was deployed almost transverse to the axis of the tidal current on site, which defines (u_n, u_t) as the velocity component in the tidal current axis and the velocity component in the transverse axis, as illustrated in Figure 5.2.

The Reynolds stresses have been estimated using two methods:

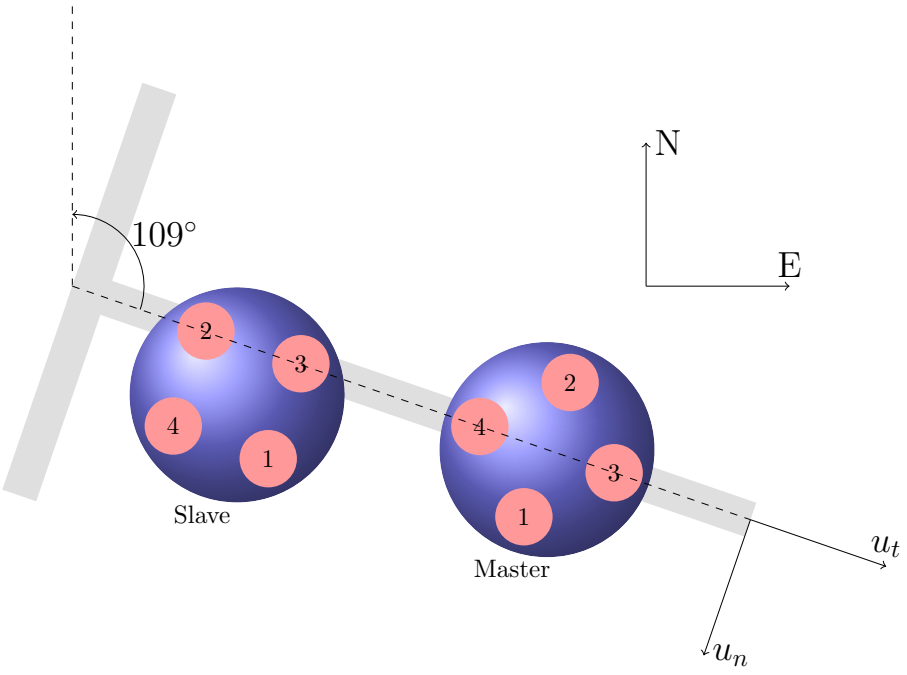

Figure 5.2: Sketch of ADCP cells positioning.

- The 5 beam ADCP method [43] enables the evaluation of five out of six Reynolds stresses, which are $\overline{u'w'}$, $\overline{v'w'}$ and the three diagonal stresses $\overline{u'^2}$, $\overline{v'^2}$ and $\overline{w'^2}$.
- The 8 beam ADCP method permits the evaluation of the six components of the Reynolds tensor [146]. This method involves the use of two 4-beam ADCPs, i.e. 8 radial velocity components, which allows an overdetermined system of equations.

Both methods give similar results, but the 8-beam method tends to overestimate tensors $\overline{v'w'}$ and $\overline{w'^2}$ as well as the anisotropy ratio, whereas the other turbulent

parameters ($\overline{u'w'}$, $\overline{u'^2}$, $\overline{v'^2}$, and the turbulent kinetic energy) are underestimated. The 5-beam method does not permit the calculation of the stress $\overline{u'v'}$ but it is debatable to suggest that it more accurately estimates Reynolds tensors.

5.1.2 Spatial and temporal discretisation

The Alderney Race numerical model is based on an about 150×120 km computational domain, focused on the allowed zone for the installation of the pilot farms (shown in Figure 1.9). The bathymetry of the domain is interpolated from a 1m resolution database, and completed with a 100m resolution grid. The area's location is reminded in Figure 5.3. Regarding the asperities on the bottom, the roughness sizes have

Figure 5.3: Location of the Alderney Race site (Raz Blanchard in French).

been evaluated on the basis of the English Channel sediment map from [1]. Figure 5.4 shows respectively the morphology and the roughness sizes interpolated for the numerical models.

Two computational domains have been used. A first one, used for RANS simulations by using the Spalart-Allmaras model only, relies on a grid resolution of 400m and extruded over the vertical with 20 σ-layers. For simulations using the embedded LES method, a resolution of 400m near the liquid boundaries is defined, as well as an internal domain composed of four areas for which the point density rises by approaching the LES subdomain. Figure 5.5 shows the different density areas involved in the LES grid. The grid has a resolution of 5m in the LES subdomain and is extruded

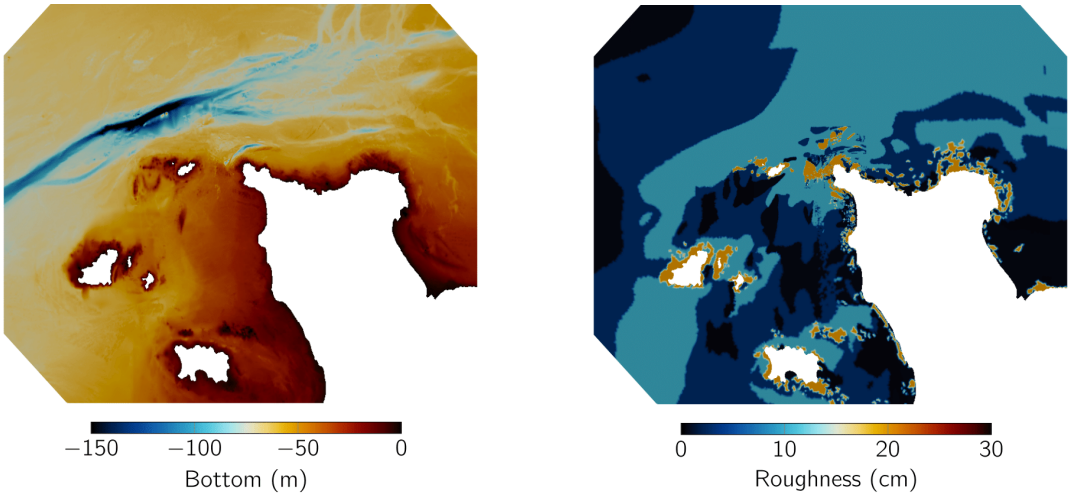

Figure 5.4: Bathymetry and roughness of the Alderney Race numerical model.

over 20 σ layers. The second finer density square, coloured in purple in Figure 5.5 for which the grid spacings are about 50m, corresponds to the area for which the bathymetry is interpolated from a high resolution database. The two other polygons have been defined in order to alleviate abrupt variations of cell sizes, which could degrade the numerical accuracy of simulations. Table 5.2 summarizes the several meshes characteristics.

	2D points (-)	vertical layers (-)	Min density (m)	Max density (m)
RANS	95313	20	400	400
LES	581432	20	400	5

Table 5.2: Mesh characteristics for the Alderney Race models.

Regarding the time discretisation, time steps of respectively 0.5s and 0.2s have been used for the RANS and LES computations.

5.1.3 Boundary conditions

To impose the tidal conditions, the TPXO tidal database is used on the liquid boundaries. This database enables the interpolation of the water depth and the depth averaged horizontal velocity components at the boundary nodes (see section 3.3.3). In the following simulations, only the horizontal velocity components are prescribed

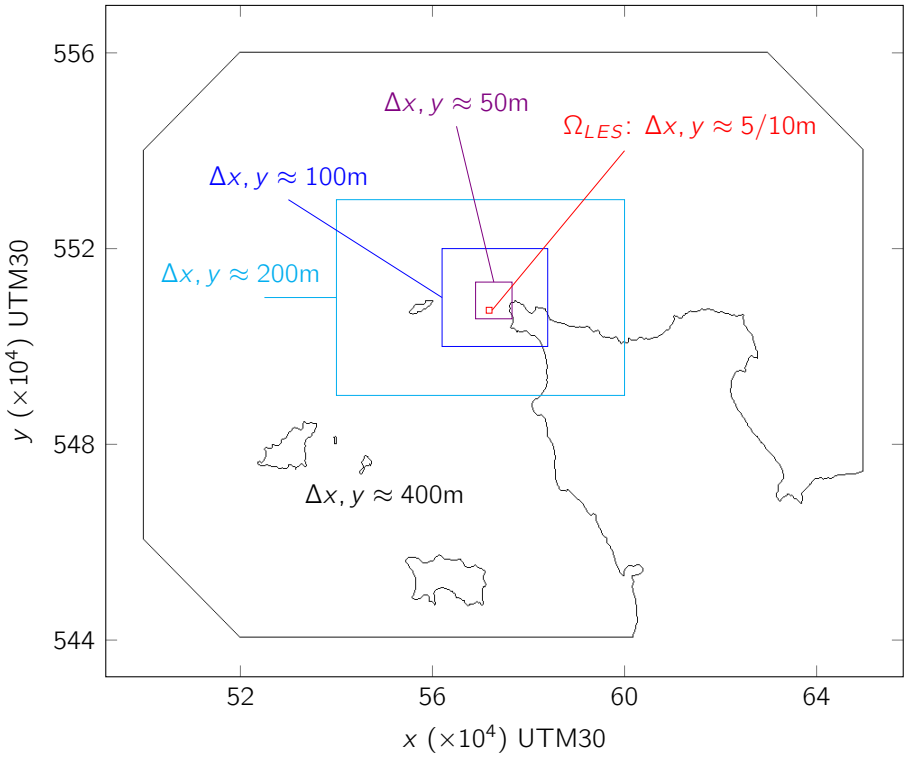

Figure 5.5: Point density in the LES Alderney Race 2D meshes.

with Dirichlet boundary conditions, whereas the vertical velocity and the water depth are free. To obtain more realistic vertical velocity profiles, the horizontal velocity components are multiplied by a function depending on altitude, which enables the definition of a logarithmic-like profile. However, these boundary conditions prescriptions can be somewhat abrupt for the calculations, particularly with the use of high order centered numerical schemes (see section 4.1.4), which are required for LES. A stabilisation term is thus added at the liquid boundary points in the convection-diffusion step, based on the SUPG formulation [110].

The coasts are treated as solid walls with a roughness coefficient of $k_s = 0.5$m. A wall model is furthermore applied at the bottom of the computational domain, for which a roughness map is presented in Figure 5.4.

5.1.4 Flow statistics computation

A final element has to be taken into account before running the calculations. Contrary to the flows covered in Chapter 4, the presence of tides makes the calculations of the statistical quantities less obvious. It is indeed required to distinguish the turbulent fluctuations from the tide variations, so the averages have to be computed over a sufficiently short duration (ten minutes in [5]), in order not to be influenced by the tide scale. An average per block operator has therefore been introduced. Time is divided into periods denoted $t_a = 6$min. At each period, a new average begins. Then, when the present time comes in the next period, the operative mean will be the one started previously. In enables also the computation of a quantity averaged over a duration of between 6 to 12min. The calculation of the Reynolds stresses relies on the same principle.

Finally, the computed Reynolds stresses are rotated by $\theta = 109°$ (see Figure 5.2) in order to be compared with the measured values. The six obtained quantities read as follows:

$$\begin{cases} < u_n' u_n' > = < u'u' > \cos^2(\theta) + < v'v' > \sin^2(\theta) - 2 < u'v' > \cos(\theta)\sin(\theta) \\ < u_n' u_t' > = (< u'u' > - < v'v' >)\cos(\theta)\sin(\theta) + < u'v' > (\cos^2(\theta) - \sin^2(\theta)) \\ < u_n' w' > = < u'w' > \cos(\theta) + < v'w' > \sin(\theta) \\ < u_t' u_t' > = < u'u' > \sin^2(\theta) + < v'v' > \cos^2(\theta) + 2 < u'v' > \cos(\theta)\sin(\theta) \\ < u_t' w' > = < u'w' > \sin(\theta) + < v'w' > \cos(\theta) \\ < w'w' > = < w'w' > \end{cases} \tag{5.1}$$

5.2 Results

In this section, results obtained with RANS and LES simulations are compared to ADCP measurements over a vertical profile at the location presented in Table 5.1 [5]. Both the averaged flow and turbulent quantities are investigated. Figure 5.6 presents the evolution of vertical profile of the averaged velocity magnitude and the water depth during the low tide and the high tide day, obtained with the different methods (RANS, LES, and ADCP). The RANS and LES methods give satisfactory data, with maximum velocity achieving $2\text{m}s^{-1}$ for the low tide day and up to $5\text{m}s^{-1}$

in the high tide day case. Furthermore, all methods presented herein enable the good depiction of the $M4$ tidal wave influence on the 07/10/17, which induces a higher velocity magnitude during the flood tide than during the ebb tide (whereas it is commonly the opposite considering continuity).

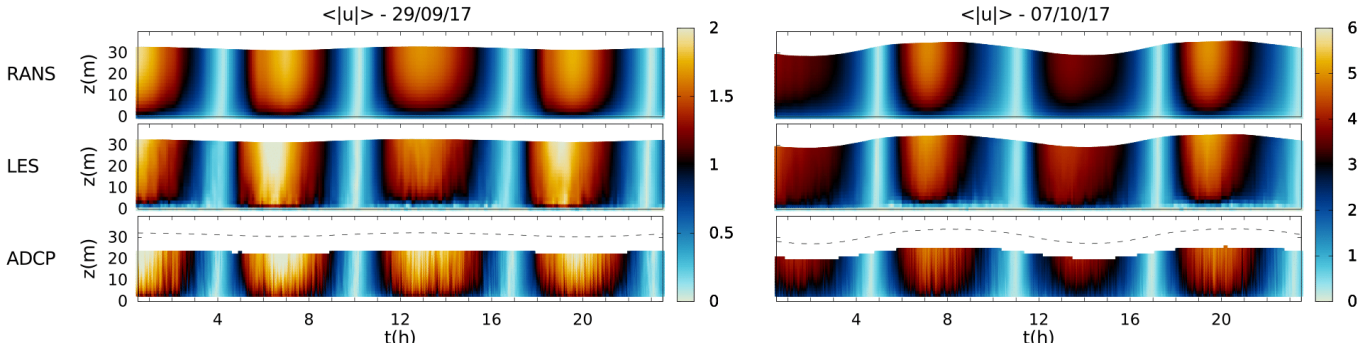

Figure 5.6: Temporal evolution of the vertical profile of averaged velocity magnitude on the 29/09/17 and the 07/10/17.

The three components of velocity $=(u,v,w)$ (in the geophysical coordinate system) are displayed respectively in Figures 5.7, 5.8 and 5.9. The agreement of the v velocity components is good for the two numerical methods, but the u and w components are underestimated, particularly in the case of results obtained with the RANS turbulence modelling.

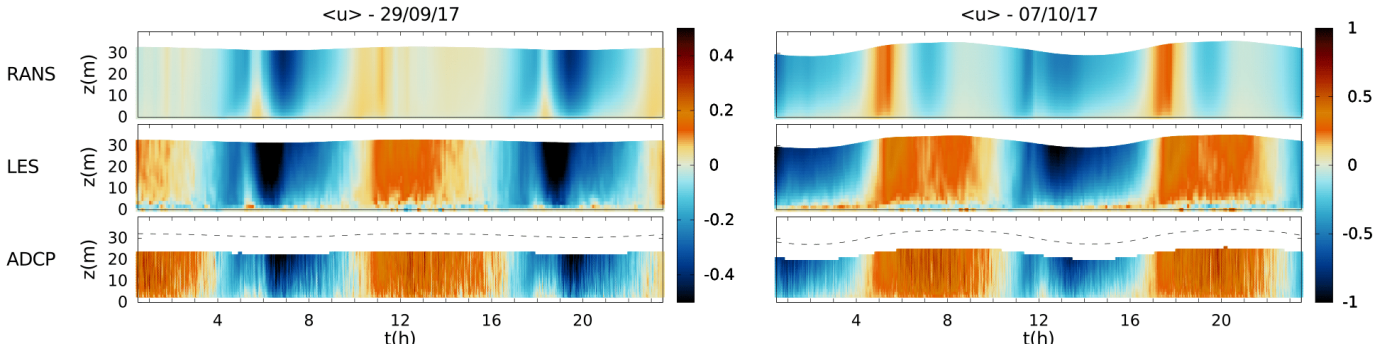

Figure 5.7: Temporal evolution of the vertical profile of averaged velocity component u (ms^{-1}) on the 29/09/17 and the 07/10/17.

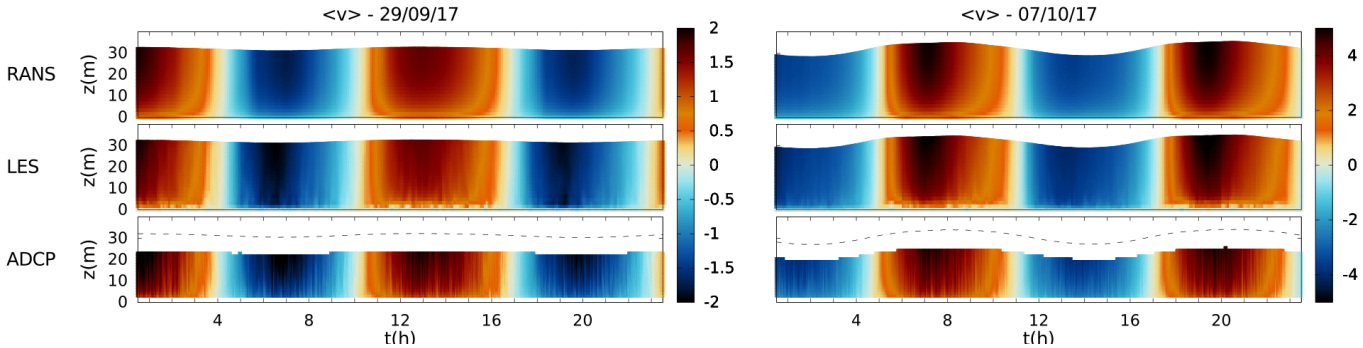

Figure 5.8: Temporal evolution of the vertical profile of averaged velocity component v (ms^{-1}) on the 29/09/17 and the 07/10/17.

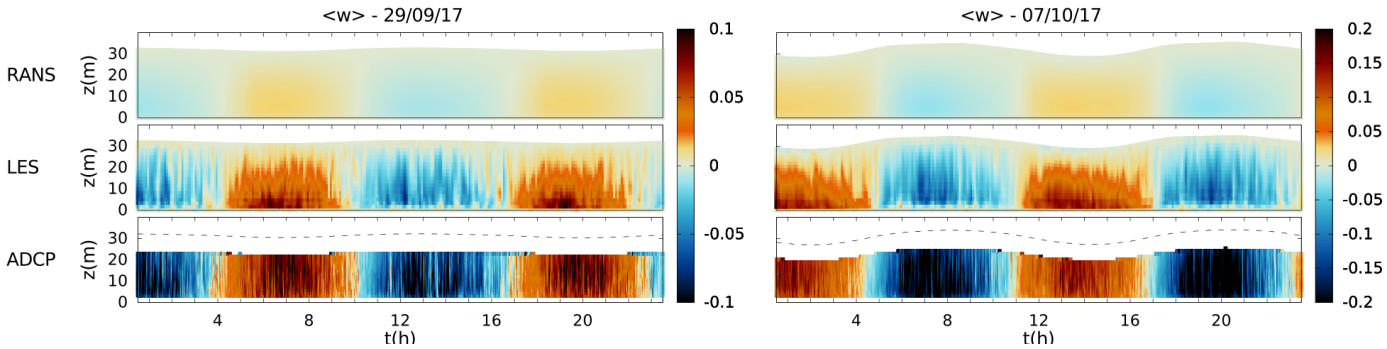

Figure 5.9: Temporal evolution of the vertical profile of averaged velocity component w (ms^{-1}) on the 29/09/17 and the 07/10/17.

Figure 5.10 presents the turbulent kinetic energy profiles obtained with the two numerical approaches (RANS, LES) as well as the two experiment processes (ADCP 5-beam and ADCP 8-beam). The trend of the numerical methods is identical. The TKE reaches a good level of energy near the bottom, but it is underestimated in the water column. The devaluation of the RANS model raises concern since the artificial turbulence generated at the embedded LES subdomain depends on it.

The comparison of the three diagonal Reynolds stresses obtained with the two LES models and the two ADCP methods are shown in Figures 5.11, 5.12 and 5.13. A similar discussion for the TKE can be made: the LES methods do not reproduce a sufficient amount of turbulent quantities in the upper region of the water column.

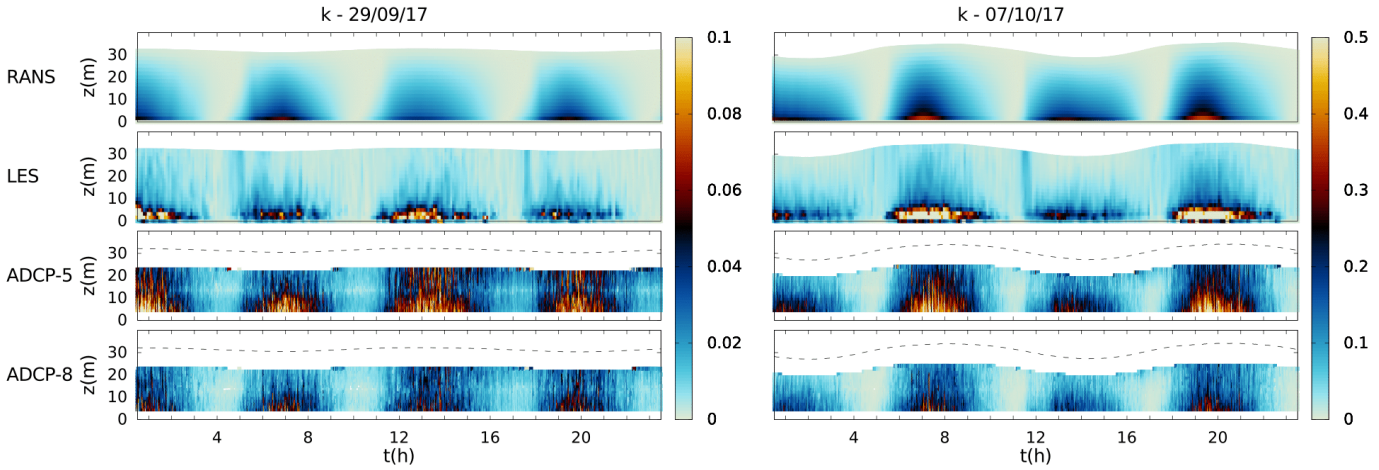

Figure 5.10: Temporal vertical profile of turbulent kinetic energy (m^2s^{-2}) on the 29/09/17 and on the 07/10/17.

Moreover, the Reynolds stresses $< u_n' u_n >$ and $< u_t' u_t' >$ are slightly overestimated near the bottom, whereas $< w'w' >$ is overall quite underestimated. Furthermore, the discrepancies between both ADCP methods are significant here.

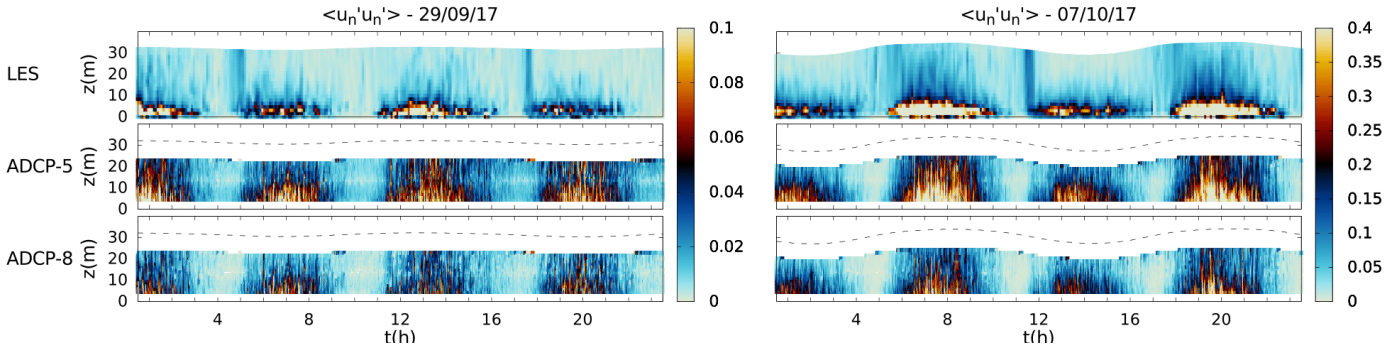

Figure 5.11: Temporal vertical profile of the Reynolds stress $< u_n' u_n' >$ (m^2s^{-2}) on the 29/09/17 and the 07/10/17.

The Reynolds stresses $< u_n' w' >$ and $< u_t' w' >$ are respectively displayed in Figures 5.14 and 5.15. The agreement of the Reynold stress $< u_n' w' >$ is good, particularly in the case performed on 07/10/17. However the results about $< u_t' w' >$ are conflicting since LES evaluates negative values during the ebb and positive values during

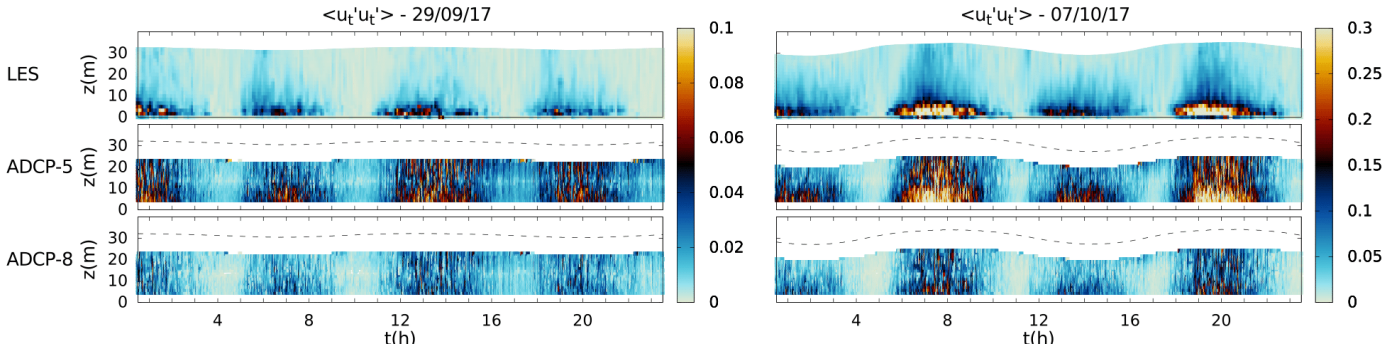

Figure 5.12: Temporal vertical profile of the Reynolds stress $< u_t' u_t' >$ ($m^2 s^{-2}$) on the 29/09/17 and the 07/10/17.

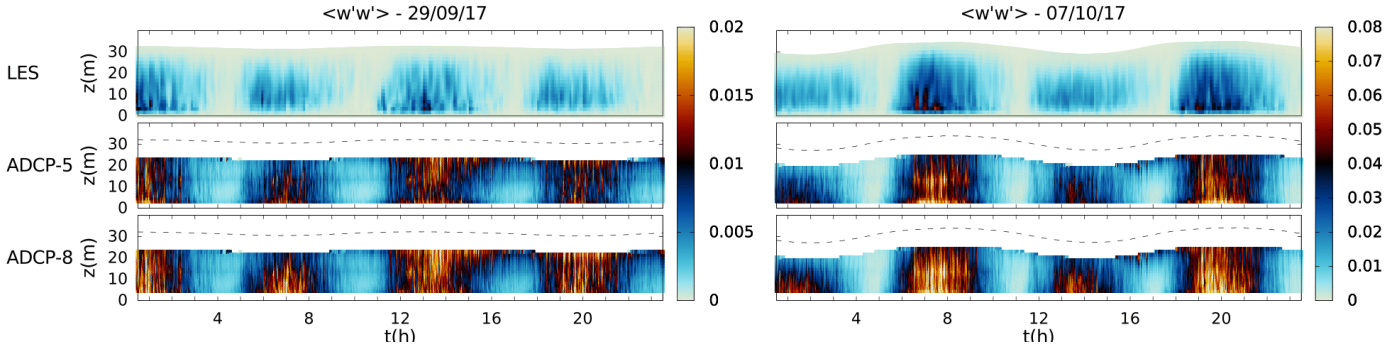

Figure 5.13: Temporal vertical profile of the Reynolds stress $< w'w' >$ ($m^2 s^{-2}$) on the 29/09/17 and the 07/10/17.

the flood, whereas $< u_t' w' >$ does not appear to have a distinctive sign according to measurements.

What can be concluded from these comparisons is first the better description of averaged velocity fields of LES models. RANS results show indeed a good agreement with in-situ measurements concerning the velocity $< v >$, whereas $< u >$ and $< w >$ are very underestimated, which is not the case for the LES data. Regarding the turbulence statistics, LES results enable overall the good depiction of the Reynolds stress tensor components since they lead to a good peak energy just above the bottom. Nevertheless, they cannot reproduce them sufficiently in the water column. This underestimation may be due to the coarse discretisation. The RANS turbulent

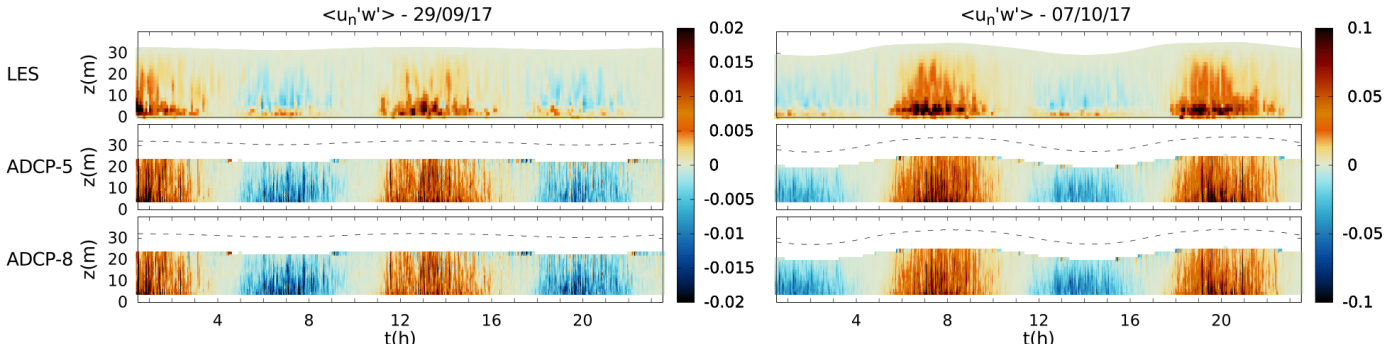

Figure 5.14: Temporal vertical profile of the Reynolds stress $< u_n' w' >$ ($m^2 s^{-2}$)on the 29/09/17 and the 07/10/17.

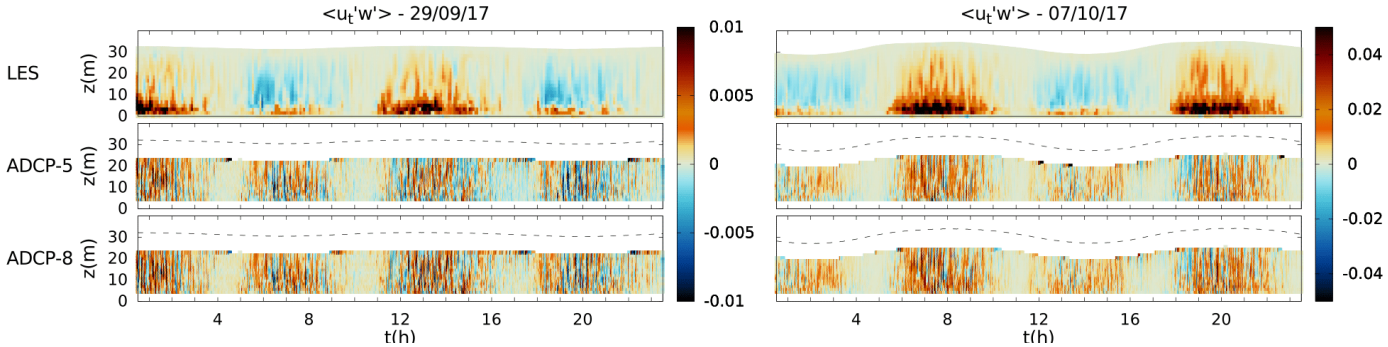

Figure 5.15: Temporal vertical profile of the Reynolds stress $< u_t' w' >$ ($m^2 s^{-2}$) on the 29/09/17 and the 07/10/17.

kinetic energy, which is undervalued too, might also have an influence, and turbulence may also not be sufficiently developed at the measurement point despite the introduced artificial fluctuations.

Two dimensional maps of the LES subdomain are presented hereafter. Firstly, Figure 5.16 presents the Alderney Race bathymetry. This topography includes mainly a shallow rocky plateau in the southern part, a rift northwest section and few dunes located on the northern side. Instantaneous flow quantities are investigated at flood (when the water level rises) and ebb (outgoing water) tides.

Figures 5.17 and 5.18 show the velocity magnitude obtained at 8m above the

seabed, on the 07/10/17 at respectively 1a.m. and 7a.m (which corresponds to ebb and flood waters). Such a velocity fields could directly impact potential tidal turbines. The highest velocity magnitude areas appear to be located over the rocky plateau, southeast of the area, where it reaches 5ms^{-1}. The influence of the Alderney Race rift can also be eyed through an important loss of velocity as well as great flow fluctuations through the flood waters. It suggests the presence of large boils in this area (with an up to 20m diameter), which is consistent with observations.

Turbulent kinetic energy maps obtained at the same moments on the plane defined at 8m above the seabed are presented in Figures 5.19 and 5.20. It reflects the significant turbulent production occurring on the rocky plateau and near the dune crests. These results also enable the identification of the rift during the ongoing phase of tide, above which the turbulent kinetic energy is particularly prominent. A quite substantial part of turbulent kinetic energy rises up in the water, but is nevertheless broadly lower during the ebb period.

Figure 5.21 and 5.22 present some λ_2 isosurfaces coloured by their elevation. These results enable the identification of coherent turbulent structures generated by the bottom morphology at both flood and ebb tides. The rocky plateau looks to be responsible for the formation of hairpin vortices, some of which reaching the water surface. Deeper eddies can also be distinguished at the seabed crests present in the north of the domain. It also reveals large turbulent structures located in the rift at flood tide.

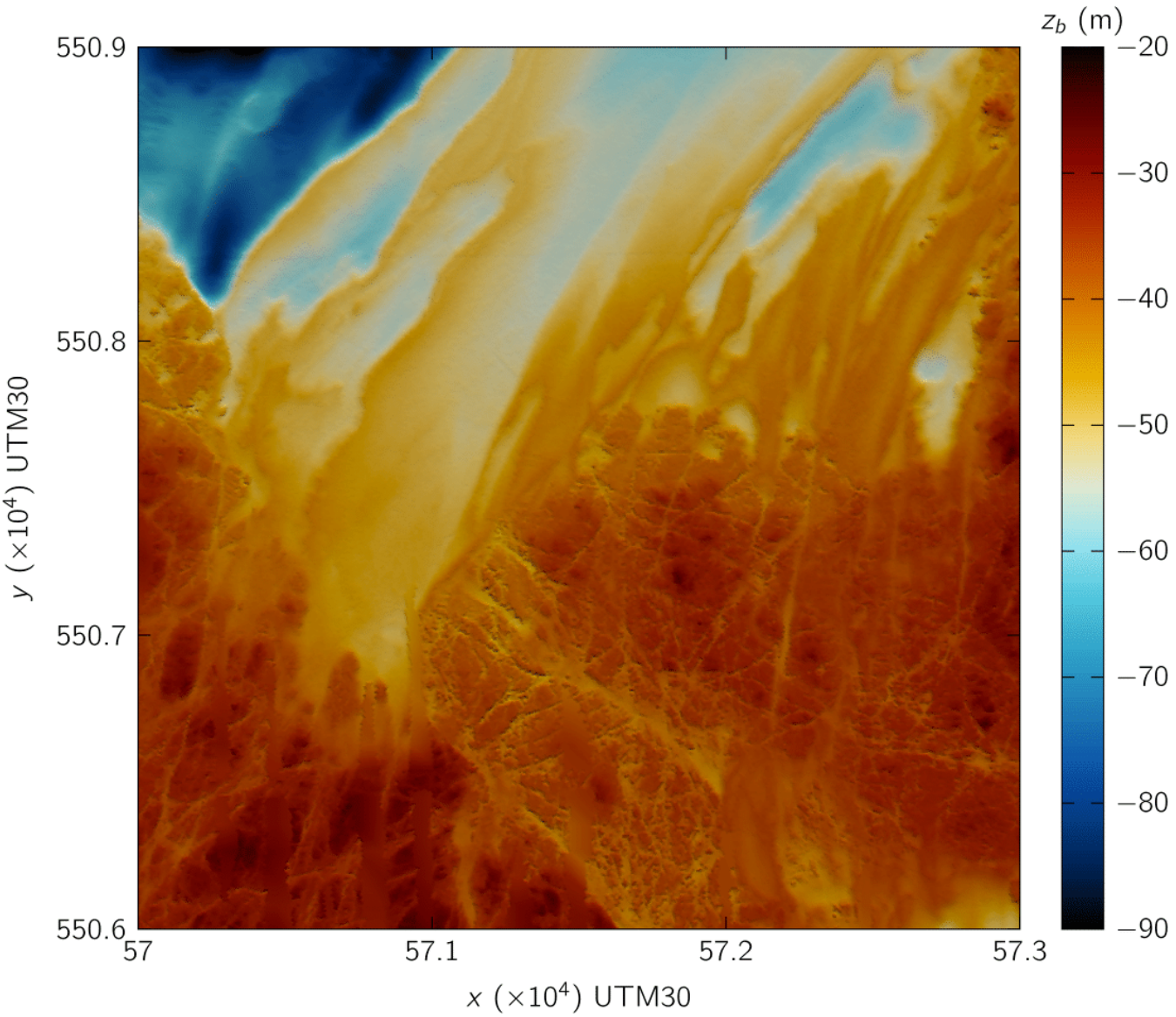

Figure 5.16: Bottom of the Alderney Race model.

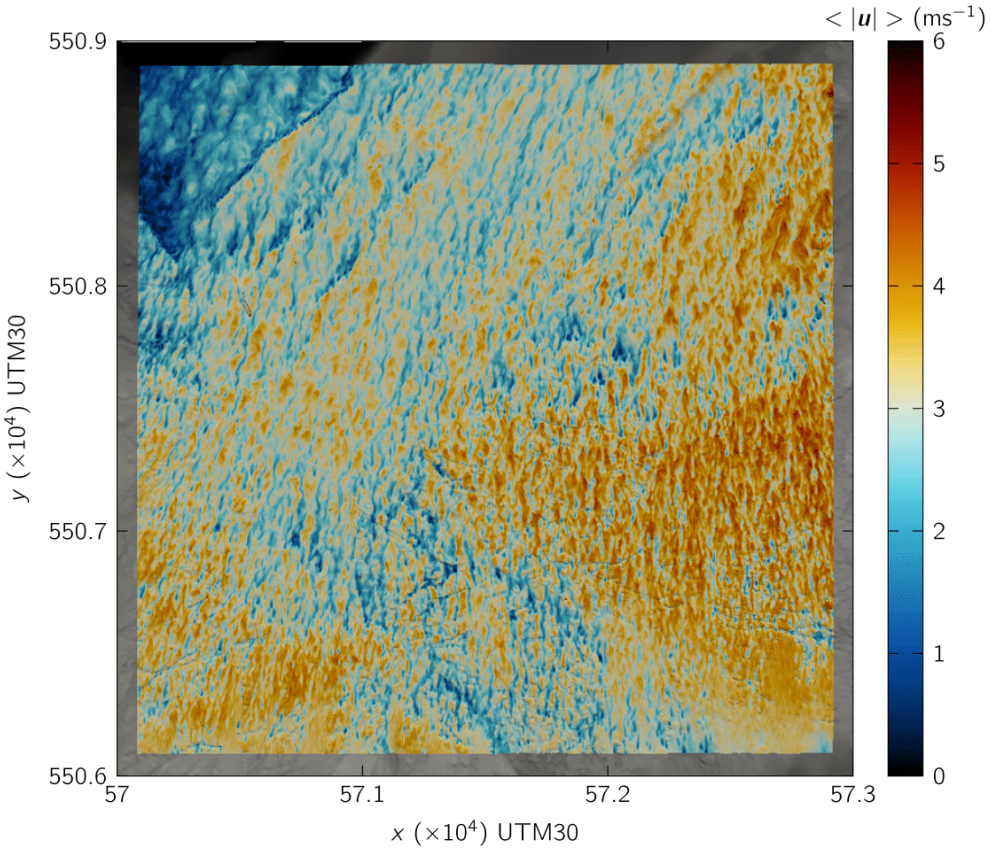

Figure 5.17: Velocity magnitude at the free surface on the 07/10/17 at 7 a.m.

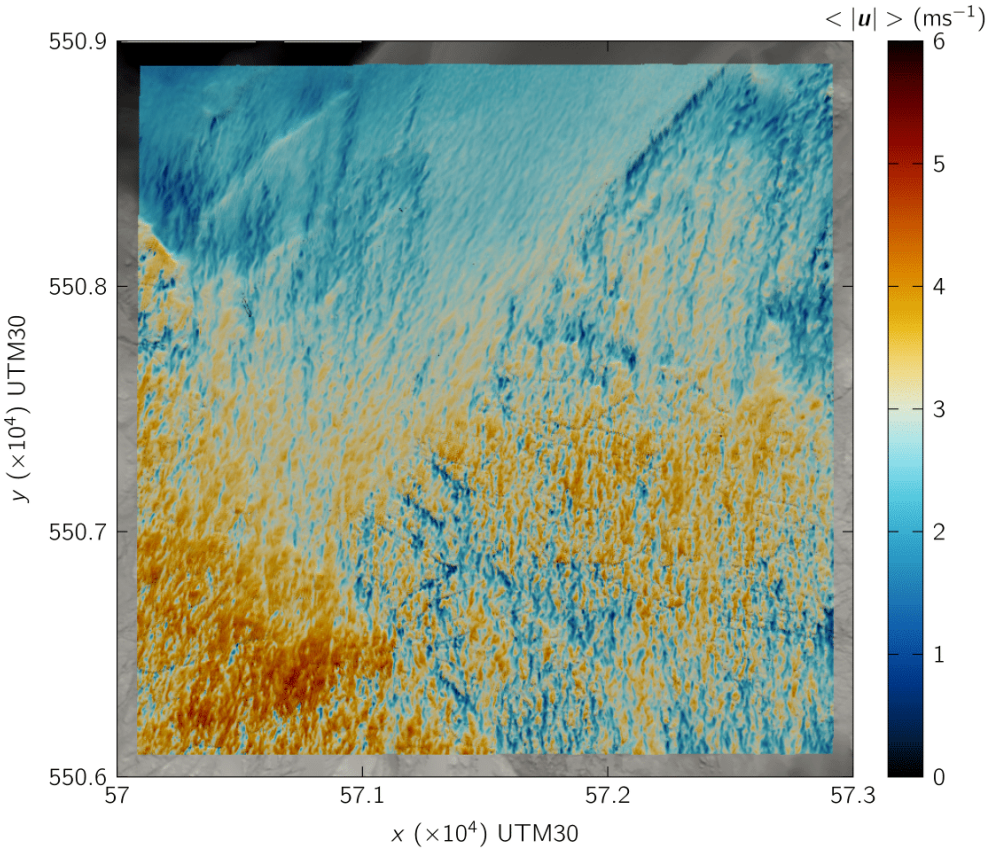

Figure 5.18: Velocity magnitude at the free surface on the 07/10/17 at 1 a.m.

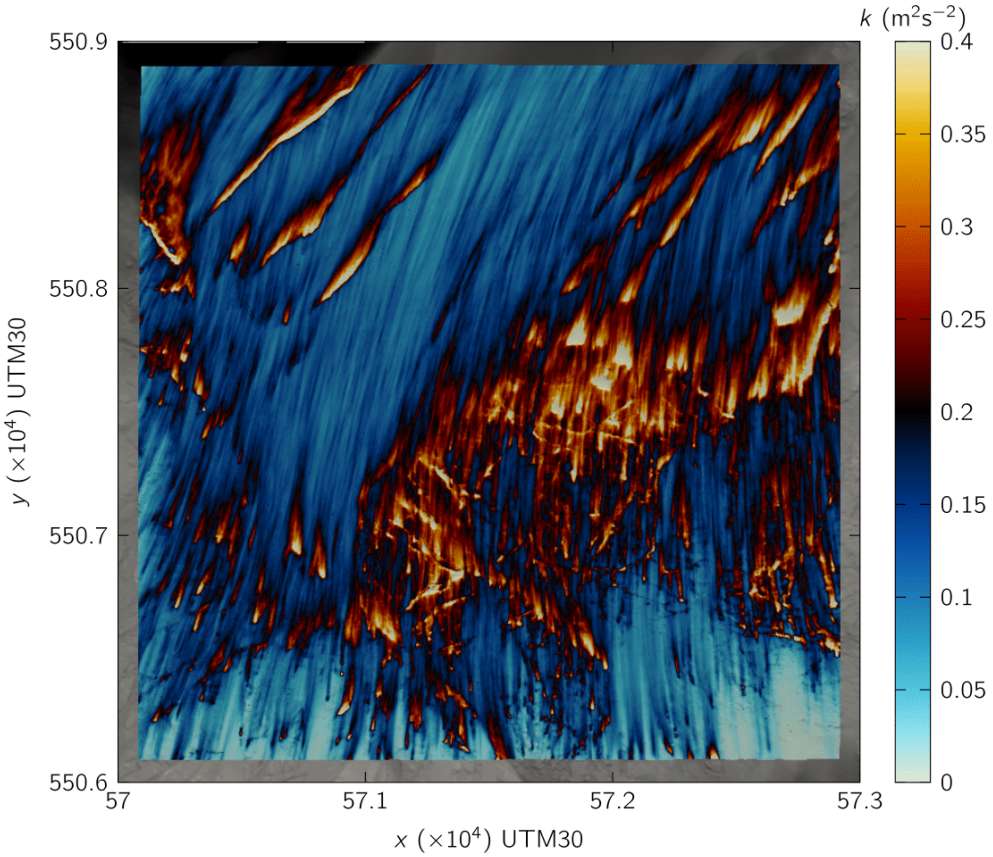

Figure 5.19: Turbulence kinetic energy at 8m above the seabed on the 07/10/17 at 7 a.m.

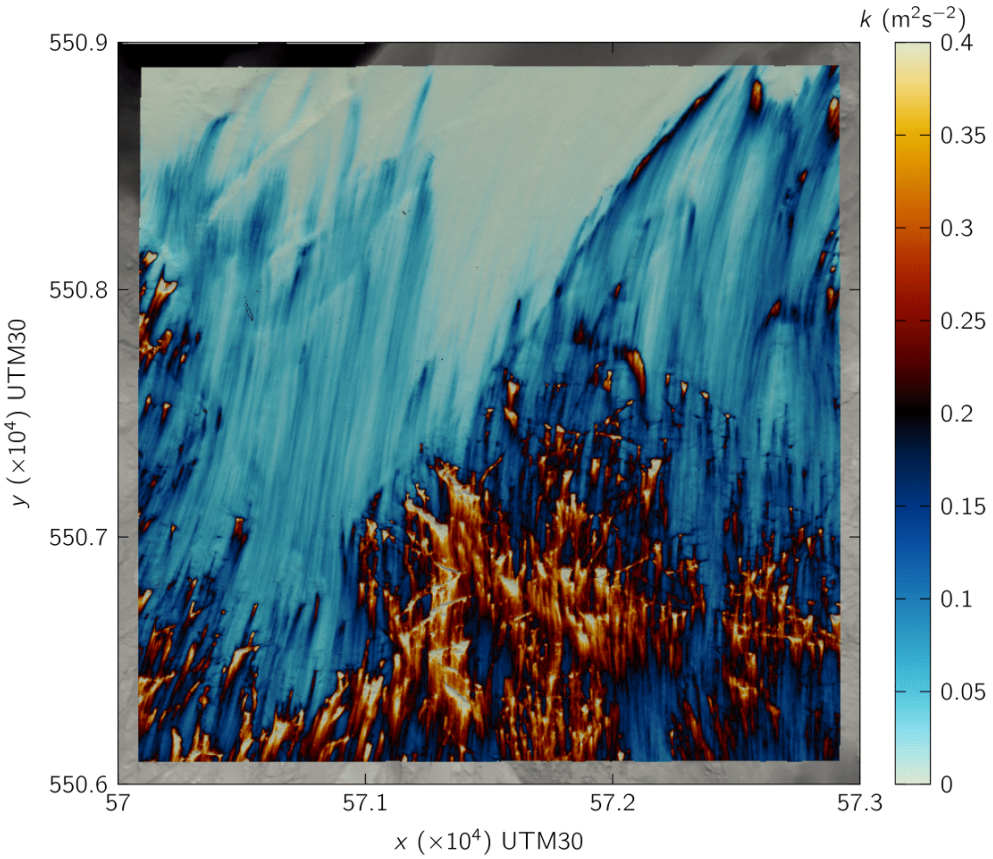

Figure 5.20: Turbulence kinetic energy at 8m above the seabed on the 07/10/17 at 1 a.m.

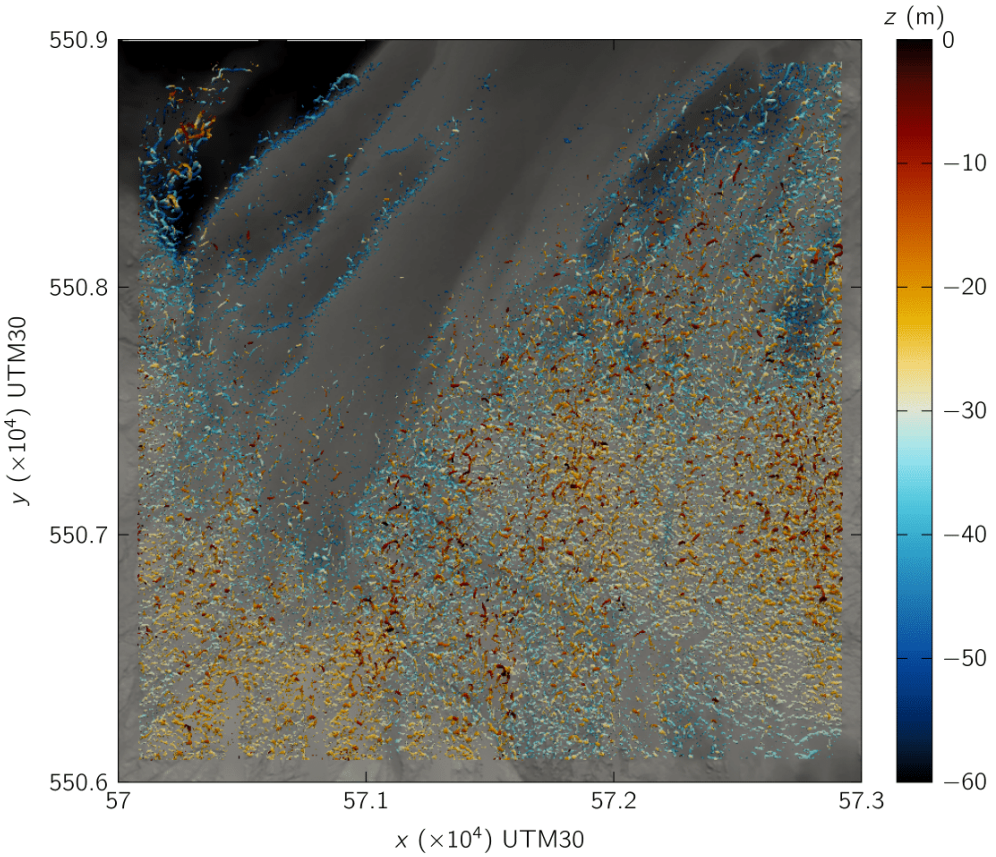

Figure 5.21: Turbulent structures identified during the ebb with the λ_2 criterion coloured by the elevation on the 07/10/17 at 7 a.m.

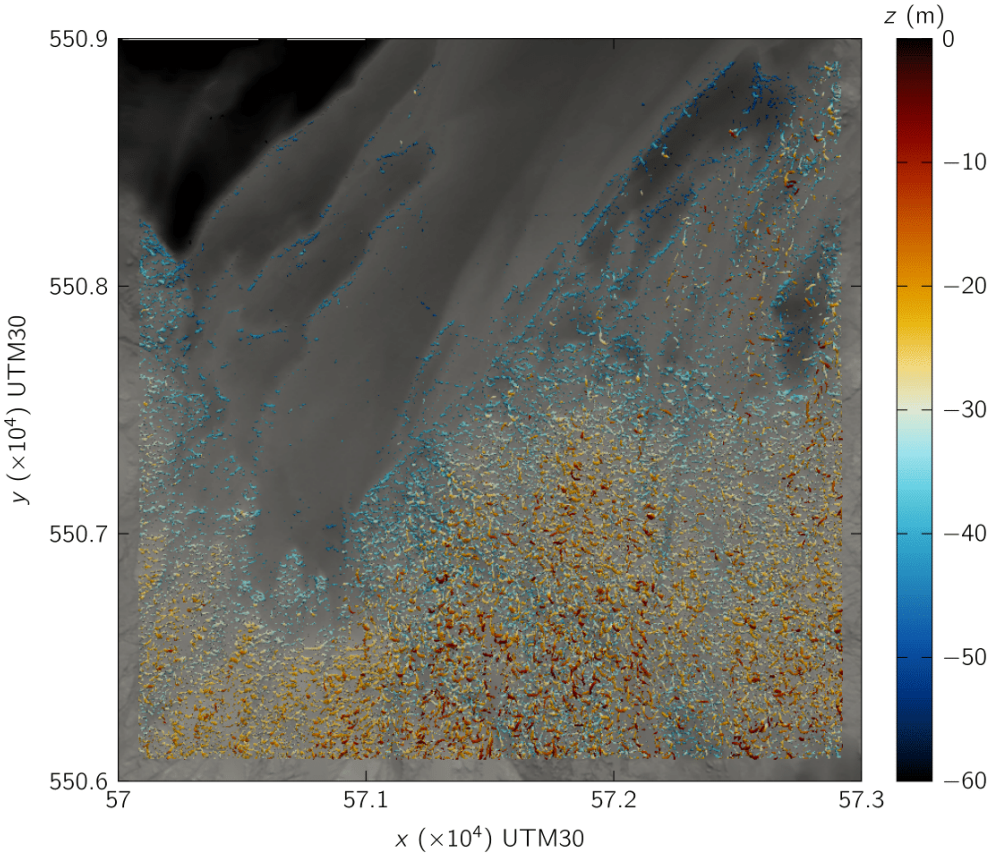

Figure 5.22: Turbulent structures identified during the flood with the λ_2 criterion coloured by the elevation on the 07/10/17 at 1 a.m.

Figure 5.23 presents isosurfaces of the λ_2 criterion, showing hairpin vortices and boils on a small plot of the Alderney Race seabed.

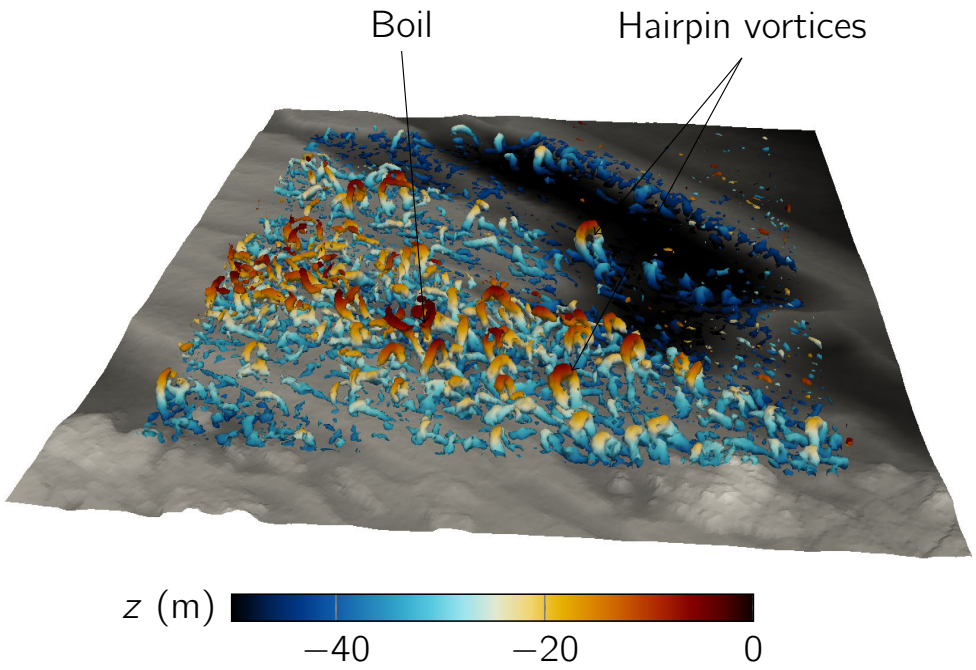

Figure 5.23: Snapshot of λ_2 isosurfaces coloured by the elevation in the Alderney Race.

With regards to all results, there is no contradiction between numerical and experimental approaches, but rather a form of complementarity. Compared to in-situ measurement data, the main drawback of the LESs is to not accurately reproduce the turbulence statistics in upper water column. However, it considerably enriches knowledge and understanding of the turbulence causes by providing results over a whole 3D domain. An interpretation of the combined results is therefore pertinent.

Firstly, the most turbulent regions are located. The rocky plateau, the dune crest and the rift appear to be the areas with the highest turbulent kinetic energy, as well as the most coherent structures identified with the λ_2 criterion. Some hairpin vortices and boils have been observed over the plateau for both ebb and flood waters. A smoother parcel can nevertheless be perceived southeast of the domain (near coordinates $[57.24, 550.65]\times10^4$ UTM30) with a much lower turbulence level.

Concerning the comparison between flood and ebb tides, the flood waters seem to be the more turbulent in the considered area. The velocity magnitude is indeed higher in the ascending water phase, and the rocky plateau influence is greater because of the flow orientation (from south to north) in respect to its location (south). Furthermore, despite the fact that the turbulent kinetic energy is lower during the low tide (29/09/17) compared to the high tide (07/10/17), it may be noted that the turbulent intensity remains similar. It reaches on both dates about $I_\infty = 20\%$ near the seabed and $I_\infty = 7\%$ in the upper water column.

5.3 Synthesis

A LES-based Alderney Race model has finally been built. Simulations have been performed on two distinct days, corresponding to respectively low and high tide coefficients. Results of mean velocity, water depth and turbulent statistics obtained with ADCP measurements , RANS and LES simulations are compared, and lead to satisfying agreements. The numerical results enable the identification of high current magnitude areas, highly turbulent regions as well as large coherent structures present in the flow. The use of finer meshes could nevertheless improve the results, as augur some preliminary simulations. Initial trends indicate turbulence mostly generated over the rocky plateau, as well as turbulent intensity reaching from $I_\infty = 7\%$ to $I_\infty = 20\%$ in the water column, independently of tide amplitudes.

Chapter 6

Main conclusions and perspectives

La production d'énergie verte devient essentielle pour notre société. La transition amorcée il y a quelques années cherche à équilibrer le mix énergétique en privilégiant les énergies renouvelables, dont l'énergie hydrolienne fait partie. Cette technologie, en plein développement, consiste à installer des turbines immergées dans des sites marins caractérisés par des intensités de courant très élevées. Par ailleurs, la France a la chance de posséder dans ses eaux le Raz Blanchard où la vitesse du courant peut atteindre $5\ ms^{-1}$*. Avant d'installer les machines, il est indispensable de caractériser de manière approfondie ces écoulements, et particulièrement la turbulence, qui peut influencer la performance et la durée de vie des turbines, comme cela a été présenté dans le chapitre 1. On s'interroge actuellement sur l'origine des vortex imposants observés dans le Raz Blanchard. L'une des hypothèses pourrait être la morphologie du fond marin, rocheux et très rugueux.*

La modélisation numérique représente un outil efficace pour caractériser les écoulements de grandes dimensions. Des logiciels tels que la suite TELEMAC-MASCARET permettent de modéliser des écoulements environnementaux, comme les rivières ou les océans. Dans ces algorithmes, la turbulence est modélisée via la méthode dite RANS, qui consiste à résoudre l'écoulement moyenné. Cette fermeture turbulente n'est pas assez précise pour étudier la naissance et le mouvement des structures turbulentes, or l'approche LES l'est. Au commencement de cette thèse, une telle méthodologie n'était pas intégrée dans les divers logiciels environnementaux, du fait de son coût calculatoire conséquent. Cependant les ressources informatiques se sont développées. Un récapitulatif des méthodes de type LES et des méthodes hybrides telles que la DES (chapitre 2) a conduit à l'établissement de la technique à introduire dans le code TELEMAC-3D. Elle s'appuie sur des modèles de sous-maille basiques, qui ont fait leur preuve tout en restant simpliste, et pouvant être utilisés avec la loi de parois déjà présente dans le solveur.

Après avoir présenté les contextes théoriques et numériques de TELEMAC-3D (chapitre 3), la méthodologie employée pour faire évoluer le code afin d'y intégrer la nouvelle approche LES est décrite (chapitre 4). Cela consiste en l'ajout des modèles de sous-maille, de conditions aux limites particulières, mais aussi de schémas numériques supplémentaires afin de garantir la précision du transport des fluctuations turbulentes. Le solveur a par la suite été validé en simulant des écoulements pour lesquels des données expérimentales ont été recueillies. L'écoulement développé derrière un pilier cylindrique a par exemple été analysé. Les résultats se sont montrés prometteurs, puisque les champs moyens ainsi que les statistiques turbulentes correspondent aux profils expérimentaux. Enfin, un premier cas en rapport avec le sujet principal de cette thèse a été étudié : l'écoulement au-dessus de dunes. Les différentes grandeurs calculées ont pareillement été convenablement estimées. De plus, la formation de structures turbulentes cohérentes au pied des dunes et leur évolution vers la surface libre ont pu être identifiées. Cela renforce la première hypothèse soutenant que le fond du Raz Blanchard est responsable de la formation de structures turbulentes cohérentes de nature à endommager les futures hydroliennes. Néanmoins les zones côtières étant étendues, l'application de la modélisation LES sur son ensemble s'est montrée irréalisable. Une LES imbriquée a donc été introduite. Cela consiste à concentrer la résolution LES dans une zone spécifique et d'utiliser la méthode RANS ailleurs. Cette approche s'est révélée indispensable puisqu'un modèle d'écoulement marin nécessite l'utilisation d'un domaine spatial suffisamment étendu pour y reproduire les différentes harmoniques de marée.

Ceci était le préambule à l'utilisation d'une telle approche LES à la zone du Raz Blanchard (chapitre 5). Les résultats obtenus avec les méthodes RANS et LES sont comparés aux données issues de mesures ADCP, réalisées lors d'une campagne du projet THYMOTE. Malgré la discrétisation grossière utilisée, les résultats LES permettent une description satisfaisante de la turbulence du Raz Blanchard. L'identification de zones de détachement tourbillonnaire a par ailleurs pu être réalisée. L'emplacement de ces espaces représente un enjeu très important pour pouvoir localiser les hydroliennes et anticiper leur performance.

Ce travail amorce de futures recherches. Un modèle a été développé et appliqué avec succès au Raz Blanchard, mais beaucoup de travail reste à faire. La méthodologie peut évidemment être améliorée en termes de processus numériques, de méthodes

pour la modélisation de la turbulence ainsi qu'en termes de performance de calcul. Entre autres, la résolution des équations de Navier-Stokes ne repose pas sur des schémas d'ordre élevé pour chacune des étapes. Il pourrait être intéressant d'améliorer la méthode de projection de Chorin-Temam, ainsi que le calcul de l'élévation de la surface libre proposés dans TELEMAC-3D.

Les perspectives physiques concernant les écoulements à petite échelle sont prometteuses, car la méthode améliore la description des statistiques des écoulements ainsi que l'étude de leurs structures tourbillonnantes. Une démarche fascinante serait par ailleurs de mettre en œuvre une décomposition orthogonale aux valeurs propres, qui permettrait le suivi spatio-temporel de vortex [44]. Outre l'hydrodynamique, la méthode permettrait aussi de mieux appréhender les processus physiques complexes existant dans les milieux environnementaux, tels que le transport sédimentaire ou la propagation des vagues.

En ce qui concerne le Raz Blanchard, seules quelques conditions de marée ont pu être simulées, en raison principalement du coût de calcul. Beaucoup de conditions devront être étudiées à l'avenir. La combinaison de l'effet des vagues et de la turbulence pourrait également être étudiée. La caractérisation des ressources marines est un domaine d'étude très actif dans le monde entier, notamment dans le cadre du développement des énergies marines renouvelables. En ce qui concerne les premiers résultats présentés dans ces travaux, cette approche pourrait également être étendue à d'autres sites et contribuer ainsi aux travaux préliminaires de l'installation de fermes d'hydroliennes ou de parcs éoliens offshore.

Green energy generation is becoming essential to our society. The transition initiated few years ago consists of balancing the energy mix by prioritizing renewable energy, for instance tidal turbines. This technology in full development involves installing submerged turbines in marine sites characterized by very high current intensities. France is also fortunate to have in its waters the Alderney Race area (Raz Blanchard in French) where the velocity magnitude can reach $5 \mathrm{ms}^{-1}$. Before installing the machines, it is essential to precisely characterize these flows and more specifically the turbulence, as this can have impacts on the turbines' performance and life time as discussed in Chapter 1. One of the questions concerns the origin and the behaviour of large eddies in the Alderney Race. One of the hypotheses could be the morphology of the bottom: the seabed is rocky and very rugged.

Numerical modelling constitutes an efficient tool to characterize tidal flows over large areas. Specific softwares such as the TELEMAC-MASCARET suite enable the simulation of free surface environmental flows, from rivers to oceans. In these solvers, turbulence is modeled using the Reynolds Averaged Navier-Stokes method, which involves solving the averaged flow. This turbulent closure is not accurate enough to study the birth and the motion of large turbulent structures, but Large-Eddy-Simulation could be. This technique was not implemented in environmental softwares at the beginning of this thesis due to its computational cost. However, computational resources have increased. An overwiew of the LES methods and mixed methods such as the Detached-Eddy-Simulations have led (Chapter 2) to the selection of the technique to be implemented in the code TELEMAC-3D. It relies on basic subgrid models, since they have shown very good results for a low computational cost and can then be used with the already implemented wall model of the solver.

After a presentation of the theoretical and numerical aspects of TELEMAC-3D (Chapter 3), the methodology used to make the code evolve to integrate the selected LES approach has been described (Chapter 4). It involves subgrid models, particular boundary conditions but also additional numerical schemes, permitting the accurate propagation of turbulent fluctuations. The solver has then been validated by simulating flows for which experimental data have been gathered. For instance, a flow around a cylindrical pier has been investigated. Promising results have been ob-

tained since both the averaged fields and turbulence statistics fit with experimental profiles. Finally, a preliminary case directly related to the main topic of this thesis has been studied: the flow over dunes. The results from this have shown that the various computed outputs have also been well estimated compared to validation data. Moreover, the coherent turbulent eddies generation on the bottom and their evolution towards the free surface have been identified. It reinforces the first hypothesis that the bottom of the Alderney Race is responsible for the generation of large coherent turbulent structures, which could cause deteriorations of any future tidal turbines placed in it. Nevertheless, coastal areas are large and the application of a full LES method has been seen as impracticable. The embedded LES method has therefore been introduced. It consists of focusing the LES resolution on a specific area, whereas the turbulence modelling is treated with a RANS method elsewhere. In fact, this approach was needed since an accurate model of tidal flows requires performing simulations over a sufficiently large spatial domain to reproduce all the tidal harmonics.

This was a preamble of a LES method application to a full domain of the Alderney Race (Chapter 5). Results obtained with both RANS and LES methodologies have been compared with ADCP measurements obtained during a field survey, realized in the framework of the THYMOTE project. Despite the very coarse discretisation used for these models, the LES results enable a decent characterisation of turbulence statistics of the Alderney Race flow. Moreover, it permits the identification of vortex shedding areas. The spatial position of these large eddies is of huge importance to localize the turbines and to foresee their lifetime.

Within this thesis. a model has been successfully developed and applied to better understand the flow behaviour in the Alderney Race. During this study, further work on this subject has been identified. The methodology can be improved in terms of numerical processes, turbulence modelling methods and calculation performance. For instance, the Navier-Stokes equations resolution does not rely on high order schemes for each step. It could be interesting to upgrade the Chorin-Temam projection method, as well as the free surface elevation calculation proposed in TELEMAC-3D. Physical outlooks about small scale flows are promising, since the method enables a better description of flow statistics and provides the opportunity to study their unsteady behaviour as well as their swirling structures. An example of a future study

could be the implementation of a Proper Orthogonal Decomposition, which would enable the vortices spatio-temporal tracking [44]. In addition to hydrodynamics, the method would indeed permit the better grasp of complex physical processes existing in environmental flows, such as sediment transport or wave propagation.

Concerning the Alderney Race, only a limited number of tidal conditions have been simulated, mainly due to the computational cost. There are a number of additional conditions that could be investigated which would be of value, for example the combination of waves and turbulence. The tidal resources characterisation is a very active field of study worldwide, particularly in the framework of the development of renewable marine energies. Regarding the first results presented in that work, this approach could also be extended to other tidal flows, and so contribute to the groundwork for the establishment of tidal turbine farms or offshore wind turbine farms.

Bibliography

[1] Carte de natures de fond au 1/500 000. https://diffusion.shom.fr.

[2] *SISYPHE manual*. http://www.opentelemac.org/downloads/MANUALS/.

[3] *TELEMAC-3D theory guide*. http://www.opentelemac.org/downloads/MANUALS/.

[4] *TOMAWAC manual*. http://www.opentelemac.org/downloads/MANUALS/.

[5] Rapport de campagne – campagne de mesures dans le raz blanchard. Technical report, THYMOTE, 2018.

[6] M Abkar, HJ Bae, and P Moin. Minimum-dissipation scalar transport model for large-eddy simulation of turbulent flows. *Physical Review Fluids*, 1(4):041701, 2016.

[7] M Abkar and P Moin. Large-eddy simulation of thermally stratified atmospheric boundary-layer flow using a minimum dissipation model. *Boundary-Layer Meteorology*, 165(3):405–419, 2017.

[8] I Afgan, J McNaughton, S Rolfo, DD Apsley, T Stallard, and P Stansby. Turbulent flow and loading on a tidal stream turbine by les and rans. *International Journal of Heat and Fluid Flow*, 43:96–108, 2013.

[9] U Ahmed, DD Apsley, I Afgan, T Stallard, and PK Stansby. Fluctuating loads on a tidal turbine due to velocity shear and turbulence: comparison of cfd with field data. *Renewable Energy*, 112:235–246, 2017.

[10] AS Bahaj. Generating electricity from the oceans. *Renewable and Sustainable Energy Reviews*, 15(7):3399–3416, 2011.

[11] AS Bahaj and L Myers. Analytical estimates of the energy yield potential from the alderney race (channel islands) using marine current energy converters. *Renewable energy*, 29(12):1931–1945, 2004.

[12] F Bashforth and JC Adams. *An attempt to test the theories of capillary action: by comparing the theoretical and measured forms of drops of fluid*. University Press, 1883.

[13] GK Batchelor. *The theory of homogeneous turbulence*. Cambridge university press, 1953.

[14] GK Batchelor. *An introduction to fluid dynamics*. Cambridge university press, 2000.

[15] Z Bedri, M Bruen, A Dowley, and B Masterson. A three-dimensional hydro-environmental model of dublin bay. *Environmental Modeling & Assessment*, 16(4):369–384, 2011.

[16] J Best. The fluid dynamics of river dunes: A review and some future research directions. *Journal of Geophysical Research: Earth Surface*, 110(F4), 2005.

[17] T Blackmore, B Gaurier, L Myers, G Germain, and AS Bahaj. The effect of freestream turbulence on tidal turbines. In *Proceedings of the 11th European Wave and Tidal Energy Conference, Nantes, France*, 2015.

[18] T Blackmore, L Myers, and AS Bahaj. Effects of turbulence on tidal turbines: Implications to performance, blade loads, and condition monitoring. *International Journal of Marine Energy*, 14:1–26, 2016.

[19] L Blunden, SG Haynes, and AS Bahaj. Dynamic sandbanks in close proximity to sites of interest for tidal current power extraction. *Proceedings of the 4th Asian Wave and Tidal Energy Conference, Taipei, 08B4-3-1.*, 2018.

[20] LS Blunden and AS Bahaj. Tidal energy resource assessment for tidal stream generators. *Proceedings of the Institution of Mechanical Engineers, Part A: Journal of Power and Energy*, 221(2):137–146, 2007.

[21] J Bonillo. *Un modelo de transporte de sustancias solubles para flujos turbulentos en lámina libre*. PhD thesis, Tesis Doctoral, A Coruna, 2000.

[22] J Boussinesq. *Essai sur la théorie des eaux courantes*. Impr. nationale, 1877.

[23] H Boye, E Caquot, P Clement, L de La Cochetiere, JM Nataf, and P Sergent. Rapport de la mission d'étude sur les énergies marines renouvelables. *Paris: Ministère de l'écologie, du développement durable et de l'énergie*, 2013.

[24] P Bradshaw, DH Ferriss, and NP Atwell. Calculation of boundary-layer development using the turbulent energy equation. *Journal of Fluid Mechanics*, 28(3):593–616, 1967.

[25] AN Brooks and TJR Hughes. Streamline upwind/petrov-galerkin formulations for convection dominated flows with particular emphasis on the incompressible navier-stokes equations. *Computer methods in applied mechanics and engineering*, 32(1-3):199–259, 1982.

[26] R Campbell, A Martinez, C Letetrel, and A Rio. Methodology for estimating the french tidal current energy resource. *International Journal of Marine Energy*, 19:256–271, 2017.

[27] C Carlier, P Mycek, B Gaurier, G Germain, G Pinon, and E Rivoalen. Etude expérimentale et numérique du comportement d'hydroliennes à axe horizontal. In *XIIIèmes Journées Nationales Génie Côtier–Génie Civil Dunkerque, 2-4 juillet 2014*, 2014.

[28] CF Carmer. Shallow turbulent wake flows: momentum and mass transfer due to large-scale coherent vortical structures. 2009.

[29] L Cea, J Puertas, and ME Vázquez-Cendón. Depth averaged modelling of turbulent shallow water flow with wet-dry fronts. *Archives of Computational Methods in Engineering*, 14(3):303–341, 2007.

[30] DR Chapman. Computational aerodynamics development and outlook. *AIAA journal*, 17(12):1293–1313, 1979.

[31] P Chassaing. *Turbulence en mécanique des fluides*. 2000.

[32] JP Chollet and M Lesieur. Parameterization of small scales of three-dimensional isotropic turbulence utilizing spectral closures. *Journal of the Atmospheric Sciences*, 38(12):2747–2757, 1981.

[33] AJ Chorin. Numerical solution of the navier-stokes equations. *Mathematics of computation*, 22(104):745–762, 1968.

[34] THE Clark. Turbulence in marine environments (time): A framework for understanding turbulence and its effects on tidal devices. *Proceedings of the 11th European Wave and Tidal Energy Conference, Nantes, 08B4-3-1.*, 2015.

[35] R Coggan and M Diesing. The seabed habitats of the central english channel: A generation on from holme and cabioch, how do their interpretations match-up to modern mapping techniques? *Continental Shelf Research*, 31(2):S132–S150, 2011.

[36] G Constantinescu, M Koken, and J Zeng. The structure of turbulent flow in an open channel bend of strong curvature with deformed bed: Insight provided by detached eddy simulation. *Water Resources Research*, 47(5), 2011.

[37] G Constantinescu, S Miyawaki, B Rhoads, and A Sukhodolov. Numerical analysis of the effect of momentum ratio on the dynamics and sediment-entrainment capacity of coherent flow structures at a stream confluence. *Journal of Geophysical Research: Earth Surface*, 117(F4), 2012.

[38] L Davidson. Large eddy simulations: how to evaluate resolution. *International Journal of Heat and Fluid Flow*, 30(5):1016–1025, 2009.

[39] M De Marchis, B Milici, and E Napoli. Numerical observations of turbulence structure modification in channel flow over 2d and 3d rough walls. *International Journal of Heat and Fluid Flow*, 56:108–123, 2015.

[40] M De Marchis, E Napoli, and V Armenio. Turbulence structures over irregular rough surfaces. *Journal of Turbulence*, (11):N3, 2010.

[41] H Deconinck, H Paillere, R Struijs, and Philip L Roe. Multidimensional upwind schemes based on fluctuation-splitting for systems of conservation laws. *Computational Mechanics*, 11(5-6):323–340, 1993.

[42] J-P Demailly. *Analyse numérique et équations différentielles-4ème Ed*. EDP sciences, 2016.

[43] R Dewey and S Stringer. Reynolds stresses and turbulent kinetic energy estimates from various adcp beam configurations: Theory. *J. of Phys. Ocean*, pages 1–35, 2007.

[44] P Druault, P Guibert, and F Alizon. Use of proper orthogonal decomposition for time interpolation from piv data. *Experiments in fluids*, 39(6):1009–1023, 2005.

[45] PA Durbin and BAP Reif. *Statistical theory and modeling for turbulent flows*. John Wiley & Sons, 2011.

[46] G Egbert and S Erofeeva. Osu tidal data inversion, 2010.

[47] G Eitel-Amor, R Örlü, P Schlatter, and O Flores. Hairpin vortices in turbulent boundary layers. *Physics of Fluids*, 27(2):025108, 2015.

[48] EH Fernandes, KR Dyer, and LFH Niencheski. Calibration and validation of the telemac-2d model to the patos lagoon (brazil). *Journal of Coastal Research*, pages 470–488, 2001.

[49] Jason Frank, Willem Hundsdorfer, and JG Verwer. On the stability of implicit-explicit linear multistep methods. *Applied Numerical Mathematics*, 25(2-3):193–205, 1997.

[50] ST Fredriksson, G Broström, M Jansson, H Nilsson, and B Bergqvist. Large eddy simulation of the tidal power plant deep green using the actuator line method. In *IOP Conference Series: Materials Science and Engineering*, volume 276, page 012014. IOP Publishing, 2017.

[51] J Fröhlich, CP Mellen, W Rodi, L Temmerman, and MA Leschziner. Highly resolved large-eddy simulation of separated flow in a channel with streamwise periodic constrictions. *Journal of Fluid Mechanics*, 526:19–66, 2005.

[52] J Fröhlich and D von Terzi. Hybrid les/rans methods for the simulation of turbulent flows. *Progress in Aerospace Sciences*, 44(5):349–377, 2008.

[53] TB Gatski, MY Hussaini, and JL Lumley. *Simulation and modeling of turbulent flows. ICASE/LaRC Series in Computational Science and Engineering*. Oxford University Press, USA, 1996.

[54] M Germano, U Piomelli, P Moin, and WH Cabot. A dynamic subgrid-scale eddy viscosity model. *Physics of Fluids A: Fluid Dynamics (1989-1993)*, 3(7):1760–1765, 1991.

[55] PM Gresho. Incompressible fluid dynamics: some fundamental formulation issues. *Annual review of fluid mechanics*, 23(1):413–453, 1991.

[56] M Grondeau, P Mercier, S Guillou, Y Méar, JC Poirier, and E Poizot. Quelle turbulence ambiante pour la simulation numérique lbm-les d'un environnement hydrolien? lattice boltzmann method turbulence modeling for tidal power environment simulation. 2016.

[57] N Guillou, G Chapalain, and SP Neill. The influence of waves on the tidal kinetic energy resource at a tidal stream energy site. *Applied Energy*, 180:402–415, 2016.

[58] S Guillou, N Barbry, and KD Nguyen. Calcul numérique des ondes de surface par une méthode de projection avec un maillage eulérien adaptatif. *Comptes Rendus de l'Académie des Sciences-Series IIB-Mechanics*, 328(12):875–881, 2000.

[59] K Gustafson and T Abe. The third boundary condition—was it robin's? *The Mathematical Intelligencer*, 20(1):63–71, 1998.

[60] L Halpern and M Schatzman. Artificial boundary conditions for incompressible viscous flows. *SIAM Journal on Mathematical Analysis*, 20(2):308–353, 1989.

[61] FR Hama. Boundary layer characteristics for smooth and rough surfaces. *Trans. Soc. Nav. Arch. Marine Engrs.*, 62:333–358, 1954.

[62] A Hay. Turbulence and bottom stress in grand passage and minas passage. Technical report, Department of Oceanography, Dalhousie University, 2014.

[63] MR Head and P Bandyopadhyay. New aspects of turbulent boundary-layer structure. *Journal of fluid mechanics*, 107:297–338, 1981.

[64] JM Hervouet. Telemac modelling system: an overview. *Hydrological Processes*, 14(13):2209–2210, 2000.

[65] JM Hervouet. *Hydrodynamics of free surface flows: modelling with the finite element method*. John Wiley & Sons, 2007.

[66] C Hinterberger, J Fröhlich, and W Rodi. Three-dimensional and depth-averaged large-eddy simulations of some shallow water flows. *Journal of Hydraulic Engineering*, 133(8):857–872, 2007.

[67] J Hong, J Katz, C Meneveau, and MP Schultz. Coherent structures and associated subgrid-scale energy transfer in a rough-wall turbulent channel flow. *Journal of Fluid Mechanics*, 712:92–128, 2012.

[68] J Hong, J Katz, and MP Schultz. Near-wall turbulence statistics and flow structures over three-dimensional roughness in a turbulent channel flow. *Journal of Fluid Mechanics*, 667:1–37, 2011.

[69] JCR Hunt, AA Wray, and P Moin. Eddies, streams, and convergence zones in turbulent flows. 1988.

[70] M Ikhennicheu, B Gaurier, P Druault, and G Germain. Experimental analysis of the floor inclination effect on the turbulent wake developing behind a wall mounted cube. *European Journal of Mechanics-B/Fluids*, 72:340–352, 2018.

[71] M Ikhennicheu, G Germain, P Druault, and B Gaurier. Experimental study of coherent flow structures past a wall-mounted square cylinder. *Experiment in Fluids*, 2018.

[72] JM Janin and X Blanchard. *Simulation des courants de marée en Manche et Proche Atlantique*. Électricité de France, Direction des études et recherches, Service applications de l'électricité et environnement, Département laboratoire national d'hydraulique, 1993.

[73] Jacek A Jankowski. *A non-hydrostatic model for free surface flows*. PhD thesis, Inst. für Strömungsmechanik und Elektronisches Rechnen im Bauwesen, 1999.

[74] N Jarrin, S Benhamadouche, D Laurence, and R Prosser. A synthetic-eddy-method for generating inflow conditions for large-eddy simulations. *International Journal of Heat and Fluid Flow*, 27(4):585–593, 2006.

[75] J Jeong and F Hussain. On the identification of a vortex. *Journal of fluid mechanics*, 285:69–94, 1995.

[76] JE Jones and AM Davies. Application of a finite element model (telemac) to computing the wind induced response of the irish sea. *Continental Shelf Research*, 26(12-13):1519–1541, 2006.

[77] A Kadota and I Nezu. Three-dimensional structure of space-time correlation on coherent vortices generated behind dune crest. *Journal of Hydraulic Research*, 37(1):59–80, 1999.

[78] M Klein, A Sadiki, and J Janicka. A digital filter based generation of inflow data for spatially developing direct numerical or large eddy simulations. *Journal of computational Physics*, 186(2):652–665, 2003.

[79] AN Kolmogorov. Dissipation of energy in the locally isotropic turbulence. *Proceedings: Mathematical and Physical Sciences*, 434(1890):15–17, 1941.

[80] BE Launder and BI Sharma. Application of the energy-dissipation model of turbulence to the calculation of flow near a spinning disc. *Letters in heat and mass transfer*, 1(2):131–137, 1974.

[81] S Lee, SK Lele, and P Moin. Simulation of spatially evolving turbulence and the applicability of taylor's hypothesis in compressible flow. *Physics of Fluids A: Fluid Dynamics (1989-1993)*, 4(7):1521–1530, 1992.

[82] A Leonard. Energy cascade in large-eddy simulations of turbulent fluid flows. In *Advances in geophysics*, volume 18, pages 237–248. Elsevier, 1975.

[83] M Lesieur and R Rogallo. Large-eddy simulation of passive scalar diffusion in isotropic turbulence. *Physics of Fluids A: Fluid Dynamics (1989-1993)*, 1(4):718–722, 1989.

[84] Y Li, JA Colby, N Kelley, B Thresher, Rand Jonkman, and S Hughes. Inflow measurement in a tidal strait for deploying tidal current turbines: lessons, opportunities and challenges. In *ASME 2010 29th international conference on ocean, offshore and arctic engineering*, pages 569–576. American Society of Mechanical Engineers, 2010.

[85] DK Lilly. The representation of small-scale turbulence in numerical simulation experiments. 1966.

[86] DK Lilly. A proposed modification of the germano subgrid-scale closure method. *Physics of Fluids A: Fluid Dynamics (1989-1993)*, 4(3):633–635, 1992.

[87] E Lorin, ABH Ali, and A Soulaimani. A positivity preserving finite element–finite volume solver for the spalart–allmaras turbulence model. *Computer methods in applied mechanics and engineering*, 196(17-20):2097–2116, 2007.

[88] H Lu, CJ Rutland, and LM Smith. A priori tests of one-equation les modeling of rotating turbulence. *Journal of Turbulence*, (8):N37, 2007.

[89] J MacEnri, M Reed, and T Thiringer. Influence of tidal parameters on seagen flicker performance. *Phil. Trans. R. Soc. A*, 371(1985):20120247, 2013.

[90] F Mathey, D Cokljat, JP Bertoglio, and E Sergent. Specification of inlet boundary condition using vortex method. *Turbulence, Heat and Mass Transfer, Vol. 4*, 2003.

[91] R McSherry, J Grimwade, I Jones, S Mathias, A Wells, and A Mateus. 3d cfd modelling of tidal turbine performance with validation against laboratory experiments. In *9th European Wave and Tidal Energy Conference*, 2011.

[92] C Mellen, J Fröhlich, and W Rodi. Large-eddy simulation of the flow over periodic hills. *16th IMACS world congress*, 2000.

[93] FR Menter. Eddy viscosity transport equations and their relation to the k-epsilon model. *NASA STI/Recon Technical Report N*, 95:14273, 1994.

[94] B Milici, M De Marchis, G Sardina, and E Napoli. Effects of roughness on particle dynamics in turbulent channel flows: a dns analysis. *Journal of Fluid Mechanics*, 739:465–478, 2014.

[95] IA Milne, AH Day, RN Sharma, and RGJ Flay. Blade loads on tidal turbines in planar oscillatory flow. *Ocean Engineering*, 60:163–174, 2013.

[96] P Moin. Advances in large eddy simulation methodology for complex flows. *International journal of heat and fluid flow*, 23(5):710–720, 2002.

[97] C Moulinec, C Denis, CT Pham, D Rougé, JM Hervouet, E Razafindrakoto, RW Barber, DR Emerson, and XJ Gu. Telemac: An efficient hydrodynamics suite for massively parallel architectures. *Computers & Fluids*, 51(1):30–34, 2011.

[98] P Mycek, B Gaurier, G Germain, G Pinon, and E Rivoalen. Experimental study of the turbulence intensity effects on marine current turbines behaviour. part i: One single turbine. *Renewable Energy*, 66:729–746, 2014.

[99] L Myers and AS Bahaj. Simulated electrical power potential harnessed by marine current turbine arrays in the alderney race. *Renewable energy*, 30(11):1713–1731, 2005.

[100] SP Neill, JR Jordan, and SJ Couch. Impact of tidal energy converter (tec) arrays on the dynamics of headland sand banks. *Renewable Energy*, 37(1):387–397, 2012.

[101] DE Neuenschwander. *Tensor calculus for physics: a concise guide*. JHU Press, 2014.

[102] F Nicoud and F Ducros. Subgrid-scale stress modelling based on the square of the velocity gradient tensor. *Flow, turbulence and Combustion*, 62(3):183–200, 1999.

[103] G Nolin, I Mary, and L Ta-Phuoc. Rans eddy viscosity reconstruction from les flow field for turbulent boundary layers. In *17th AIAA Computational Fluid Dynamics Conference*, page 4998, 2005.

[104] E Osalusi, J Side, and R Harris. Reynolds stress and turbulence estimates in bottom boundary layer of fall of warness. *International Communications in Heat and Mass Transfer*, 36(5):412–421, 2009.

[105] P Ouro and T Stoesser. Impact of environmental turbulence on the performance and loadings of a tidal stream turbine. *Flow, Turbulence and Combustion*, pages 1–27, 2018.

[106] HJ Paillere and H Deconinck. Multidimensional upwind residual distribution schemes for the euler and navier-stokes equations on unstructured grids. 1995.

[107] IL Pairaud, F Auclair, P Marsaleix, F Lyard, and A Pichon. Dynamics of the semi-diurnal and quarter-diurnal internal tides in the bay of biscay. part 2: Baroclinic tides. *Continental Shelf Research*, 30(3-4):253–269, 2010.

[108] Ivane L Pairaud, Florent Lyard, Francis Auclair, Thierry Letellier, and Patrick Marsaleix. Dynamics of the semi-diurnal and quarter-diurnal internal tides in the bay of biscay. part 1: Barotropic tides. *Continental Shelf Research*, 28(10-11):1294–1315, 2008.

[109] P Parnaudeau, J Carlier, D Heitz, and E Lamballais. Experimental and numerical studies of the flow over a circular cylinder at reynolds number 3900. *Physics of Fluids*, 20(8):085101, 2008.

[110] NA Phillips. A coordinate system having some special advantages for numerical forecasting. *Journal of Meteorology*, 14(2):184–185, 1957.

[111] L Pineau-Guillou. Previmer validation des atlas de composantes harmoniques de hauteurs et courants de marée. Technical report, Technical Report ODE/DYNECO/PHYSED/2013-03 version 1.0, Ifremer, 2013.

[112] U Piomelli and JR Chasnov. Large-eddy simulations: theory and applications. *Turbulence and transition modelling*, 2:269–336, 1996.

[113] DR Plew and CL Stevens. Numerical modelling of the effect of turbines on currents in a tidal channel–tory channel, new zealand. *Renewable Energy*, 57:269–282, 2013.

[114] C Polatel. *Large-scale roughness effect on free-surface and bulk flow characteristics in open-channel flows*. ProQuest, 2006.

[115] R Poletto, T Craft, and A Revell. A new divergence free synthetic eddy method for the reproduction of inlet flow conditions for les. *Flow, turbulence and combustion*, 91(3):519–539, 2013.

[116] SB Pope. *Turbulent FLows*. Cambridge University Press, 2000.

[117] L Prandtl. Bericht uber untersuchungen zur ausgebildeten turbulenz. *Zs. angew. Math. Mech.*, 5:136–139, 1925.

[118] BL Rhoads and AN Sukhodolov. Field investigation of three-dimensional flow structure at stream confluences: 1. thermal mixing and time-averaged velocities. *Water Resources Research*, 37(9):2393–2410, 2001.

[119] LF Richardson. *Weather prediction by numerical process*. Cambridge University Press, 2007.

[120] A Roberts, B Thomas, P Sewell, Z Khan, S Balmain, and J Gillman. Current tidal power technologies and their suitability for applications in coastal and marine areas. *Journal of Ocean Engineering and Marine Energy*, 2(2):227–245, 2016.

[121] SK Robinson. Coherent motions in the turbulent boundary layer. *Annual Review of Fluid Mechanics*, 23(1):601–639, 1991.

[122] W Rodi. Examples of calculation methods for flow and mixing in stratified fluids. *Journal of Geophysical Research: Oceans*, 92(C5):5305–5328, 1987.

[123] W Rodi. Large eddy simulation of river flows. In *Proceedings of the International Conference on Fluvial Hydraulics, Bundesanstalt fur Wasserbau, Karlsruhe, Germany*, pages 23–32, 2010.

[124] W Rozema, HJ Bae, P Moin, and R Verstappen. Minimum-dissipation models for large-eddy simulation. *Physics of Fluids*, 27(8):085107, 2015.

[125] P Sagaut. *Large eddy simulation for incompressible flows: an introduction*. Springer Science & Business Media, 2006.

[126] RL Sani and PM Gresho. Résumé and remarks on the open boundary condition minisymposium. *International Journal for Numerical Methods in Fluids*, 18(10):983–1008, 1994.

[127] S Šarić, S Jakirlić, M Breuer, B Jaffrézic, G Deng, O Chikhaoui, J Fröhlich, D Von Terzi, M Manhart, and N Peller. Evaluation of detached eddy simulations for predicting the flow over periodic hills. In *ESAIM: proceedings*, volume 16, pages 133–145. EDP Sciences, 2007.

[128] H Schlichting and K Gersten. *Boundary-layer theory*. Springer, 2016.

[129] P Schureman. Manual of harmonic analysis and prediction of tides. 1958.

[130] S Shamsoddin and F Porté-Agel. Large-eddy simulation of atmospheric boundary-layer flow through a wind farm sited on topography. *Boundary-layer meteorology*, 163(1):1–17, 2017.

[131] J Smagorinsky. General circulation experiments with the primitive equations: I. the basic experiment*. *Monthly weather review*, 91(3):99–164, 1963.

[132] CR Smith. A synthesized model of the near-wall behavior in turbulent boundary layers. Technical report, LEHIGH UNIV BETHLEHEM PA DEPT OF MECHANICAL ENGINEERING AND MECHANICS, 1984.

[133] PR Spalart and SR Allmaras. A one-equation turbulence model for aerodynamic flows. *Recherche Aerospatiale*, n/a(1):5–21, 1994.

[134] PR Spalart, WH Jou, M Strelets, SR Allmaras, et al. Comments on the feasibility of les for wings, and on a hybrid rans/les approach. *Advances in DNS/LES*, 1:4–8, 1997.

[135] T Stallard, R Collings, T Feng, and J Whelan. Interactions between tidal turbine wakes: experimental study of a group of three-bladed rotors. *Phil. Trans. R. Soc. A*, 371(1985):20120159, 2013.

[136] C Staquet. Two-dimensional secondary instabilities in a strongly stratified shear layer. *Journal of Fluid Mechanics*, 296:73–126, 1995.

[137] T Stoesser, C Braun, M Garcia-Villalba, and W Rodi. Turbulence structures in flow over two-dimensional dunes. *Journal of Hydraulic Engineering*, 134(1):42–55, 2008.

[138] R Temam. Sur l'approximation de la solution des équations de navier-stokes par la méthode des pas fractionnaires (ii). *Archive for Rational Mechanics and Analysis*, 33(5):377–385, 1969.

[139] J Thiébot, P Bailly du Bois, and S Guillou. Numerical modeling of the effect of tidal stream turbines on the hydrodynamics and the sediment transport–application to the alderney race (raz blanchard), france. *Renewable Energy*, 75:356–365, 2015.

[140] KW Thompson. Time dependent boundary conditions for hyperbolic systems. *Journal of computational physics*, 68(1):1–24, 1987.

[141] J Thomson, B Polagye, and MC Durgesh, Vand Richmond. Measurements of turbulence at two tidal energy sites in puget sound, wa. *IEEE Journal of Oceanic Engineering*, 37(3):363–374, 2012.

[142] M Togneri and I Masters. Micrositing variability and mean flow scaling for marine turbulence in ramsey sound. *Journal of Ocean Engineering and Marine Energy*, 2(1):35–46, 2016.

[143] AAR Townsend. *The structure of turbulent shear flow*. Cambridge university press, 1980.

[144] PG Tucker. Differential equation-based wall distance computation for des and rans. *Journal of computational physics*, 190(1):229–248, 2003.

[145] MCLM Van Mierlo and JCC De Ruiter. Turbulence measurements above artificial dunes. *Q0789*, 1988.

[146] B Vermeulen, AJF Hoitink, and MG Sassi. Coupled adcps can yield complete reynolds stress tensor profiles in geophysical surface flows. *Geophysical Research Letters*, 38(6), 2011.

[147] RWCP Verstappen, W Rozema, and HJ Bae. Numerical scale separation in large-eddy simulation. In *Proceedings of the Summer Program*, pages 417–426, 2014.

[148] PL Viollet, JP Chabard, and P Esposito. *Mécanique des fluides appliquée: écoulements incompressibles dans les circuits, canaux et rivières, autour des structures et dans l'environnement*. Presses des Ponts, 2003.

[149] RJ Volino, MP Schultz, and KA Flack. Turbulence structure in rough-and smooth-wall boundary layers. *Journal of Fluid Mechanics*, 592:263–293, 2007.

[150] D von Terzi and J Frohlich. Coupling conditions for les with downstream rans for the prediction of incompressible turbulent flows. In *TSFP DIGITAL LIBRARY ONLINE*. Begel House Inc., 2007.

[151] K Wilcox, I McLeod, A Gerber, T Jeans, and J Culina. Validation of high-fidelity cfd simulation of the unsteady turbulent tidal flow in minas passage. In *the 11th European Wave and Tidal Energy Conference*, volume 13, 2015.

[152] W Wu and U Piomelli. Effects of surface roughness on a separating turbulent boundary layer. *Journal of Fluid Mechanics*, 841:552–580, 2018.

[153] A Yoshizawa and K Horiuti. A statistically-derived subgrid-scale kinetic energy model for the large-eddy simulation of turbulent flows. *Journal of the Physical Society of Japan*, 54(8):2834–2839, 1985.

Appendix A

Appendix

	Subroutines	Function
Boundary Conditions	INI_SEM	Initializes the (DF)SEM
	SYEM	Computes the velocity fluctuations to prescribe using the (DF)SEM
	GET_BND_RECYCLING	Associates the corresponding outlet and inlet points for recycling.
	RECYCLAGE	Prescribes the recycling boundary condition.
	OUTCONVBC	Prescribes the non-reflective outflow boundary condition
Numerical schemes	PREADV	Computes the matrices for the Adams-Bashforth scheme
	DIFF3D	Solves the advection-diffusion part of the Navier-Stokes equations

Table 1: Boundary condition and numerical scheme subroutines performed in TELEMAC-3D.

	Subroutines	Function
Spalart-Allmaras model	SOUSA	Computes the sources terms of the SA equation
	CSTA	Defines the constants involved in the SA model
	SAINI	Initializes the SA viscosity
	SAPICL	Defines the boundary conditions type for the SA viscosity
	SACL3	Compute the Dirichlet boundary conditions for the SA viscosity
	VISCSA	Assembles the total viscosity using the SA model
	WALLDIST	Computes the distance to the closest solid wall
Subgrid models	SMAGO3D	Computes Smagorinsky viscosity components
	VISSMA	Assembles the total viscosity using the Smagorinsky model
	WALE3D	Computes WALE viscosity components
	VISWAL	Assembles the total viscosity using the WALE model
	AMD3D	Computes AMD viscosity components
	VISAMD	Assembles the total viscosity using the AMD model
Embedded LES	ELES_INI	Initializes the embedded LES
	ELES_SEM	Computes the source terms at the interfaces RANS -> LES
	VISEMB	Assembles the total viscosity using the embedded LES method
Post-processing	POST_LES	Computes the averaged fields, the Reynolds stresses, the Q and λ_2 criterions

Table 2: Turbulence modelling subroutines performed in TELEMAC-3D.

	Subroutines	Function
FEM arrays	VC06PP	Computes $\int_\Omega \nabla . f d\Omega$ for prismatic elements
	VC17AA	Computes $\int_\Omega \left(\frac{\partial u_i}{\partial x_j} - \frac{\partial u_j}{\partial x_i}\right)^2 d\Omega$ for triangular elements
	VC17PP	Computes $\int_\Omega \left(\frac{\partial u_i}{\partial x_j} - \frac{\partial u_j}{\partial x_i}\right)^2 d\Omega$ for prismatic elements
	VC20AA	Computes $\int_\Omega 2\left(\frac{\partial u_i}{\partial x_j} + \frac{\partial u_j}{\partial x_i}\right)^2 d\Omega$ for triangular elements
	VC20PP	Computes $\int_\Omega 2\left(\frac{\partial u_i}{\partial x_j} + \frac{\partial u_j}{\partial x_i}\right)^2 d\Omega$ for prismatic elements
	VC21AA	Computes $\int_\Omega \left(\frac{\partial f}{\partial x_i}\right)^2 d\Omega$ for triangular elements
	VC21PP	Computes $\int_\Omega \left(\frac{\partial f}{\partial x_i}\right)^2 d\Omega$ for prismatic elements
Parallelism	P_ALLGATHERV_D	Gathers data from all tasks and deliver the combined data to all tasks

Table 3: FEM arrays computations and parallelism subroutines performed in TELEMAC-3D.

Modélisation de la turbulence induite par la morphologie dans le Raz-Blanchard : Approche régionale avec TELEMAC-LES

Résumé : Les courants marins sont aujourd'hui considérés comme une source d'énergie renouvelable prometteuse. De nombreux projets internationaux consistent à installer différents types de convertisseurs d'énergie des courants marins. La caractérisation des ressources marines est alors essentielle pour optimiser cette production d'énergie. En particulier, les zones à fort potentiel hydrolien sont sujettes à une turbulence multi-échelles, allant de petits tourbillons capables de solliciter les pales en fatigue aux gros tourbillons pouvant perturber la production de la turbine. Une meilleure connaissance de la génération de ces tourbillons et de leur propagation est essentielle. C'est l'objet du projet ANR/FEM THYMOTE (Turbulence, Hydrolienne, Modélisation, Observations et TEsts en bassin) avec comme site d'étude le Raz Blanchard : l'un des sites les plus prometteurs d'Europe. L'une des questions posées concerne la capacité des grandes structures morphologiques du fond marin à produire des tourbillons. La méthode utilisée est l'emploi d'un modèle régional 3D pour couvrir la zone occupée par ces reliefs.
Les modèles régionaux tels que TELEMAC-3D utilisent une fermeture turbulente de type URANS (Unsteady Reynolds Averaged Navier Stokes), avec par exemple le modèle $k-\varepsilon$. Cette approche ne permet pas une description fine des instationnarités de la turbulence. Cependant, grâce à l'augmentation des performances de calcul, la méthode Large Eddy Simulation (LES) devient envisageable. Celle-ci s'appuie sur un filtrage de l'écoulement, et consiste à simuler uniquement les plus grandes échelles de turbulence. Les plus petites, elles, sont modélisées. Le code TELEMAC-3D a été modifié durant cette thèse de manière à introduire cette fermeture turbulente. Le code développé permet de simuler des écoulements à surface libre en tenant compte d'une large gamme d'échelles allant de la turbulence à la propagation de la marée. Le code TELEMAC-LES a été validé sur la base de résultats expérimentaux issus de la littérature. Il est ensuite utilisé pour étudier les écoulements turbulents dans le Raz Blanchard grâce à une stratégie par emboîtement. La méthode LES permet alors une description fine de la turbulence de ces milieux, conduisant à l'identification de structures tourbillonnaires énergétiques, et donc la définition des zones les plus appropriées pour l'installation d'hydroliennes.

Mots-clés : Hydrodynamique, Hydrolienne Marine, Modélisation numérique, Large Eddy Simulation, TELEMAC

Morphology induced turbulence modelling the Alderney Race site: Regional approach with TELEMAC-LES

Abstract: Nowadays tidal currents are considered a promising renewable energy source. Many worldwide projects involve the installation of different types of marine current energy converters. The characterisation of marine resources is therefore essential to increase efficiency of energy production. Areas with high hydroturbine potential are particularly subject to multi-scale turbulence, ranging from small vortices able to cause large fatigue loads, to large vortices capable of disrupting turbine production. A better knowledge of the generation of these eddies and their propagation is essential. This is the purpose of the ANR/FEM THYMOTE project (Turbulence, Hydrolienne, Modélisation, Observations et TEsts en bassin) studying one of the most promising sites in Europe: the Alderney Race. One of the questions raised concerns the ability of large morphological structures on the seabed to produce eddies. The adopted method uses a 3D regional model to cover the area occupied by these bedforms.
Regional models such as TELEMAC-3D use a turbulent URANS (Unsteady Reynolds Averaged Navier Stokes) closure, with for example the $k-\varepsilon$. This approach does not allow a detailed description of the instability of turbulence. However, thanks to the increase in computing resources, the large scale method (LES) becomes feasible. This is based on flow filtering, and consists of simulating only the largest turbulence scales, whereas the smaller ones are modeled. The TELEMAC-3D code was modified during this thesis in order to introduce this turbulent closure. The code developed allows free surface flows to be simulated over a wide range of scales from turbulence to tidal propagation. The TELEMAC-LES code has been validated on the basis of experimental results from the literature. It is then used to study turbulent flows in the Alderney Race using a nesting strategy. The LES method allows a detailed description of the turbulence of these environments. It finally leads to the identification of energetic vortex structures, and thus the definition the most appropriate zones for the installation of tidal turbines.

Keywords: Hydrodynamic, Tidal turbines, CFD, Large Eddy Simulation, TELEMAC